University of Southern Queensland

Analysing Urban Aerosols using a Digital Camera

A Dissertation submitted by

Damien Igoe, BAppSci BSc (Hons) BSpecEd DipEd MEd

For the award of

Masters of Science

Supervisor: Dr. Brad Carter
Associate Supervisor: Dr. Alfio Parisi

February, 2011

Abstract

This dissertation tests the idea that 'off the shelf' digital cameras can be used to supplement or replace more cumbersome methods of detecting and classifying urban aerosols. Currently, most aerosol observations are made using expensive and specialised equipment that can often only analyse a small portion of the sky at a time. In contrast, the recent proliferation of high-resolution wide-field colour digital cameras with advanced noise reduction makes feasible the use of colorimetric image calibration to provide a cost-effective alternative for monitoring air pollution for research, education and outreach purposes.

Nitrogen dioxide and carbonaceous (soot) aerosols from human activities are the two main types of discolouring aerosols causing the haze and choking dust commonly observed in many large cities, particularly Asian megacities such as Tokyo. These aerosols deserve more extensive study due to their potential for widespread negative effects on climate, ecosystems, human health, and transportation. This dissertation thus involved the use of a digital camera for repeated imaging of Tokyo's polluted skies under different meteorological conditions, with images subjected to detailed colorimetric calibration and analysis. This work included the effects of a volcanic eruption that fortuitously occurred near Tokyo during this study.

The results obtained in this thesis indicates that a modern mass-market digital camera produces wide-field colorimetric aerosol data of comparable accuracy to that obtained from expensive specialised equipment and models. Such an outcome can be used to promote more widespread monitoring of aerosols and greater awareness and understanding of the local effects of air pollution.

Certification of Dissertation

I certify that the ideas, experimental work results, analyses, software and conclusions reported in this dissertation are entirely my own effort, except where otherwise acknowledged. I also certify that the work is original and has not been previously submitted for any other award, except where otherwise acknowledged.

_____ _____

Signature of Damien Igoe

Endorsement

_____ _____

Signature of Dr. Brad Carter, Principal Supervisor

_____ _____

Signature of Dr. Alfio Parisi, Associate Supervisor

Acknowledgements

From Tokyo to Toowoomba and beyond, there are a number of people that must be acknowledged for their support in completing this thesis. The challenges were great, but so was the help rendered by a lot of people.

First and foremost, Dr. Brad Carter, Principal Supervisor for the duration of the project – he is a gentleman of patience and incredible knowledge. Dr. Alfio Parisi, who stepped in as Associate Supervisor for the project, provided great insight and patience in the completion of the thesis.

The study was completed on the roof of an inner city International School in Tokyo: K. International School, Tokyo (KIST). The school owners, Mr. and Mrs. Komaki are thanked for allowing me access to one of the viewing platforms. Many kind thanks are given to Vice Principal Damian Rentoule, who always supported the study. Gratitude is also extended to History teacher, Michael Wagner; Art teacher, Daryl Bates and Kindergarten teacher Jody Hancock for the many discussions, proof reading and assistance in many of the experiments. A special thank you goes to Jody's 8 year old daughter, for being the greatest laboratory assistant.

Most of all, sincerest gratitude is extended to my parents, Denis and Lorraine and my large extended family of talented tradespeople, teachers and musicians, their unfailing support was a major driving force in the project's completion. My family never let me lose focus when things got tough.

Words can hardly do justice for the gratitude I feel for these people.

This thesis is dedicated to the greatest teacher I have ever known, my grandmother Joyce Taylor, who left us in August of 2010 after a long and full life – she left us just before the completion of the thesis that she gave me so much encouragement to complete. She always knew where I was headed, even if I forgot at times.

Table of Contents

List of Figures

List of Tables

1. Introduction

1.1 Rationale

This study aims to evaluate the modern digital (still) camera as a cost-effective and accessible means of monitoring urban air pollution for different purposes, including research, education and outreach.

Clear and polluted skies have measurable colorimetric characteristics that have been predominantly measured using spectroradiometers, Whole Sky Imagers and modelled based on the effects of scattering and absorption on sky colour.

Phases of daylight and the inclusion of aerosols result in defined colorimetric behaviour. Observations are made using blackbody or Planckian correlated colour temperature chromaticities on the Planckian locus and the greener, semi parallel Daylight locus (also referred to as the Daylight locus) as bases.

The following are generalisations made from previous studies (these will be elaborated on further in the thesis):

- Unpolluted clear and cloudy skylight (not including the sun) is generally on the Daylight locus, becoming greener with elevation from the horizon.

- The presence of absorbing and scattering particulate matter results in achromatic chromaticities, often seen as grey or whitish haze. These chromaticities have very little spread and usually lie between the Daylight and Planckian loci.

- Nitrogen dioxide, which absorbs blue light, results in a chromatic 'yellow-red' shift. The higher the concentration of nitrogen dioxide, the more the colour shifts towards red-yellow.

Mass-market digital cameras are made with similar CCD sensor technology used in conventional observations, thus it is feasible for there to be similar observations. The processing of data provides a powerful teaching tool and can be streamlined to allow observations to be made anywhere, by anyone.

Increased involvement by schools and the public in monitoring air pollution raises awareness of its effects, particularly when it comes to haze and soot. Rather than have students learn about air pollution "second-hand" from a textbook or the media, digital cameras can directly involve people in a practical scientific study to where they live.

Modern low-cost digital camera technology can be used to assist science education in developing as well as developed nations. For example, a delegation from an Italian university recently travelled to northern Uganda to enhance science student learning by retraining their teachers from ROTE learning methods (Rossi et al. 2010). A major problem was the lack of relevant equipment and expertise, which to some degree is the same for science

classrooms anywhere. Starting instead with widely available technology offers alternative ways to do science.

Accessible and inexpensive imaging technology is not confined to digital still cameras, and includes security cameras, webcams and cameras contained in smart phones such as the iPhone. In particular it is reasonable that the same techniques used for digital still cameras could be applied to phone cameras, with appropriate recalibrations and technical support from online and written sources.

Phone cameras in particular, represent the proliferation of dual imagining and communication technology. Alongside freely available photo-sharing and customisable web based analysis tools, the door has been opened to the involvement of people anywhere regardless of location and qualifications to participate in aerosol studies as "citizen scientists". Studies such as that conducted in this thesis are done with possible broader wide-ranging monitoring and collaboration in mind.

1.2 Colorimetry Literature Review

Colorimetry is a relatively new science and its specific use in aerosol studies has been explored only since the 1930s and 1940s with the pioneering work of researchers such as MacAdam (1981, 1942). However, it can be argued that the first real studies of aerosols were by artists across the centuries. This first part of the Literature Review recounts the rich and varied history of ideas and developments leading to modern colorimetry.

The Literature Review discusses measurements and observations of urban aerosol pollution in Tokyo as an example of a megacity and the base for this study. Included in the review will be a brief discussion of the consequences on the local climate and human health.

Conventional methodologies of measurement and observation as applied in Tokyo and other major cities are discussed in light of their limitations. Discolouring aerosol optical absorption and scattering are explored in terms of their respective colorimetric effects, supported by observations made in prior studies, particularly with the use of CCD digital still cameras.

Finally, the variable of seasonality is briefly discussed, as this provides a background for what can be usually expected over the time of the study. Temporal changes in aerosol concentrations are also explained in terms of historical policy. The Tokyo Ministry of Environment provided all seasonal, temporal and hourly data for the study location.

1.2.1 History and Development of Colorimetry

Colorimetry is the science of measurement of colour and its aspects; namely chromaticity, including the colour primaries (red, green and blue); hue, chroma, including saturation and purity; brightness and lightness (relative luminance) (Brainard and Stockman, 2009; Zhang and Montag, 2006; Ohno, 2000).

Colorimetry is closely related to studies about the effects of colours on visual perception, emotions, philosophy and spatial awareness (Kim, 2006; Ohno, 2000; Zelanski and Fisher, 1994). What follows is a brief account of the development of modern colorimetry as applied to atmospheric sciences.

In the past, colour differences in colorimetric metrics including hue, purity and brightness were discerned by an artist's eye, expressed via the palette, often into a masterpiece on canvas. Imaging with the common digital still camera (DSC) is similar; where the digital image is analogous to the canvas and the primary colour CCD sensor to the palette. However, despite the technological advances, the colour difference is still discerned by the photographer's eye.

Modern atmospheric colorimetry can trace its lineage of ideas back to the philosophers, artists and alchemists of the ancient world, through Medieval

Europe to the modern day and comparatively recently, psychologists and scientists in modern laboratories around the world (Kuehni, 2007a; Hutchings, 2006). The discipline started, like so many of the modern sciences, as disparate parts for different purposes, only truly coalescing in the 20th century.

Light and colour have long been the subject and inspiration of many art forms, from poetry to paintings to modern photography (Hutchings, 2006; Zelanski and Fisher, 1994). Colour in many ancient art forms represented the foundations of existence, such as in Buddhism (Kim, 2006). From these humble beginnings, the foundations of colorimetry emerged.

Two sets of primary colours exist, based on additive and subtractive principles and applications (Jacobson, 2006; Malacara, 2002):

- When colours combine to become white, such as with light, these are said to be additive. The additive primaries are red, green and blue – the basis of CCD sensor arrays.
- When colours combine to become black, such as with paint and optical filters, these are subtractive. The subtractive primaries are red, yellow and blue.

All of the primary colours make up the '4 unique hues': red, yellow, green and blue that are used in both art and modern colorimetry.

Some of the earliest ideas, from well known ancient scholars as Plato and his student Aristotle, sought to explore the aesthetic perceptions of colour, for many years seeking to relate it to music, attempting to correlate 7 colours to the 7 music notes (Keuhni, 2007a; Spivey, 2005; Williams, 2005). Across ancient Europe and Asia, colours represented the 4 main elements of existence – water, air, earth and fire (Kim, 2006).

Robert Grosseteste, a 13th century bishop in England, followed by 14th century German theologian and natural scientist, Theodoric of Friesberg, identified the 4 unique hues when studying the rainbow (Keuhni 2007a). Later, Rene Descartes determined that a rainbow is comprised of primary and secondary colours (Wiliams, 2005).

In classic and modern Korean, the representation of 'dyed colour' means the hue after the dye combines with an object, hence colour mixing (Kim, 2006). Renaissance to modern day artists, in their quest to fully capture a scene experimented with colour mixing, specifically adding and subtracting pigments and light (Keuhni, 2007a; Wright, 2007; Zerefos et al. 2007; Zelanski and Fisher, 1994).

Leonardo da Vinci, within his artistic masterpieces explored concepts of light and shade and colour mixtures. Italian and French researchers at the time studied perceived lightness and identified black as an absence of colour (Keuhni, 2007a). Later, Grassman formulated early laws of colorimetric colour mixture (Wright, 2007).

The famous Alchemist, Sir Isaac Newton did much to elucidate the nature of light and through his diffraction experiment revealed that the end bands of light were perceptually similar, thus could be joined up as his well-known and still used colour wheel (Wright, 2007; Zelanski and Fisher, 1994). He demonstrated that white light is comprised of all the visible wavelengths, dividing into the spectrum (Wright, 2007; Williams, 2005; Zelanski and Fisher, 1994). The spectral divisions were found to be parts of the continuous spectrum by later researchers such as Aubert and Root in the 19th century (Williams, 2005).

The famed German dramatist, poet, playright and artist, Johann Wolfgang von Goethe is sometimes heralded as a pioneer of colorimetry (Williams, 2005). His book, 'Theory of Colour', published in 1810, studied the effects of and consequently recommended the use of complementary colours to separate costumes from stage scenery (Spivey, 2005; Williams, 2005).

Matthias Klotz, an often forgotten German painter and lithographer, living at the same time as Goethe, developed a lightness scale which was used as a basis of a 24 hue circle and thus demonstrated notions of chromatic theory opposing colours (Keuhni, 2008). Sensitivities to opposing white-black, red-green and yellow-blue that form the basis of many colour spaces were investigated later in the 1800's by Hering (Ohno, 2000).

Thomas Young built on the earlier studies of English glass merchant George Palmer to describe the 3-colour (trichromatic) theory of vision in the early 19th century (Keuhni, 2007b; Williams, 2005; Ohno, 2000). Herman von Helmholtz further quantified Young's theories and observations, forming the basis of trichromatic theory (Williams, 2005).

Maxwell identified the 3 primary colours of light recognised today in the mid-19th century (Williams, 2005; Ohno, 2000). Maxwell developed a quantitative theory of colour with his 'colour box' that allowed the mixing of the 3 primaries into the colours perceived, thus calculating the first colour mixing curves and his colour triangle, an early equilateral version of the modern chromaticity chart (Wright, 2007).

Maxwell is widely considered to be the 'father' of modern colorimetry (Wright, 2007; Williams, 2005; Ohno, 2000). Remarkably, Maxwell also produced the first colour photo in a presentation to the Royal Society of London in 1861. Maxwell used what could be considered the forerunner of the tricolour CCD chip, by passing light through a red, green and blue filter (Wright, 2007; Williams, 2005). Konig and Abney further refined Maxwell's colour mixing curve (Keuhni, 2007b; Wright, 2007).

In the absence of mainstream instrumentation to record the colour detail of the skies, paintings provide a wealth of information about aerosol loading, particularly about distant volcanic eruptions occurring at the time, from careful analyses of the colours the artists used (Zerefos et al. 2007).

The famed impressionist artist, Claude Monet often painted the different colours of the sky through different times of the day and across the seasons, relying on

what he saw, rather than any interpretation (Williams, 2005; Zelanski and Fisher, 1994). In his later paintings including the famed lily series, cataracts distorted his perception of colour resulting in a greater emphasis of the yellows and reds (Brown, 2007). This perception is in some way, similar to the yellowing that occurs in the presence of atmospheric haze.

The 19th century English artist, Turner, commenting on his landscape paintings which included rich visions of the sky at the time, is quoted as saying:

"*I did not paint it to be understood, but I wished to show what the scene was like*"
(Zerefos et al. 2007).

Through their attention to detail, these Masters had unintentionally recorded the colour of the sky in exquisite detail, sometimes, suitable for analysis (Butkus and Johnson, 2010; Zerefos et al. 2007). Turner's quote suggests that the Masters' works, while being aesthetically pleasing and thought provoking, were also a precursor to recording scenes using the modern digital camera.

Artistic perspectives related to volcanic dust interactions form the basis of many paintings by artists who focused particularly on sunsets and sunrises (Butkus and Johnson, 2010; Zerefos et al. 2007). Examples include Turner's 'Sunset' from the early 19th century and Munch's 'The Scream' from late in that century that depicted the effects of distant volcanic eruptions occurring around the same time (Zerefos et al. 2007).

Ludwig Pilgrim, a German Physics and Mathematics teacher is another forgotten link in the development of modern colorimetry. He published a treatise further explaining Young, Helmholtz and Konig's work in his school's yearbook in 1901 and expanded on the plotted colour space developed earlier by Konig (Keuhni, 2007b).

Albert Munsell, an American artist and colour theorist developed the widely used Munsell colour chart in the early 20th century that specifically describes a colour's hue, chroma and value as measures of a colour's purity and intensity (Wright, 2007; Williams, 2005; Zelanski and Fisher, 1994). These colour charts are still used as analysis tools for commercial purposes and in atmospheric colorimetry (Hunt, 2006; Malacara, 2002; Wyszecki and Stiles, 2000; Zelanski and Fisher, 1994).

The early part of the 20th century up to 1931 was an 'arms' race between the United States and Great Britain for discoveries on the nature of photometry. By 1924, the United States hit the 'lead' with researchers such as Gibson and Troland of the Optical Society of America developing the standard visibility curve $V(\lambda)$, still in use today (Wright, 2007; Hunt, 2006; Malacara, 2002; Wyszecki and Stiles, 2000).

In the late 1920's, further developments of colour solids were made by American, British and German researchers (Keuhni, 2007b). Around 1930,

Wright and Guild made observations using the red-green-blue primaries that formed a great part of modern colour spaces (Ohno, 2000).

The Commission Internationale L'Eclairage (CIE) convened in 1931 culminating all the research about colour theory since Maxwell's time, predominantly the work from researchers in the United States and remodelling the colour solids made since Konig's research (Keuhni, 2007b; Wright, 2007; Ohno, 2000). The CIE (1931) primaries were rather different than those described by Wright and Guild, formally defined as having wavelengths of 700 nm for red, 546.1 nm for green and 435.8 nm for blue (Ohno, 2000).

The CIE convention established the standard framework used in colorimetry, the tristimulus CIE XYZ and CIE xyY systems that mathematically categorises all spectral colours and to what are referred to as the 'non-spectral purples' (Brainard and Stockman, 2009; Wright, 2007; Williams, 2005; Hunt, 2006; Malacara, 2002; Ohno, 2000; Wyszecki and Stiles, 2000).

In 1960 and later revised in 1976, the Uniform Colour Spaces, starting with CIE u'v'Y were developed as being more perceptibly true than the earlier CIE xyY colour space. At the same time, the CIELAB and CIELUV colour spaces were developed for the textile and digital imaging industries respectively, the latter derived from CIE UCS. The CIELch (luminance, chroma and hue angle) colour space was derived from both CIELAB and CIELUV to provide more in-depth colour information (Hunt, 2006; Malacara, 2002; Ohno, 2000; Wyszecki and Stiles, 2000).

Further work in the 1990s and early part of the 21st century led to the formulation of the CMC, BFD, CIE94 and the CIEDE2000 colour difference formulae derived from the CIELAB colour space. The CIEDE2000 colour difference is the latest and is thus recommended by the CIE for use in any analyses (Kandi and Tehran, 2010; Witt, 2007; Hunt, 2006; Malacara, 2002; Ohno, 2000; Wyszecki and Stiles, 2000).

Further developments of colour spaces are increasingly collaborative between colour scientists, designers, psychologists and artists, particularly in response to the demands of modern and emerging imaging technology including digital cameras, smart phones and webcams (Heckaman and Fairchild, 2006; Hutchings, 2006).

1.2.2 Atmospheric Aerosol Studies

There is strong interest in research about the effects of aerosols on the climate (Yan et al. 2008; Zhang et al. 2008; De Tomasi et al. 2007; Duffy and Bonfils, 2007; Mahmood, 2007; Johnson et al. 2005; Dogras et al. 2004; Wang et al. 2004; Malinowski et al. 1998; Pandis et al. 1995).

How clouds and aerosols interact is a major source of uncertainty and is of great interest to researchers particularly for their effects on climate forcing and UV

irradiance (He et al. 2009; Alexander et al. 2008; Yan et al. 2008; Zhang et al. 2008; Duffy and Bonfils, 2007; Gangl et al. 2007; Mahmood, 2007; Long et al. 2006; Lee Jr. and Hernandez-Andres, 2005; Johnson et al. 2005; Wang et al. 2004; Sabburg and Wong, 1999; Malinowski et al. 1998).

It is generally accepted that soot, nitrogen dioxide and other aerosols have a measurable effect on local and global climate systems, often affecting local temperatures, albedo and hydrologic cycles. The result of scattering and absorption by aerosols degrades visibility and contrast, creating problems for air travel (He et al. 2009; Alexander et al. 2008; Haralabidis and Pilinis, 2008; Yan et al. 2008; Zhang et al. 2008; De Tomasi et al. 2007; Gangl et al. 2007; Janeiro et al. 2007; Chou et al. 2005; Haralabidis and Pilinis, 2005; Johnson et al. 2005; Nieves et al. 2005; Dogras et al. 2004; Molders and Olson, 2004; Schnaiter et al. 2003; Torres et al. 2002; Jacobson, 2001; Mahadev and Henry, 1999; Yoshikado and Tsuchida, 1996; Pandis et al. 1995; Takamura, 1992).

Over the past decade, Tokyo has experienced an increase in summertime low level cloud, (Souch and Grimmond, 2006), partly due to the increase in cloud condensation nuclei (CCN) associated with increased urban aerosols, seasonal natural dust events from northern China and Mongolia referred to by the Japanese as 'Kosa' and infrequent volcanic eruptions (Takeo, 2008; Zhang et al. 2008; Molders and Olson, 2004; Wang et al. 2004; Highwood and Stevenson, 2003; Pandis et al. 1995; Zielinski et al. 1994).

NO_2 and suspended particulate matter (SPM) reach a peak during calm days, primarily during early winter (Yoshikado and Tsuchida, 1996). Concurrently, overall temperatures have risen in Tokyo, particularly over the past decade in line with similar increases recorded in China and Taiwan (He et al. 2009; Schaefer and Domroes, 2009; Kondo et al. 2006; Chou et al. 2005; Jacobson, 2001).

Increased temperature and aerosol concentrations raise concerns about human health from heat-related conditions, and given soot's small size (often less than 100 nanometres), it can be inhaled deep into the lungs, resulting in pulmonary conditions (He et al. 2009; Zhang et al. 2008; Johnson et al. 2005; Liu et al. 2005; Torres et al. 2002).

Most soot in urban environments comes from the incomplete combustion of diesel fuel, coal and biomass burning. Soot is often quickly mixed with sulphates (He et al. 2009; Yan et al. 2008; Zhang et al. 2008; Gangl et al. 2007; Kondo et al. 2006; Johnson et al. 2005; Liu et al. 2005; Monkkonen et al. 2005; Renard et al. 2005; Dogras et al. 2004; Schnaiter et al. 2003; Jacobson, 2001; Yoshikado and Tsuchida, 1996; Pandis et al. 1995).

In central Tokyo, soot concentrations peak with rush hour traffic (Kondo et al. 2006). The same correlation was also noted for Mexico City, New Delhi, Beijing and surrounding areas observed during 2003-2005 (He et al. 2009; Yan et al. 2008; Johnson et al. 2005; Monkkonen et al. 2005).

Conventional methodologies for urban aerosol research are varied, using numerical and statistical techniques and equipment such as LIDAR, radar, profilers, transmissometers, photometers, ceilometers, remote sensing (Duffy and Bonfils, 2007; Janeiro et al. 2007; Souch and Grimmond, 2006; Lim et al. 2004; Seiz and Baltsavias, 2000; Ackermann, 1998). Ground based LIDAR and photometer systems provide vertical profiles of aerosol radiative forcing and aerosol extinction (De Tomasi et al. 2007).

Conventional observation methods have been widely used in observations in Tokyo and many other major cities, including:

- Physical sampling: Measurements and analyses of soot from Tokyo used a Thermo-Optical Analyser, calibrated Scanning Mobility Particle Sizer and a Carbon Analyser (Kondo et al. 2006; Chou et al, 2005). Physical sampling was performed in Beijing and Taipei using Quartz and Teflon multi stage impactors (Yan et al. 2008; Chou et al. 2005) and via a Time Resolved Aerosol Collector, also used in studies in Mexico City (Johnson et al. 2005). Further analyses of aerosols performed in Mexico City during 2003 used scanning and transmission electron microscopy and x-ray analysis (Johnson et al. 2005). A similar method was used by Alexander et al (2008) to determine the differences between 'black carbon' (soot) and the largely transparent brown carbon.

- Optical sampling: He et al (2009)'s and Yan et al (2008)'s study of Beijing aerosols were performed using a nephelometer to measure light scattering coefficients, an aethalometer to measure soot concentrations and an automatic weather station to correlate meteorological and aerosol data. The effects of natural dust events (Yellow or 'Kosa' dust) emanating from northern China and Mongolia are detected and analysed using a sunphotometer (Wang et al. 2004). Spectroradiometers were used by Lee Jr, and Hernandez-Andres (2005) to determine the spectral properties of overcast skies in Granada, Spain.

However, it is very difficult to achieve adequate multispectral imaging at low cost and with high portability (Nieves et al. 2005). Most commonly used instrumentation are one dimensional, therefore surveying a whole scene is very time consuming (Wuller and Gabele, 2007; Nieves et al. 2005; Seiz and Baltsavias, 2000; Lee Jr. 1994).

Satellite imagery is also a very common and relatively efficient means to retrieve aerosol data, sometimes in conjunction with models (Johnson et al. 2005; Wang et al. 2004; Torres et al. 2002; Sabburg and Wong, 1999; Roy et al. 1998). Aerosol properties are often detected using the Aerosol Robotic Network (AERONET), Total Ozone Mass Spectrometer (TOMS), the Moderate-Resolution Imaging Spectroradiometer (MODIS) and the Multiangle Imaging SpectroRadiometer (MISR) (Wang et al. 2004; Torres et al. 2002; Cairns et al. 1998).

Satellite imagery has weaknesses in quantifying small sky features due to spatial resolution limitations (Long et al. 2007; Cairns et al. 1998). Difficulties occur with data collection from surfaces with low reflectivity and contrast, such as urban environments (Torres et al. 2002). Cloud cover often impedes adequate satellite imagery data being obtained (Lim et al. 2004).

Aerosol optical models provide a basis for analysis, often employing colorimetry metrics. Models by Dogras et al. (2004), assume a sky with sulphuric acid and soot. Similarly, Sloane (1988) modelled the interaction between soot and NO_2. Models by Haralabidis and Pilinis (2008) simulate viewing of a cloudless sky through a skydome. The models use D_{65} daylight illuminant as the spectral radiant power input (Haralabidis and Pilinis, 2008; Dogras et al. 2004; Sloane, 1988). Twilight aerosol polarisation models were developed by Postylyakov et al (2003).

Aerosol-colorimetric models cannot fully take all of the variables into account, particularly for something as dynamic as aerosol behaviour, particularly when associated factors such as meteorological conditions are considered (Haralabidis and Pilinis, 2008).

1.2.2.1 Aerosol Absorption

Only those aerosol particles that contain elemental carbon (the main constituent of soot), iron oxides sometimes found in volcanic ash, and gaseous NO_2 are highly absorbing in the visible spectrum. Absorption is strongest at lower wavelengths (blue) (Kokhanovsky, 2008; Yamanoi et al. 2008; Zhang et al. 2008; Gangl et al. 2007; Shaddix and Williams, 2007; Chou et al. 2005; Haralabidis and Pilinis, 2005; Dogras et al. 2004; Highwood and Stevenson, 2003; Schnaiter et al. 2003; Horvath, 1993; Sloane, 1988).

Transparent aerosols, such as sulphates, contribute very little to visible sunlight absorption, unless attracted to soot (Zhang et al. 2008; Johnson et al. 2005; Dogras et al. 2004; Schnaiter et al. 2003). The absorbing and discoloring effect of soot mixed with sulphates is considerable due to what is referred to as microlensing. Microlensing describes how aerosol sulphates act as a magnifying glass, focusing incident light onto the soot grain, increasing absorption (Zhang et al. 2008; Gangl et al. 2007; Chou et al. 2005; Johnson et al. 2005; Dogras et al. 2004; Schnaiter et al. 2003).

The refractive indices of some aerosols, including sea salt and sulphates, change with increasing ambient humidity and particle or droplet diameter (Alexander et al. 2008; Gangl et al. 2007; Shaddix and Williams, 2007; Haber et al. 2005; Dogras et al. 2004; Ackermann, 1998).

1.2.2.1.1 Detecting Aerosol Absorption

With the proliferation of high resolution digital still cameras, it is now possible to achieve fine resolution image analysis of the sky. Luminance constancy and reproducibility is possible with digital cameras, as a large array of points are captured at the same time in a photo and can be stored as an image file for further analysis (Wuller and Gabele, 2007; Malinowski et al. 1998).

Digital cameras provide a low cost, easy to use, multispectral imaging technique alternative to commonly used more expensive methodologies (Lee Jr. 2008; Janeiro et al. 2007; Nieves et al. 2005; Spasojevic and Mahdavi, 2005; Seiz and Baltsavias, 2000; Lim et al. 2004; Lee Jr.. 1994).

Colour shifts that may go unnoticed by the human eye can be potentially detected by a digital camera (Haralabidis and Pilinis, 2008). Digital cameras can detect a colour change in fine resolution, when the average signal to noise ratio for each RGB channel is above 1 (Haralabidis and Pilinis, 2008; Spasojevic and Mahdavi, 2005; Dogras et al. 2004; Lim et al. 2004; Roy et al. 1998).

The colorimetric precision of digital cameras was noted in tests performed by Haralabidis and Pilinis (2005) using a colorimeter, based on a single sensor CCD camera operated from dawn to dusk. A recent application of CCD technology to UV and cloud based studies is the development and use of whole-sky imagers (Lee Jr. 2008; Long et al. 2006; Sabburg and Wong, 1999; Shields et al. 1998).

1.2.2.2 Aerosol Scattering

The three broad classes of scattering, namely geometric, Mie and Rayleigh, are based on the ratio of the relative aerosol diameter to the magnitude of the incident wavelength of light. All three have different effects on the expected colorimetric properties of the atmosphere in various conditions (Petty, 2006; Seinfeld and Pandis, 2006; Haber et al. 2005; Hinds, 1999; Preetham et al. 1999; Horvath, 1993; van de Hulst, 1981).

When the size ratio is much greater than 1 (meaning that aerosol particle diameter is several orders of magnitude larger than the wavelength of transmitted light), it is said to be the geometric optics regime, which has the greatest influence on aerosol scattering (Petty, 2006; Seinfeld and Pandis, 2006; Hinds, 1999; van de Hulst, 1981).
Geometric optics is not specifically wavelength dependent, obeying geometric laws such as reflection, diffraction and refraction (Petty, 2006). Water droplets are large enough to be in the geometric regime and are the medium for refraction, forming rainbows (Seinfeld and Pandis, 2006; van de Hulst, 1981).

Mie scattering occurs when the size ratio is approximately 1, meaning that the particle size is approximately that of the incident light wavelength. (Petty, 2006; Seinfeld and Pandis, 2006; Haber et al. 2005; Hinds, 1999; Preetham et al. 1999; Horvath, 1993; van de Hulst, 1981). Most urban and many volcanic aerosols are

of the size that is affected by Mie scattering and thus is a source of colorimetric variation (Kokhanovsky, 2008; Yamanoi et al. 2008; Petty, 2006; Seinfeld and Pandis, 2006; Haber et al. 2005; Preetham et al. 1999; Lee Jr. 1994; Horvath, 1993; van de Hulst, 1981).

When sunlight (approximating white light) passes through a haze layer, with elevated concentrations of aerosol particulate matter such as dust and soot, blue wavelengths are preferentially backscattered, leaving some green and mostly red to reach the observer. As blue light has been effectively 'removed', the sky colour 'shifts' towards yellow and red (Yamanoi et al. 2008; Seinfeld and Pandis, 2006; Dogras et al. 2004; Horvath, 1993; Sloane, 1988). Backscattering occurs when incident light is completely reflected (Hinds, 1999).

Turbidity is the term used to describe the fraction of scattering caused by urban aerosol haze, the higher the turbidity, the more haze, the greater yellow-red shift and thus the greater the effects on visibility and visual contrast of distant objects (Haber et al. 2005; Preetham et al. 1999; Horvath, 1993).

Rayleigh or molecular scattering predominates when the size ratio between the aerosol and incident wavelength is far less than 1 (when the particle diameter is approximately the fourth root of the wavelength), thus is extremely wavelength dependent (Petty, 2006; Seinfeld and Pandis, 2006; Haber et al. 2005; Hinds, 1999; Preetham et al. 1999; Horvath, 1993; van de Hulst, 1981).

The ambient colour of the clear sky is blue because blue light has greater diffuse scattering than red through Rayleigh scattering (Petty, 2006; Seinfeld and Pandis, 2006; Haber et al. 2005; Horvath, 1993). Nitrogen dioxide is small enough to be within the Rayleigh scattering regime. However, this aerosol preferentially absorbs blue wavelengths allowing some of the green and most of the red to pass through to the observer, but as these wavelengths are not as strongly scattered, they appear pale (Horvath, 1993).

In the atmosphere, single scattering phenomena such as described above is more of an approximate model rather than a true picture of how light interacts with aerosols. In reality, light undergoes multiple scattering (Haber et al. 2005; Preetham et al. 1999). Multiple scattering is more likely with increased optical path length, such as when sunlight is incident near the horizon and especially at dawn and dusk (Lee Jr. and Hernandez-Andres, 2005).

As the viewing angle trends towards the horizon, the optical air path increases, as does the incidences of multiple scattering, resulting in much of the blue light to be backscattered (Seinfeld and Pandis, 2006; Haber et al. 2005; Lee Jr. and Hernandez-Andres, 2005; Preetham et al. 1999; Lee Jr. 1994; van de Hulst, 1981). Non-absorbing dust causes an associated brightening near the horizon, when absorbing soot is added, a darkening is observed (Haber et al. 2005).

1.2.3 Volcanic Ash

Japan is one of the most volcanically active regions of the planet. The confluence and interaction of the Pacific, Eurasian, Philippines and North American tectonic plates and their associated subduction zones result in over 500 volcanoes in the country, of which 108 are active (Kubota and Fujioka, 2009; Simkin and Siebert, 1994; Zielinski et al. 1994; Global Volcanism Network). The most active volcano in Japan is Sakura-jima on the southern island of Kyushu (Yamanoi et al. 2008).

There are several active volcanoes in the vicinity of Tokyo. The most iconic of these, Mt. Fuji has been dormant for many centuries and is not the most active in the area. Mt. Asama, 36°30'N 138°54'E, 140 km north west of Tokyo is considered to be the most active volcano in the region (Kubota and Fujioka, 2009; Takeo, 2008; Zielinski et al. 1994). According to the Global Volcanism Network website, activity at Mt. Asama has occurred since as early as 14,000 years before present, with major eruptions occurring in 1108AD and 1783AD, the latter at about the same time as the Laki, Iceland eruption that significantly affected the climate in the Northern Hemisphere (Highwood and Stevenson, 2003; Zielinski et al. 1994).

Numerous studies have been performed on the ash from Mt. Asama, particularly in response to recent activity (2004 and 2009). Asama is unique in that unlike many volcanoes, it releases much less aerosol sulphate (Kokhanovsky, 2008; Tsunematsu et al. 2008; Highwood and Stevenson, 2003; Jacobson, 2002; Zielinski et al. 1994). However the dust and ash from Mt. Asama has been found to act as cloud condensation nuclei (CCN)', causing an increase in cirrus, rain and snow, observed during eruptions since the 1950s (Kokhanovsky, 2008; Tsunematsu et al. 2008; Jacobson, 2002; Zielinski et al. 1994; Isono, 1955).

Studies by Yamanoi et al. (2008) at Sakura-jima determined that different eruptive types result in red-yellow shifting of the sky colour. A common inclusion in volcanic ash, ferrous iron causes absorption, similar to soot, peaking at 512 nm (Kokhanovsy, 2008; Yamanoi et al. 2008; Jacobson, 2002).

The last 2 eruptions of Mt. Asama were in September, 2004 and in early February, 2009, although the eruptions were relatively minor. On both occasions however, ash did reach Tokyo (Kubota and Fujioka, 2009). The 2009 eruption occurred during the present study, thus is of particular interest to this study and provided a unique opportunity to study the effects of aerosol volcanic ash.

There are significant difficulties with the colorimetric detection of volcanic ash, particularly in an urban environment where ferrous iron has similar colorimetric properties as soot (Horvath, 1993). Scattering from volcanic ash, when mixed with urban dust, would also be difficult to detect, thus could be a limitation.

1.2.4 Aerosol Seasonal Averages

Since environmental laws were enacted in the late 1960's into the 1970's, Tokyo's air quality has improved significantly (Okubo and Takahashi, 2009; Fukushima, 2006; Minoura et al. 2006; Uno et al. 1996). Ambient nitrogen dioxide and soot decreased significantly, and then remained mostly level for over a decade (Fukushima, 2006; Uno et al. 1996), although localised reduction still occurs in Tokyo (Okubo and Takahashi, 2009; Minoura et al. 2006).

Significant amounts of SPM are transported over Japan during spring and summer from China and Mongolia, due to westerlies occurring as part of synoptic scale low pressure systems (Osada et al. 2007; Minoura et al. 2006; Tsutsumi et al. 2005; Tsutsumi et al. 2004). Late autumn – early winter aerosol peaks in Tokyo and surrounding areas are due to calmer conditions and the photochemical oxidation of car-borne NO (Okubo and Takahashi, 2009; Uno et al. 1996).

The seasonal nature of aerosol concentrations adds another factor to determining days with above average aerosol concentrations. The average concentration of NO_2 and SPM for each month is calculated from the past 8 years of data available from the Japanese Government Ministry of Environment. Using the averages as a basis, the NO_2 and SPM concentrations are classified as being 'clear sky' and 'above average'.

1.3 Scope

Urban pollution is a growing problem in major cities, particularly in the rapidly growing economies of Asia. Issues related to pollution include the effects on visibility, climate, corrosion of structures, local ecosystems and especially on human health.

The cost and inaccessibility of traditional aerosol measuring devices put them out of reach of many researchers and educators, limiting their use to mostly academic and governmental facilities. The limited range of traditional equipment makes them preferable for use in analyses of small sections of the sky. Sky imagers have a much wider range of view, but distort the horizon, and are not portable.

CCD digital cameras, while not being colorimetric devices, have the advantage of being portable, easy to use and cost-effective. Calibration by standardisation experiments and mathematical transformations is required to convert pixel data from sRGB (standard RGB) JPEG camera images to colorimetric CIE standard colour spaces for analysis.

Classification of discolouring aerosols, particularly NO_2 and carbon soot can then be performed through further transformations to the other colorimetric colour spaces used by other researchers (i.e CIE xyY, CIELAB). Comparing observations to documented colorimetric effects of absorption and scattering of discolouring aerosols, analysing these using standard transforms, a CCD camera will be evaluated for aerosol detection and classification.
Colorimetric boundaries for polluted and unpolluted skylight vary from author to author. However, chromaticity trends can be used as a basis for analysis. Unpolluted clear and cloudy skies are blue-green trending; Skies with significant particulate aerosols are 'achromatic trending' and significant nitrogen dioxide aerosol laden skies are yellow-red trending.

1.4 Hypothesis

This research tests the hypothesis that sky images from a calibrated mass-market CCD digital compact camera can provide extensive cost-effective measurements of typical urban discolouring pollutants (NO_2 and carbonaceous aerosols), by producing comparable results to expensive specialised professional equipment (such as light detection and ranging [LIDAR] and radiometers).

2. Methodology

Skylight studies do not involve direct viewing of the sun, thus are more appropriate for studies using a digital camera due to the light sensitivity of the CCD chip (Haralabidis and Pilinis, 2008). Daylight studies include the solar disc in observations requiring significant filtering or blocking, not present with digital cameras. UV and ozone aerosol studies require the use of daylight studies (Haralabidis and Pilinis, 2008; Parisi et al. 2004).

Practical issues affected the experiments. Equipment including sunphotometers and colorimeters that many researchers including Haralabidis and Pilinis (2008) used for comparative studies were very difficult to access in Tokyo and were considerably too expensive to purchase for the evaluative processes in this project. However, Haralabidis and Pilinis (2008) also determined that clear sky colorimetric data collected from such comparative studies should only be used as reference values, as there is significant variance in actual conditions and camera settings.

Parameters considered for this study included site location and altitude, sky conditions when observations were made and the length of time taken for each observation to be taken (Hernandez-Andres et al. 2001). The following sections are physical procedures that were required to gather data; all of them are adapted from previous similar studies.

2.1 Preprocessing

Strict laboratory conditions are not possible for atmospheric observations. Meteorological conditions, observation times and positions relative to the sun affect sky colour and brightness. Furthermore, the properties of the camera, particularly noise response, affect the quality of the image produced. All of these variables must be taken into consideration before data collection.

2.1.1 Data Collection Positions

All observations were made from viewing platforms near central Tokyo, latitude 35°40’N, longitude 139°45’E, elevation 5 m. Azimuth directions are relative to maximum solar elevation for the Northern Hemisphere (south), where the study and the previous studies referenced in this paper are based (mainly in the US, UK, Spain and India).

Observations were made during February to December, 2009, excluding June and July (the author had prior commitments). In this study it has not been practical to obtain pixel data from some directions, due to the presence of tall buildings and the availability of observation platforms.

Each photo was taken with the camera set up on a stable 1.2 metre tripod. A compass was used to maintain consistency with the viewing direction at each of the observation platforms.

The 1st of the 3 viewing areas is the roof of an International School, surrounded by tall buildings (14 storeys and higher) for most of the north, west and east directions; however it has a clear view of the southern and part of the eastern and western skies. On weekends and all days at dawn and dusk, this platform was unavailable due to the school being closed and some other times were unavailable due to the author's teaching schedule.

The 2nd viewing platform is the author's former residence on the 7th floor of an 8 storey building, approximately half a kilometre from the school. In this case, the available viewing directions from the resident's balconies are the north-east, north-west, south-east and south-west skies, the rest being obscured by buildings.

The 3rd viewing platform is a bridge approximately halfway between the other two platforms. The viewing directions are unobstructed due east and west, following the course of the Onagigawa River which it spans. This platform is ideal for observations made at dawn and dusk, particularly dawn as a skyscraper acted as a block to the solar disc at dawn for the duration of the study.

Hernandez-Andres et al (2003; 2001)'s study of the Granada, Spain skylight used comparable viewing directions, taken at 0°, 45°, 90° and 315° relative to the sun's azimuth during maximum solar elevations, these correspond to south, south-west, west and north-east directions.

Sloane's (1988) models of discoloration of skylight due to increased soot and NO_2 concentrations were focused on 0° and 30° to the sun's azimuth during maximum solar elevation occurring in late spring and summer, these correspond to south and south-west from sun azimuth.

Lee Jr. and Hernandez-Andres (2003) and Lee Jr. (1994) took their twilight measurements in the sun's direction, corresponding to approximately east and west for dawn and dusk respectively. This was the basis for choosing the 3rd viewing platform.

Although Hernandez-Andres et al. (2001) took measurements at 15° intervals between elevations of 15° and 165°, several authors, such as Lee Jr, and Hernandez-Andres (2003) and Lee Jr. (1994) confined their measurements to within 20° of the horizon during twilight and used to measure the purple due to the earth's shadow on the atmosphere, that is often seen at those times.

Sloane's midday models were constrained by what is referred to as the 'horizon' (1.5°) and as 'elevated' (20°). This range is well within the field of view for the camera used in the study and was approximated by selecting 20 pixels from sky photos in a line from the horizon upwards. The line of pixels was taken from a clear space, in the centre of each sky photo. The reference points used were distant buildings.

2.1.1.1 Relative Air Mass

Relative air mass or optical mass is a measure of the relative amount of air that light must propagate through to the observer, (Darula and Kittler, 2002; Kasten and Young, 1989; MacAdam, 1981). Observations made closer to the horizon are subject to greater air mass, longer path length of light and increased effects of scattering and absorption (Haber et al. 2005; Preetham et al. 1999; MacAdam, 1981).

The main consequence of a longer light path length is that shorter wavelengths of light (blue) are preferentially absorbed and scattered away from the observer, resulting in the yellow-red shifted colours seen at dawn and dusk (Haber et al. 2005; Dogras et al. 2002; MacAdam, 1981).

Kasten and Young (1989) developed lookup tables calculating relative air mass for varying solar elevation angles used to compare results in this study. These comprehensive tables form the basis for classifications of midday and dawn-dusk data used for this study. In this study, midday data is defined by a relative air mass of <2, equivalent to elevation angles <30°, as these correspond to maximum solar elevations throughout duration of the observations in Tokyo. Dawn-dusk data is defined by relative air masses >5.5, equivalent to solar elevation angles of >10°, the reason was based on being within an hour of civil twilight.

The only exceptions to these classifications are the photos taken from the 1st viewing platform at the time when ash from the Mt. Asama eruption was reportedly over Tokyo (Kubota and Fujioka, 2009) and mid-morning and mid-afternoon pictures taken to help generate overall colorimetric models of the Tokyo sky.

2.1.2 Daily Observation Times

Changes in colour occurring from a card of known reflectance properties were tested by Romero et al. (2003) at civil twilight to maximum solar elevation during different conditions. Similar colour differences also quantify perceptions of colour shifts due to haze (Mahadev and Henry, 1999). However, it was found by Hernandez-Andres et al. (1999) that regardless of the time of day or air quality, sky colorimetric data still follows the same quantifiable gamut.

Direct midday zenith viewing used in some prior studies is damaging to the CCD sensor in digital cameras. Often studies involving zenith measurements have a moving solar block (Sabburg and Wong, 1999). However, this is impractical for the digital camera, given the different orientations, range of positions, settings and photographic sensitivities. Despite this, sky photos were taken at dawn, around midday and at dusk, with only a few taken mid-morning and mid-afternoon.

2.1.3 Meteorological Conditions

Many skylight models and observations involve the assumption of a cloudless sky (Hernandez-Andres, 2001; Sloane, 1988). However, this is not always possible. Lee Jr. and Hernandez-Andres (2005) measured the colours of the overcast sky, specifically conducting their observations when clouds have sufficient optical thickness so that shadows are not cast. In these previous studies it was found that the data still fit on the same colorimetric gamut as clear and hazy skies, the same assumption is used in this study.

2.1.4 Camera

The camera used in the study is the Canon Powershot G10, having up to 20 times optical zoom and a resolution of 14.7 megapixels arranged 4416 by 3312 pixels on the standard 1/1.7" type CCD sensor (Carlson, 2010; Canon). The actual sensor size is 7.6 mm wide by 5.7 mm high (Fink, 2008). Each pixel is a square with side lengths and area of approximately 1.7 μm and 2.96 μm^2 respectively.

The G10 is a modern digital compact camera with similar features to many, more expensive SLR cameras including auto white balance and increased noise reduction (Carlson, 2010). Recently, the G10 has been superseded by the G11 and G12 models. The Canon G10, like most digital cameras is based on 24 bit sRGB (standard RGB) colour space with a white point D_{65}, approximating daylight (Kerr, 2010).

The total field of view (FOV) of the canon Powershot G10 is approximately 0.3π steradians (64° by 50°), considerably less than a Whole Sky Imager that encompasses the entire 2π steradian sky dome (Lee Jr, and Hernandez-Andres, 2005; Shields et al. 1998). A fish eye lens would allow the Canon G10 to have the same FOV as a Whole Sky Imager, but would have chromatic distortion on the horizon.

Spectroradiometers, commonly used in the literature for atmospheric observations, typically have had a viewing FOV of 1° diameter, corresponding to an approximate solid angle of 1 millisteradian (Lee Jr. 2008; Buluswar and Draper, 2001). Each pixel of the Whole Sky Imager used by Shields et al. (1998) has a FOV of 34 microsteradians, whereas the Canon G10's pixels have a FOV of approximately 80 nanosteradians (just less than 1 arc minute).

2.1.4.1 Camera Settings

Many digital camera based air quality studies use a fish eye lens, including UV-cloud observations made by using a Total Sky Imager by Sabburg and Wong (1999). However, this method is unsuitable for any horizon measurements owing to distortion due to the lens itself (Spasojevic and Mahdavi, 2005). A

photo taken with a digital camera that includes the horizon and a significant proportion of the sky in view can cover a significant range of elevation angles.

Calibration of CCD digital cameras is a necessary step, as the colour responses are device dependent rather than colorimetric and are manufactured to produce crisp, aesthetically pleasing pictures rather than scientific imagery (Wuller and Gabele, 2007; Spasojevic and Mahdavi, 2005; Orava et al. 2004; IEC, 1999). There are a few components within a digital CCD camera that potentially cause errors that are either very difficult or not practically feasible to correct, but nonetheless must be considered.

Photographic parameters, including shutter speed, f-number/aperture and ISO number, are recorded as the digital image's Exif (Exchangeable information file) data which can be accessed by viewing the image's properties.

- Exact values of aperture (f-number) and exposure time are recorded as part of the camera's Exif data. However, discrepancies may exist between these two components' diameters and times respectively due to inherent limitations in the accuracy of the camera's mechanical components, (Wuller and Gabele, 2007).

- ISO speed depends on the quantum or photon capture efficiency of the camera, which relates to the physical size of the pixel and the depth of the electron collecting potential well on the CCD chip. Less CCD sensor noise occurs at minimum ISO values (Jacobson et al. 2000). The values recorded in Exif data are not always accurate. For example, ISO100 is often more likely to be ISO80 (Wuller and Gabele, 2007).

- Pixel colour data accuracy can potentially be lowered through rounding error in converting to digital output signals (Wuller and Gabele, 2007).

- Vignetting, image and associated chromatic distortion, usually occurs near the edges of a photo (Wuller and Gabele, 2007). This is not a major consideration, as all pixels are selected from near to the centre of an image.

- All tests used auto white balance settings, as is standard in several studies (Wuller and Gabele, 2007; IEC, 2003; Martinez-Verdu et al. 2003).

2.1.4.2 Noise Calculations

Noise is caused by unwanted, yet not completely unavoidable light intensity and thermal fluctuations across the imaging sensor (Brady and Legge, 2009; Imatest, 2009; Jacobson et al. 2006). Noise is a significant factor in this study, as averaged or "demosaicked" pixel data taken from sky photos may have noise-related errors in observed colorimetric shifts (Haralabidis and Pilinis, 2005).

Colour accuracy is often sacrificed for noise reduction and higher resolution. This is a particularly pertinent consideration in selecting a camera for scientific

use; despite all images taken during the study were at low ISO levels where image noise is at a minimum (Jacobson et al. 2006; Holm et al. 2003).

There are several types of noise. Some types of noise are defined differently depending on the field of study in which they are observed, an attempt is made here to describe each type with reference to other terminology uses.

- Random or readout noise is a generally unobtrusive irregularly spaced noise or graininess most prominent at high ISO levels (Imatest, 2009; Wuller and Gabele, 2007; McLean, 1997). Random noise can be defined statistically, but not systematically owing to the intrinsic unpredictability of its effects (Jacobson et al. 2006; McLean, 1997). The effects of random noise can actually even enhance the picture (Yoshida, 2006).

- Spatial noise mainly affects still pictures, or a 'snapshot' of a moment in temporal noise (Jacobson et al. 2006). Temporal noise describes fluctuations that can occur randomly over time and can be reduced by frame averaging (Imatest, 2009; Kodak, 2005). Spatial noise tends to have a regular pattern, and as such, is referred to as 'fixed pattern' noise (Imatest, 2009; Wuller and Gabele, 2007; Yoshida, 2006).

- Thermal noise or 'hot pixels' is often considered a type of temporal noise, as the temperature fluctuates as a function of time (Kodak, 2005). Resistance from electrical amplifier functions in the camera cause this type of noise, often referred to as 'dark current' (Brady and Legge, 2009; Wuller and Gabele, 2007; Jacobson et al. 2006; Kodak, 2005; McLean, 1997). Dark current can be lessened by cooling but not completely removed (Yoshida, 2006; Kodak, 2005). Thermal noise also occurs as a minor result of sky observations, where cooling has no effect on the final result (Haralabidis and Pilinis, 2005).

- Photon shot noise is due to the unavoidable random arrival of photons on the sensor (Wuller and Gabele, 2007; Kodak, 2005). Smaller pixel sizes provide greater resolution at the expense of an increase in this type of noise (Wuller and Gabele, 2007; Holm et al. 2003). A consequence of the large number of pixels in the Canon G10 (14.7 megapixels) used in this study is that each pixel size is smaller, and therefore fewer photons can reach each pixel. Thus, this CCD is potentially more prone to random fluctuations of photon quanta (Wuller and Gabele, 2007; Jacobson et al. 2006; Yoshida, 2006; Kodak, 2005; Holm et al. 2003).

Signal to noise ratio (SNR) is a true measure of the effectiveness of a system to transmit information (Jacobson et al. 2006), where

$$SNR = 20\log\left(\frac{S}{N}\right)\text{(dB)}, \qquad (1)$$

where S is the signal and N is the noise (Imatest, 2009).

With the development of the Digic IV chip, Canon claims to have significant noise reduction compensates for the smaller pixel size that would normally result in increased photon shot noise (TechTarget, 2009). The Digic IV chip is often used in Canon's SLR camera range and is included in the G11 and G12 models. It is not clear how this technology works and at the time of writing, Canon had not explained the technical details.

An effective means to determine the signal to noise ratio of a camera is to use a standard card with known digital values (Imatest, 2009). A Kodak Q13 grayscale card (Figure 2.1) was used to measure the SNR in controlled conditions according to IEC international standards (2003) compared to hazy conditions representative of a polluted day in Tokyo.

Imatest Stepchart was then used to calculate the SNR for red, green, blue and brightness (Y) channels of each part of the Q13 standard. The three primary colour SNR values were factored into the 'Y" channel, providing an indication of the overall noise level affecting the CCD sensor.

Figure 2.1: Kodak Q13 Gray Scale card (Arizona Digital Imaging Institute). Each step to the left represents an increase in digital number.

For constancy, in both tests the camera had the same ISO speed, f-stop number and exposure time (Wuller and Gabele, 2007; IEC, 2003). However, the settings for f-stop and exposure time often are not exactly the same as what is set on the camera, due to inherent mechanical errors (Wuller and Gabele, 2007).

For the controlled test, the Kodak Q13 grayscale stepchart is uniformly illuminated by 2 x 3200 K globes, 1.5 m distant and viewed through an 80A color corrective filter, so that the image is viewed as the daylight standard 5500 K (Jacobson et al. 2000). Five identical images were averaged to improve the accuracy of the signal to noise ratio (Imatest, 2009).

A separate experiment using clear skylight as the light source illuminating the grayscale chart, without the colour correction filter was performed during hazy conditions (modified from Lim et al. 2004). The presence of haze potentially contributes a significant amount of noise by adding 'airlight' to the path of light through the combined and random effects of aerosol scattering, increasing noise, and by absorption, attenuating the signal (Hyslop, 2009; Haralabidis and Pilinis, 2005).

2.2 Data Collection

The main method for data collection was to take a photo keeping the horizon at approximately the centre of the picture. Meteorological conditions and aerosol concentrations are recorded, the latter to classify the ambient air quality. Each photo then has 20 pixels selected from the horizon; these are then broken down to their red, green and blue components.

2.2.1 Meteorological and Aerosol Data

Hourly meteorological and aerosol data are recorded and made publicly available by the Tokyo Ministry of Environment. The data includes meteorological aspects such as temperature, humidity, wind speed and direction; Aerosol data includes the concentrations of nitrogen oxides, separated into nitrogen monoxide and nitrogen dioxide, sulphur dioxide, suspended particulate matter (SPM), ozone, methane and non-methane hydrocarbons.

It was not possible to directly access meteorological and aerosol sampling equipment maintained by the Japan Meteorology Agency and the Tokyo Ministry of Environment. However, suitable data for this study were retrieved from a Government monitoring station approximately 2 km from where the observations were taken. Whilst the monitoring station was very close to the viewing platforms, other, more local factors may have affected the aerosol concentrations, particularly local traffic conditions.

2.2.1.1 Concentration classifications

Monthly aerosol concentration data for the past 8 years are made available on the Japanese Government's Ministry of Environment website. The mean for each month (Table 2.1) forms the basis for determining 'clear sky' for concentrations equal or less than the average and 'elevated concentration' for above the average.

Table 2.1: 8-year mean monthly discolouring aerosol concentrations for Tokyo (Ministry of Environment, Japanese Government). Seasonal peaks are highlighted.

	NO_2 (ppb)	SPM ($\mu g/m^3$)
Jan	30	24
Feb	31	25
Mar	29	27
Apr	29	31
May	26	28
Jun	29	29
Jul	25	30
Aug	23	28
Sep	24	25
Oct	29	27
Nov	35	32
Dec	34	28

Opposing seasonal trends in NO_2 and SPM concentrations are very apparent in Table 2.1. SPM concentrations peak mainly during the spring and summer, this increase is described by Osada et al. (2007); Minoura et al. (2006); Tsutsumi et al. (2005, 2004), as a result of Yellow or Kosa dust events originating in China and Mongolia. These seasonal peaks coincide with troughs in NO_2 concentrations that in turn, peak during autumn and winter described in part by Yoshikado and Tsuchida (1996).

2.2.1.2 Volcanic Ash Observations

On the day after the volcanic eruption of Mt. Asama, ash was reported over the Tokyo Metropolitan area (Kubota and Fujioka, 2009). The observation for volcanic ash coincided with above average aerosol NO_2 and approaching average SPM concentrations during a cloudy morning. Pixel data for this event were collected in the same way as for other sky photos.

2.2.2 Pixel Data

The pixel data used in this study are generated by the camera as 24-bit sRGB format images. RGB pixel data were then obtained from digital JPEG images using Matlab and Scilab, which is then imported into Microsoft Excel where all numerical analyses are completed. It is not possible to exactly reconvert the original device output data to exact CIE XYZ values due to internal camera errors and JPEG compression, (Wuller and Gabele, 2007).

The International Electrotechnical Commission (IEC) defines standard procedures for converting device dependent sRGB to colorimetric CIE XYZ which were applied to sky images from this study, (Hunt, 2006; Martinez-Verdu et al. 2003; Ohno, 2000; IEC, 1999).

2.3 Data Analysis

2.3.1 Colorimetric Transformations

Digital still cameras are not colorimetric, so all pictures taken in this study require transformation from device dependent RGB pixel data to device independent, colorimetric CIE XYZ (Kerr, 2010; Haralabidis and Pilinis, 2008; Huynh and Robles-Kelly, 2007; Spasojevic and Mahdavi, 2005; Pujol et al. 2004). Hue angle based on raw pixel RGB and that is gamma-invariant to brightness and gamma corrections were used to compare the effect of colorimetric transformations (Schaefer and Finlayson, 2001).

Skylight colorimetric data are most often transformed using the CIE XYZ, CIELUV and CIELAB colour spaces and CIELCH colour differences (Haralabidis and Pilinis, 2008; Kerr, 2008; Wuller and Gabele, 2007; Ben Chouikha et al. 2006; Lee Jr. and Hernandez-Andres, 2005; Orava et al. 2004; Pujol et al. 2004; Martinez-Verdu et al. 2003; Romero et al. 2003; Mahadev and Henry, 1999; Lee Jr 1994; Sloane 1988).

Digital still cameras when properly calibrated provide luminance distributions and ratios across a scene, but not absolute luminance (Wuller and Gabele, 2007). There are relatively few studies that address the angular distribution colorimetry of clear sky and these are arguably just as important as radiance studies in areas such as spectrally sensitive photovoltaic systems and camera vision (Hernandez-Andres et al. 2001). Camera vision considerations are also becoming more important for the growing camera phone market.

All colorimetric transformations make reference to a 'white point' or a point of 'equal energy' of known values (Kerr, 2010; Kerr, 2008; Hunt, 2006). In past studies, the white points used were referred to as B and C, possessing colour temperatures of 4874K and 6774K respectively (Wyszecki and Stiles, 2000; MacAdam, 1981). However, recent studies including those from Kerr (2010, 2008), Hunt (2006), Lee Jr. and Hernanadez-Andres, (2005) and Sloane, (1988) use a daylight standard D_{65}, with a colour temperature of 6504K. D_{65} is the designated white point for the sRGB colour space used in most digital cameras, including the Canon G10 (Kerr, 2010; IEC, 1999).

2.3.2 Metrics

Several mathematical transformations are required to convert device dependent sRGB values into useful colorimetric and colour difference data. These processes are detailed in the following sub-chapters and the complete processes are summarised at the end in Figure 2.6.

2.3.2.1 CIE XYZ

sRGB pixel values are normalised by dividing by 255 to be between 0 and 1. A gamma correction needs to be applied to the normalised RGB (red green blue) values to make them linear before they are converted to CIE XYZ (Kerr, 2010; Orava et al. 2004; Pujol et al. 2004). This process is outlined by the international standard IEC (International Electrotechnical Commission) 61966-2.1 (1997).

A constant gamma correction of 2.4 is used as a standard if the normalised *RGB* values (denoted as *R'G'B'* in equation 2) are all above 0.03928 (Kerr, 2010; IEC, 1997). The constant is used despite this factor altering due to viewing conditions, camera type and settings (IEC, 1997,

$$RGB_{linear} = \begin{cases} \dfrac{R'G'B'}{12.92}, & R'G'B' \leq 0.03928 \\ \left[\dfrac{(R'G'B'+0.055)}{1.055}\right]^{2.4}. \end{cases} \quad (2)$$

where RGB_{linear} represents the gamma corrected (linear) red, green and blue digital values. *R'G'B'* are normalised raw red, green and blue digital values as described above. RGB_{linear} values are then transformed by matrix multiplication to attain corresponding colorimetric CIE XYZ values as in equation 3 (for simplicity, RGB_{linear} is labelled just as *RGB*):

$$\begin{bmatrix} X \\ Y \\ Z \end{bmatrix} = \begin{bmatrix} 0.4124 & 0.3576 & 0.1805 \\ 0.2126 & 0.7152 & 0.0722 \\ 0.0193 & 0.1192 & 0.9505 \end{bmatrix} \begin{bmatrix} R \\ G \\ B \end{bmatrix}. \quad (3)$$

From the matrix transform in equation 3, Wuller and Gabele (2007) equated the luminance function (Y_{CIE}) as being the linear transform for CIE Y,

$$Y_{CIE} = 0.2126R_{linear} + 0.7152G_{linear} + 0.0722B_{linear} \quad (4)$$

where the luminance function (Y_{CIE}) is a weighted sum of gamma corrected (linear) red, green and blue digital values.

Discrimination between pixel brightness and luminance levels compared to clear sky and relative to the sun's position can provide one of the means for determining attenuation and discoloration (Sabburg and Wong, 1999), but needs to be an averaged pixel effect (Wuller and Gebele, 2007).

2.3.2.2 CIExyY (1931)

CIE XYZ data are then converted to CIE xyY (1931) for presentation and analysis on a chromaticity xy diagram used in many sky colour studies (Figure 2.2), where Y is the luminance and x is red-trending (equation 5) and y is green-trending (equation 6) (Kerr, 2010; Malacara, 2002; Dogras et al. 2002; Ohno, 2000; Ford and Roberts, 1998; Sloane, 1988),

$$x = \frac{X}{X + Y + Z}, \tag{5}$$

$$y = \frac{Y}{X + Y + Z}, \tag{6}$$

$$Y = Y. \tag{7}$$

where X, Y and Z are CIE XYZ values derived from equation 3. The luminance function used in the CIE xyY is the same as derived in equation 4.

CIE xy coordinates are used to calculate a skylight gamut (Hyslop, 2009; Hernandez-Andres et al. 2001; Wyszecki and Stiles, 2000; Hernandez-Andres et al. 1999; Judd et al. 1964). A colorimetric gamut is effectively a trendline that best fits, thus describes groups of colorimetric data.

The gamut derived from the data was then compared to the CIE Standard Daylight locus and the Planckian locus of blackbody correlated colours (Figure 2.2), (Hernandez-Andres et al. 2001; Herndandez-Andres et al. 1999; Judd et al. 1964).

The x and y axes represent red and green trends respectively with low values of both representing blue trending (Hunt, 2006; Malacara, 2002; Ohno, 2000; Wyszecki and Stiles, 2000).

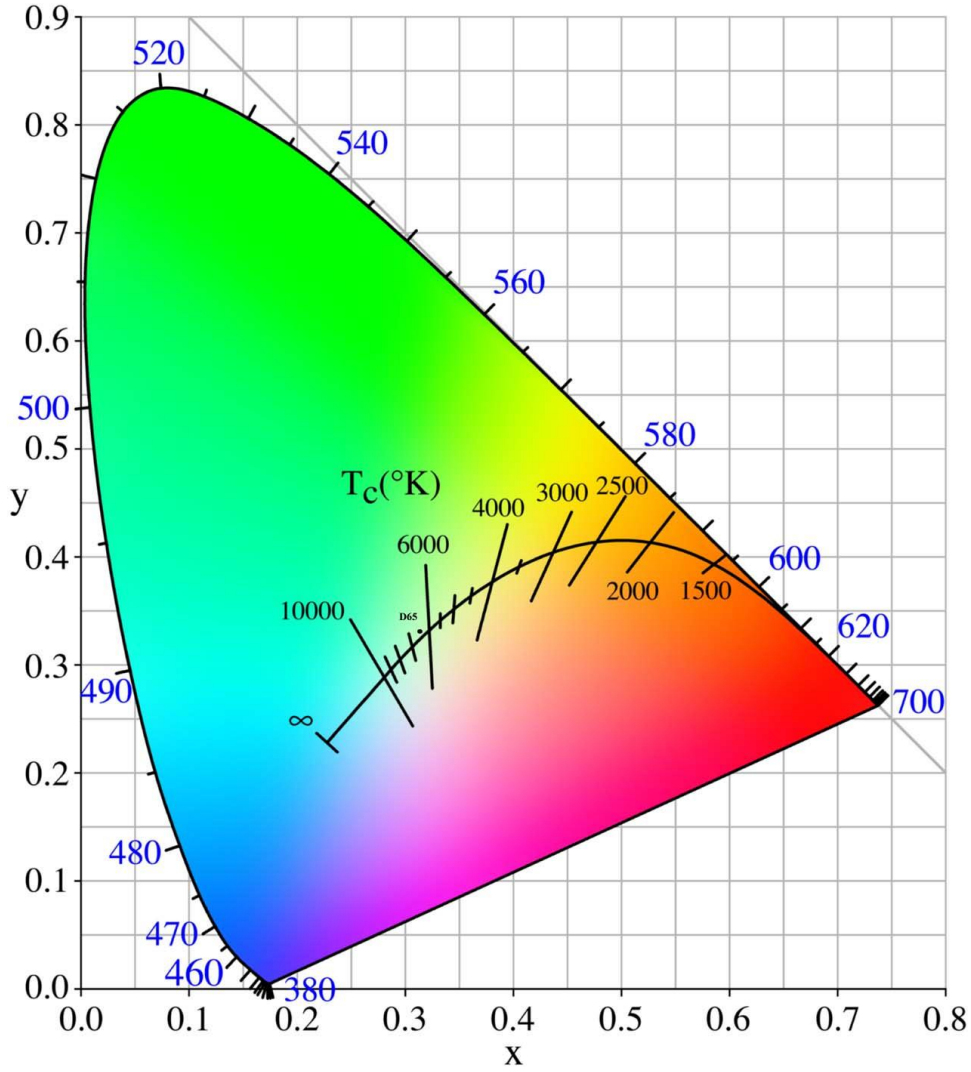

Figure 2.2: CIE xy (1931) chromaticity diagram representing all of the colours and Planckian locus, surrounded by spectral wavelengths (nm) (Hancock Technologies).

Correlated Colour Temperatures (CCT's), labelled as 'T_c (K)' in Figure 2.2 are representative of the CIE xy chromaticity coordinates of Planckian blackbody radiators (Wyszecki and Stiles, 2000). The data for Planckian locus correlated colour temperatures and their corresponding chromaticity coordinates were obtained from Charity (2001) and Wyszecki and Stiles (2000). This locus is used as a reference as many results, including those of natural light have spectral power distributions close to or the same as its chromaticity coordinates (Wyszecki and Stiles, 2000; Hernandez-Andres et al. 1999).

Studies conducted by the CIE in the United States, Canada and England defined the Daylight Locus, which tends to be almost parallel to, but slightly more green than the Planckian Locus (Buluswar and Draper, 2001; Hernandez-Andres et al. 2001; Wyszecki and Stiles, 2000; Hernandez-Andres et al. 1999; Judd et al. 1964). A total of 622 clear and cloudy sky skylight and daylight observations were made by the CIE in the United States, Canada and England across the

different phases of the day during the early to mid 1960's (Buluswar and Draper, 2001; Wyszecki and Stiles, 2000; Judd et al. 1964).

The results of these studies were plotted and the equation for the CIE Daylight locus was calculated as being,

$$y_D = -3.000x_D^{\,2} + 2.870x_D - 0.275, \tag{8}$$

where there is a negative quadratic relationship between the parameters *x* and *y*. This gamut runs almost parallel with, but above the Planckian locus.

The CIE Daylight standard is greener than the equivalent blackbody (Planckian) locus, this is normal for the Northern Hemisphere, but the reverse has been found to be true for the Southern Hemisphere for reasons that are not clear (Buluswar and Draper, 2001; Wyszecki and Stiles, 2000).

The standard white point used, D_{65} (6504K) is derived from this locus having xy chromaticity coordinates of 0.3127, 0.3290 in the achromatic centre of the CIE xyY diagram as in figure 2.2 (Malacara, 2002; Buluswar and Draper, 2001; Hernandez-Andres et al. 2001; Wyszecki and Stiles, 2000).

The parameter Y also represents 'brightness', and has the same value as it does in the CIE XYZ metric detailed in equation 4 (Hunt, 2006; Malacara, 2002; Wyszecki and Stiles, 2000). This parameter is not often used in atmospheric studies as it has been superseded by the more modern colour space relative luminance parameter *L**.

2.3.2.3 CIE Uniform Colour Spaces (1976)

2.3.2.3.1 CIE u'v'Y

The CIE 1976 UCS colour space (Figure 2.3) describes a uniform distribution of chromaticity coordinates than the earlier CIE xyY and superseded an earlier now deprecated CIE u'v'Y (1960) system of coordinates (u, v) (Kerr, 2010; Hunt, 2006; Malacara, 2002; Ohno, 2000; Wyszecki and Stiles, 2000; Ford and Roberts, 1998),

$$u' = \frac{4x}{-2x + 12y + 3}, \tag{9}$$

$$v' = \frac{9y}{-2x + 12y + 3}. \tag{10}$$

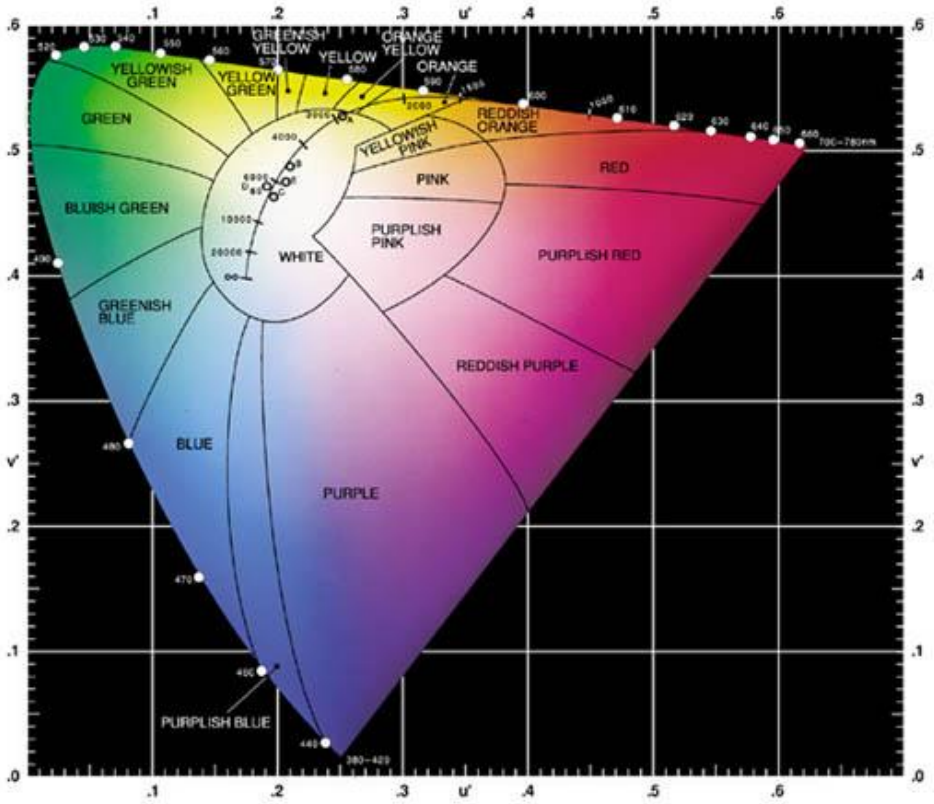

Figure 2.3: CIE u'v'Y (1976) chromaticity diagram representing all of the colours, spectral wavelengths and Planckian locus (Nave, nd).

Kerr (2010, 2008) suggests the use of differences between the u' and v' coordinates and a designated reference point as a colour difference vector (with the subscripts 1 and 2 respectively). The reference used is the chromaticity coordinates for clear blue sky determined by Wyszecki and Stiles (2000),

$$du' = u'_2 - u'_1, \tag{11}$$

$$dv' = v'_2 - v'_1, \tag{12}$$

where *du'* and *dv'* are colour differences from the reference point.

CIE u'v'Y chromaticity coordinates derived from the CIE xy coordinates presented by Wyszecki and Stiles (2000) for a 'clear blue sky' with a correlated colour temperature of 15,000K were used as the reference in this study. Increasing du' and dv' values represent trends towards red and yellow respectively.

Average colour differences will be evaluated for midday and dawn-dusk data separated by air quality conditions – clear sky, above average NO_2 and above average NO_2 and SPM. From each sky photo, the data selected will be the bottom 3 pixels, approximating Sloane (1988)'s colorimetric models for the 'horizon' and the upper 3 approximating her 'elevated' positions.

Kerr (2008) and Lee Jr. (2008) use a single metric to determine chromaticity difference and in discrepancies in error calculations:

$$\Delta u'v' = \sqrt{\left(\Delta u'\right)^2 + \left(\Delta v'\right)^2} \,. \tag{13}$$

2.3.2.3.2 Just Noticeable Differences

In order to improve on inconsistent perceived colour change threshold studies, during the 1940's, MacAdam performed experiments to gauge visual sensitivity to small colour and luminance differences using CIE xyY chromaticity coordinates as a basis (Hunt, 2006; Malacara, 2002; Wyszecki and Stiles, 2000; Brown and MacAdam, 1949; MacAdam, 1942).

Just noticeable difference projections on colour spaces are known as 'MacAdam Ellipses' and are still in use today, still forming the basis of perceived 'just noticeable differences' (JND) in colour used in the CIE xyY and easily converted to the CIE u'v'Y (1976) colour spaces shown in Figure 2.4 (Lee Jr. 2008; Hunt, 2006; Wyszecki and Stiles, 2000).

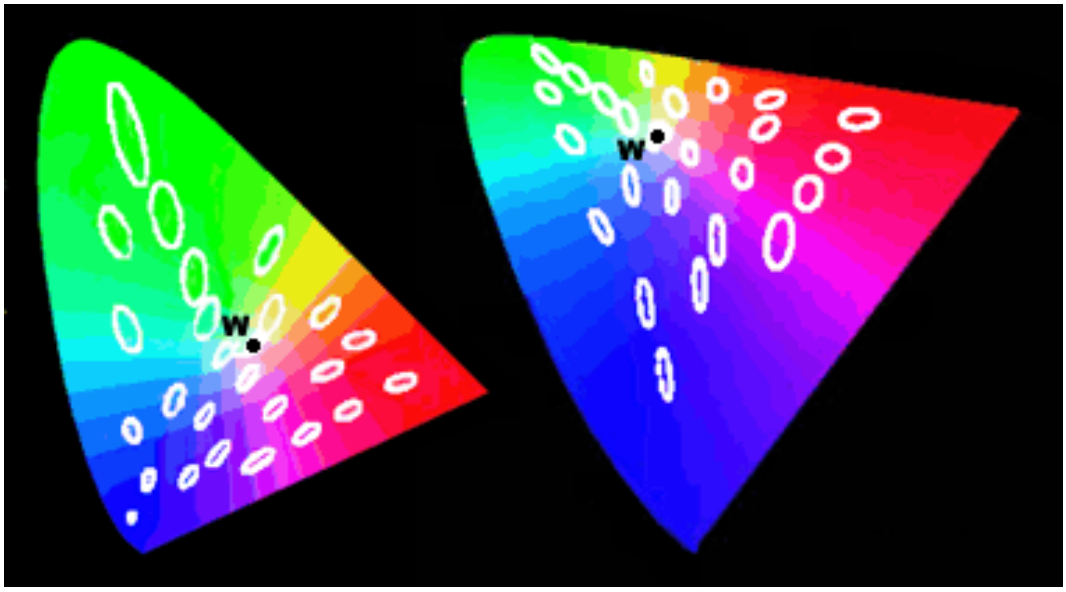

Figure 2.4: MacAdam Ellipses (each ellipse magnified 10 times for clarity) shown on the CIE xyY (left) and on the CIE u'v'Y (right) diagrams (MacEvoy, 2009). W represents the D_{65} white point.

Although still not exact, the CIE u'v'Y diagram allows for perception generalisations. MacAdam Ellipses are generally estimated to be $\Delta u'v' \approx 0.002$ (Kerr, 2008; Lee Jr. 2008). The relative luminance function has a just noticeable difference defined as $L^* < 2\%$ (Hernandez-Andres et al. 2003).

2.3.2.3.3 CIE LUV

CIE LUV has the same colour tendency is derived from the CIE u'v'Y colour space (Kerr, 2010; Hunt, 2006; Malacara, 2002; Wyszecki and Stiles, 2000; Ford and Roberts, 1998). This colour space was developed for use in digital technologies (Hunt, 2006; Malacara, 2002; Wyszecki and Stiles, 2000).

$$u^* = 13L^* \cdot \left(u' - u'_n\right), \tag{14}$$

$$v^* = 13L^* \cdot \left(v' - v'_n\right), \tag{15}$$

where u_n' and v_n' are the CIE u'v'Y white point coordinates.

L^* describes lightness or relative luminance or 'lightness', 'value' or 'intensity',

$$L^* = 116 \cdot f\left[\frac{Y}{Yn}\right] - 16, \tag{16}$$

where,

$$f(s) = \begin{cases} 7.787s + \dfrac{16}{116}, & s \leq 0.008856 \\ s^{\frac{1}{3}} \end{cases}. \tag{17}$$

The parameter '*s*' represents the ratio of the measured *Y* value with the white point value Y_n. For the D_{65} white point, Y_n is 100.

It is clear that there is a cube root relationship between brightness (Y) and relative luminance (L*) where the ratio between the measured brightness to the white point is above 0.008856. Ratios less than or equal to 0.008856 are linear, as can be observed in equation 17, (Hunt, 2006; Malacara, 2002; Ohno, 2000; Wyszecki and Stiles, 2000).

2.3.2.3.4 CIE LAB

The CIELAB colour space describes the colour tendency from purplish-red to green (a*) and yellow to blue (b*). This colour space is mainly used for textiles and plastics, but also has been applied to aerosol studies (Kerr, 2010; Hunt, 2006; Romero et al. 2003; Malacara, 2002; Ohno, 2000; Wyszecki and Stiles, 2000; Ford and Roberts, 1998).

$$a^* = 500 \cdot \left[f\left(\frac{X}{Xn}\right) - f\left(\frac{Y}{Yn}\right) \right], \tag{18}$$

$$b^*=200\cdot\left[f\left(\frac{Y}{Yn}\right)-f\left(\frac{Z}{Zn}\right)\right], \quad (19)$$

where X_n, Y_n and Z_n are the CIE XYZ white point values. The internal functions, denoted *f(s)* follow equation 17, where *s* represents the ratio of the CIE XYZ value with its respective white point value.

2.3.2.3.5 Color Differences ΔE

Colour differences (ΔE) can also be calculated from CIE LAB (Kerr, 2010; Hunt, 2006; Malacara, 2002; Wyszecki and Stiles, 2000; Ford and Roberts, 1998),

$$\Delta E_{LAB}=\sqrt{\left(\Delta L^*\right)^2+\left(\Delta a^*\right)^2+\left(\Delta b^*\right)^2}, \quad (20)$$

where

$$\Delta L^*=L^*-L^*_{ref}, \quad (21)$$

$$\Delta a^*=a^*-a^*_{ref}, \quad (22)$$

$$\Delta b^*=b^*-b^*_{ref}, \quad (23)$$

where the 'ref' subscript refers to any reference point, usually the colour space's white point (Malacara, 2002).

Colour differences can also be calculated from the CIE LUV colour space by substituting u* and v* parameters in place of a* and b* respectively in equations 20, 22 and 23. L* is calculated and is defined in the same way as for the CIE LAB colour space, (Kerr, 2010; Hunt, 2006; Malacara, 2002; Wyszecki and Stiles, 2000).

2.3.2.3.6 CIE LCh

Polar coordinates describing the saturation or chroma (C^*_{AB}) and hue angle (h^*_{AB}) are also derived from the CIE LAB and CIE LUV colour spaces, in a separate CIE LCH colour space (Figure 2.5) (Kerr, 2010; Hunt, 2006; Romero et al. 2003; Malacara, 2002).

$$C^*_{AB}=\sqrt{\left(a^*\right)^2+\left(b^*\right)^2}, \quad (24)$$

$$h^*_{AB}=\tan^{-1}\sqrt{\left(\frac{b^*}{a^*}\right)}. \quad (25)$$

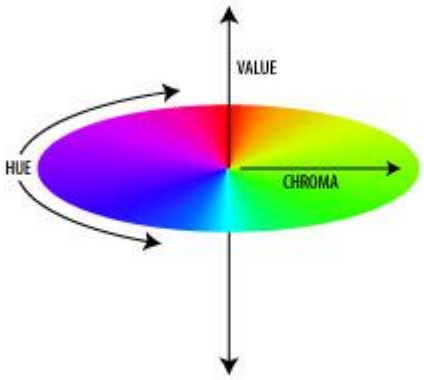

Figure 2.5: Diagrammatic relationship between hue angle, chroma (saturation) and luminance (value = L*) (Adobe, 2000).

Chroma describes how 'rich' or 'pure' a colour is. Low chroma values describe greys, higher values describe rich spectral colours and purples (Wyszecki and Styles, 2000). The calculation to derive chroma (Equation 24), gives the 'magnitude' of the CIELAB colour space vector for that pixel. Thus, averaging the chroma for pixels from the same air quality condition will give an average 'depth' of colour for comparison.

Hue angle is measured from the +a* axis anticlockwise from the CIE Lab colour space chart (Hunt, 2006; Wyszecki and Stiles, 2000). Hue angle difference (ΔH^*_{AB}) (Malacara, 2002; Wyszecki and Stiles, 2000), is equated to:

$$\Delta H^*_{AB} = \sqrt{\left(\Delta a^*\right)^2 + \left(\Delta b^*\right)^2 - \left(\Delta C^*_{AB}\right)^2}\,, \tag{26}$$

where Δa^* and Δb^* are described by equations 22 and 23 respectively and

$$\Delta C^*_{AB} = C^*_{AB} - C^*_{ABref}\,. \tag{27}$$

Hue angle, hue angle difference and chroma can be calculated from the CIELUV colour space in a similar manner to that for CIELAB by substituting u* and v* for a* and b* respectively (Hunt, 2006; Malacara, 2002; Wyszecki and Stiles, 2000). Despite their different intended uses, both have been widely used in atmospheric aerosol studies (Brady and Legge, 2009; Lee Jr and Hernandez-Andres, 2005; Romero et al. 2003; Hernandez-Andres et al. 1999). Hue angle is analogous to and is used to calculate the dominant wavelength (Hunt, 2006).

Saturation is another metric that can be measured only from the CIELUV colour space (Hunt, 2006; Malacara, 2002; Wyszecki and Stiles, 2000). Objectively, saturation is also referred to as 'purity' (Hunt, 2006), it is equated as,

$$s_{uv} = \frac{C^*_{uv}}{L^*}\,. \tag{28}$$

CIELCh derived from CIELUV is favoured over that from CIELAB, as it is derived from the equal area CIE u'v'Y colour space related to the perception of light (Kerr, 2010; Malacara, 2002; Wyszecki and Stiles, 2000).

Chromaticities of constant hue angle plotted on the CIE xy and CIE u'v' diagrams form curved lines from the colour space's white point to the spectral boundary (Lillo et al. 2002; Wyszecki and Stiles, 2000). Dominant wavelengths are a more readily understandable means to describe hue angle (Lillo et al. 2002). It was expected that the data from Tokyo sky images will follow this schema.

2.3.2.3.7 Dominant Wavelength

Correlating hue angle to its equivalent dominant wavelength is usually measured by extending a line from the white point, through the data chromaticity point until it reaches a point on the spectral boundary (Kerr, 2010; Hunt, 2006; Malacara, 2002; Wyszecki and Stiles, 2000). However, this method is impractical when dealing with large numbers of chromaticity points, especially if they are close together as is the case for many atmospheric studies (Lee Jr. and Hernandez-Andres, 2003; Hernandez-Andres et al. 2001; Wyszecki and Stiles, 2000; Lee Jr. 1994).

A useful method would be to quantify a mathematical relationship between hue angle and dominant wavelength; however, this is very difficult given the complexities of colour space curves as in figures 2.2 and 2.3. There have been attempts in quantifying dominant wavelengths from chromaticities, such as the formula to determine the dominant wavelength of red wine developed by Heredia and Chozas (1992).

In Heredia and Chozas' model, they formulated an equation derived from the CIE xy colour space to describe red wavelengths pertinent to the wines they were testing. However, this derived formula was found to not match the blue spectral wavelengths and so cannot be used for atmospheric studies. Although a more workable model covering some or all chromaticities could be developed sometime in the future.

A more convenient method of linking hue angle and dominant wavelength is to develop look up tables based on established colour systems including the Munsell and the Swedish Natural Colour System 'wheels' (Hunt, 2006; Lillo et al. 2002; Malacara, 2002; Wyszecki and Stiles, 2000; Derefeldt and Hedin, 1989; Derefeldt et al. 1987).

Lillo et al. 2002 tabulated CIELUV derived hue angles and their corresponding dominant wavelengths using the Swedish Natural Colour System as a basis, which will serve as an approximation of dominant wavelengths in this study.

2.3.2.4 CIEDE2000 Colour Difference Formula

Despite the expectation that the CIE LAB colour space would be uniformly spaced, several inhomogeneities have been found particularly in the calculation and plotting of equal tolerance contours (Milward, 2009; Schanda, 2007; Witt, 2007; Melgosa et al. 2004; Melgosa, 2000).

The CIE and other groups sought to improve on the CIE LAB colour space with colour difference formulae developed by the CIE – CIE94 and CIEDE2000; the Colour Measurement Committee of the British Society of Dyers and Colourists – CMC and a German standard – DIN99 (Millward, 2009; Witt, 2007).

Although CIEDE2000 is computationally more demanding than the other colour difference formulae, it is considered more accurate and representative of perceived colour shifts (Millward, 2009; Witt, 2007; Sharma et al. 2005, Melgosa et al. 2004; Malacara, 2002). Additionally, this colour difference formula supersedes the other algorithms (Witt, 2007). The complexity is readily overcome by the use of Microsoft Excel or equivalent spreadsheet programs (Sharma et al. 2005).

The following is an account of the rationale needed for each of the CIEDE2000 corrections. The lengthy calculation is divided into 4 interdependent parts modified from Sharma et al. (2005).

All equations are from Witt (2007) and Sharma et al. (2005). Note, for each comparison, the subscript '*i*' refers to the number of the sample being compared (1 or 2). A description for the main iterations used in the calculation of the colour difference will also be discussed below.

Studies of the equal tolerance ellipsoids found that the *a** axis needed to be elongated to match those on the *b** axis ellipsoids to provide a better fit within the CIE LCh cylindrical colour space. Subsequently this requires a recalculation of the *L*,*C* and *h* values of the corresponding CIE LCH colour metric in step 1 below, (Witt, 2007; Sharma et al. 2005; Melgosa et al. 2004).

Step 1. Recalculating $L_i^{'}, C_i^{'}, h_i^{'}$:

The *a** axis of the CIELAB colour space needed to be extended, therefore:

$$a_i^{'} = a_i^{*}(1+G), \tag{29}$$

where *G* is dependent on the average chroma vector,

$$G = 0.5\left(1-\sqrt{\frac{\overline{C}_{AB}^{7}}{\overline{C}_{AB}^{7}+25^{7}}}\right), \tag{29a}$$

and

$$\overline{C}^{*}_{AB} = \frac{C^{*}_{1AB} + C^{*}_{2AB}}{2}. \tag{29b}$$

The chroma vectors in equation 29b are calculated in the same way as in equation 24 for each of the colour samples being compared. For consistency in notation for the b^* and luminance L^* (Witt, 2007),

$$b_i^{'} = b^{*}, \tag{30}$$

$$L_i^{'} = L^{*}. \tag{31}$$

Hence, to calculate the corrected chroma and hue angle, equations 32 and 33 are applied:

$$C_i^{'} = \sqrt{\left(a_i^{'}\right)^2 + \left(b_i^{'}\right)^2}, \tag{32}$$

$$h_i^{'} = \tan^{-1}\sqrt{\left(\frac{b_i^{'}}{a_i^{'}}\right)}. \tag{33}$$

Corrected hue angle will be used for comparison with those calculated directly from the CIE LAB colour space and gamma-invariant hue angles detailed in the next section.

Step 2. Calculating luminance, chroma and hue angle differences (denoted as $\Delta L^{'}, \Delta C^{'}, \Delta H^{'}$ respectively) requiring the recalculated luminance, chroma and hue angle vectors calculated in Step 1:

$$\Delta L^{'} = L_2^{'} - L_1^{'}, \tag{34}$$

$$\Delta C^{'} = C_2^{'} - C_1^{'}, \tag{35}$$

$$\Delta H^{'} = 2\sqrt{C_1^{'}C_2^{'}}\sin\left(\frac{\Delta h^{'}}{2}\right), \tag{36}$$

where

$$\Delta h^{'} = \begin{cases} 0 & C_1^{'}C_2^{'} = 0 \\ h_2^{'} - h_1^{'} & C_1^{'}C_2^{'} \neq 0;\ \left|h_2^{'} - h_1^{'}\right| \leq 180^{\circ} \\ (h_2^{'} - h_1^{'}) - 360^{\circ} & C_1^{'}C_2^{'} \neq 0;\ (h_2^{'} - h_1^{'}) > 180^{\circ} \\ (h_2^{'} - h_1^{'}) + 360^{\circ} & C_1^{'}C_2^{'} \neq 0; (h_2^{'} - h_1^{'}) < -180^{\circ} \end{cases}. \tag{37}$$

Step 3. Calculating luminance, chroma and hue angle averages between 2 colour samples (denoted as $\overline{L}', \overline{C}', \overline{h}'$ respectively) requiring the luminance, chroma and hue angle vector differences calculated in Step 2.

$$\overline{L}' = \frac{L_1' + L_2'}{2}, \tag{38}$$

$$\overline{C}' = \frac{C_1' + C_2'}{2}, \tag{39}$$

$$\overline{h}' = \begin{cases} \dfrac{h_1' + h_2'}{2} & C_1' C_2' \neq 0; \quad \left|h_1' - h_2'\right| \leq 180° \\ \dfrac{h_1' + h_2' + 360°}{2} & C_1' C_2' \neq 0; \quad \left|h_1' - h_2'\right| > 180°; \quad (h_1' + h_2') < 360° \\ \dfrac{h_1' + h_2' - 360°}{2} & C_1' C_2' \neq 0; \quad \left|h_1' - h_2'\right| > 180°; \quad (h_1' + h_2') \geq 360° \\ (h_1' + h_2') & C_1' C_2' = 0; \end{cases}. \tag{40}$$

Step 4. CIEDE2000 colour differences, requiring parameters calculated in Step 3.

The 'lightness weighting function' (S_L) was not included with the earlier CIE94 colour difference formula, but has been included in the CIEDE2000 due to testing that revealed many differences in this parameter (Witt, 2007),

$$S_L = 1 + \frac{0.015\left(\overline{L}' - 50\right)^2}{\sqrt{20 + \left(\overline{L}' - 50\right)^2}}. \tag{41}$$

The 'chroma weighting function' (S_C) is the same as the earlier CIE94 formulae. It is designed to reduce the effects of chroma differences as chroma increases (Witt, 2007),

$$S_C = 1 + 0.045\overline{C}'. \tag{42}$$

The 'hue weighting function' (S_H) is quite complex with the CIEDE2000 colour difference formula taking into account various small hue angle complexities (Witt, 2007: Melgosa et al. 2004),

$$S_H = 1 + 0.015\overline{C}'T, \tag{43}$$

where T is calculated using the averaged hue angle (from Step 3),

$$T = 1 - 0.17\cos\left(\overline{h}' - 30°\right) + 0.24\cos\left(2\overline{h}'\right) + 0.32\cos\left(3\overline{h}' + 6°\right) - 0.20\cos\left(4\overline{h}' - 63°\right) \tag{43a}$$

The final adjustment in the CIEDE2000 colour difference formula is a correction factor, R_T, (equation 44) made for the tolerance ellipses around the blue region ($h_{AB} \approx 270°$) not aligning with the CIELAB origin (Witt, 2007; Sharma et al. 2005). This is particularly pertinent to this study as much of the data is anticipated to be within this hue angle region.

$$R_T = -R_C \sin\left(2\Delta\theta\right), \tag{44}$$

where R_c is calculated using the averaged chroma.

$$R_C = 2\sqrt{\frac{\overline{C}'^7}{\overline{C}'^7 + 25^7}}, \tag{44a}$$

and the double angle is defined using hue angle averages:

$$\Delta\theta = 30\mathrm{e}^{\left[-\left(\frac{\overline{h}' - 275°}{25}\right)^2\right]}. \tag{44b}$$

Finally, the CIEDE2000 (ΔE_{00}) formula is

$$\Delta E_{00} = \sqrt{\left(\frac{\Delta L'}{k_L S_L}\right)^2 + \left(\frac{\Delta C'}{k_C S_C}\right)^2 + \left(\frac{\Delta H'}{k_H S_H}\right)^2 + R_T\left(\frac{\Delta C'}{k_C S_C}\right)\left(\frac{\Delta H'}{k_H S_H}\right)}, \tag{45}$$

where the parameters k_L, k_C and k_H are equal to 1 for most situations (Witt, 2007; Sharma et al. 2005; Melgosa et al. 2004).

2.3.2.5 Gamma-Invariant Hue Angle

Mathematically, it is easy to note that hue angle is gamma-invariant to lightness or brightness (L^*), calculated from the angle between the yellow-blue and red-green planes from the CIELAB and CIELUV, expressed in the respective CIELCh colour space (Kerr, 2010; Hunt, 2006; Malacara, 2002; Finlayson and Schaefer, 2001; Wyszecki and Stiles, 2000).

However, hue angle calculated using all colour spaces is subject to the approximated generalised gamma correction performed in equation 2, which can actually vary significantly with atmospheric optical conditions (Kerr, 2010; Hunt, 2006; Finlayson and Schaefer, 2001; IEC, 1999).

Finlayson and Schaefer (2001) developed a hue angle correlate (*H*) that is both gamma-invariant to brightness, lightness and gamma. Thus, this correlate is more 'stable', mirroring 'machine vision' or how the camera 'sees',

$$H = \tan^{-1} \frac{\log(R) - \log(G)}{\log(R) + \log(G) - 2\log(B)}, \tag{46}$$

where R, G and B are the red, green and blue signal from the camera sensor normalised to be out of 1. The gamma-invariant hue angle is analogous to CIELAB's h_{AB}, where 0°/360° represents red, 90° represents yellow; 180° represents green and 270° represents blue, (Lillo et al. 2002; Finlayson and Scahefer, 2001).

This correlate will be used to determine the general effects of gamma correction on hue angle. Also, it will provide a means to demonstrate the effectiveness of using the modifications made to the red-green axis of CIELAB (a^*) for use with the CIEDE2000 colour difference formula by comparing the gamma-invariant hue angle with average profiles (horizon to 20° elevation) of midday CIELAB derived h_{ab} (Equation 25) and CIEDE2000's parameter h' (Equation 33).

'Gamma-invariant chroma' can be determined in much a similar way as for C_{AB} and C_{UV} (Equation 24 and the substitution of u^* and v^* for a^* and b^* for the latter). From equation 46, the gamma-invariant chroma can be derived as:

$$C_{inv} = \sqrt{\left(\log(R) - \log(G)\right)^2 + \left(\log(R) + \log(G) - 2\log(B)\right)^2}. \tag{47}$$

2.4 Error Analysis

There are very few studies detailing or using error analysis in colorimetric aerosol studies. Natural aerosol variability, meteorological conditions, camera image noise and seasonality make it very difficult to determine the exact magnitude of uncertainties with data from long term studies, thus being a likely reason why no error bars are placed on many graphs from many of the previous studies. The same condition applies for this study. However, the variance-covariance analyses can be applied to average data, as has been applied in this study.

Studies related to calculating uncertainties of the parameters for each colour space have applied variance-covariance analyses (Gardner, 2007; Burns and Berns, 1997), using a general formula:

$$U_{\alpha\beta\gamma} = S^{T}{}_{\alpha\beta\gamma} U_{XYZ} S_{\alpha\beta\gamma}, \tag{48}$$

where $U_{\alpha\beta\gamma}$ is the uncertainty matrix of a colorimetric triplet being analysed, such as CIE xyY; $S_{\alpha\beta\gamma}$ and $S^{T}_{\alpha\beta\gamma}$ are the sensitivity matrix of the colorimetric triplet and its transpose; and U_{XYZ} is the variance-covariance matrix of the CIE XYZ tristimulus data.

Haralabidis and Pilinis (2008) quantified observer sensitivities to colour shifts due to urban aerosols as compared with the 'machine vision' from a digital camera. Both methods are considerably difficult and time consuming particularly if applied to each datum point from a large data set without specialised computing capabilities.

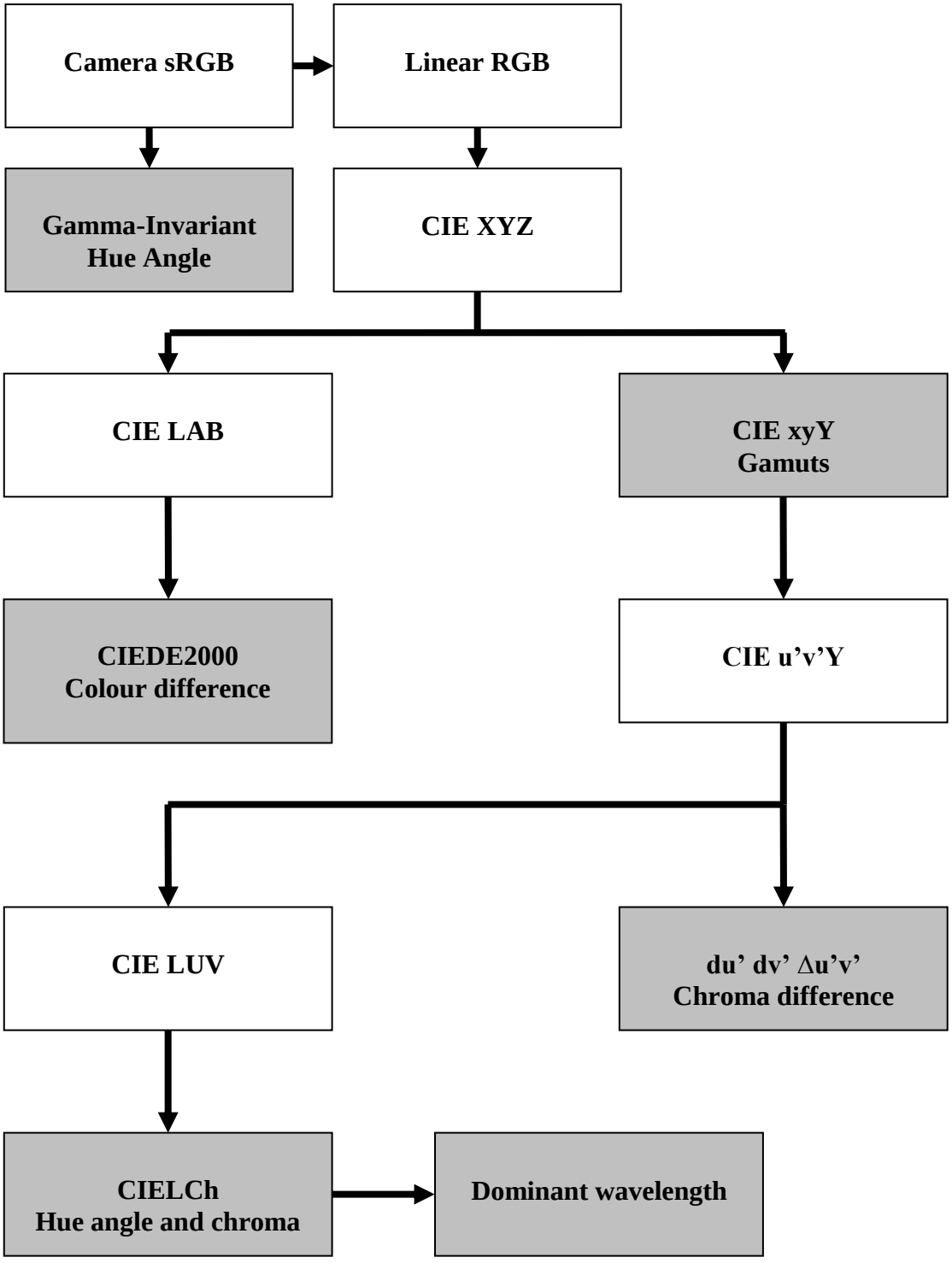

Figure 2.6: Methodology summary flowchart. Shaded boxes indicate an endpoint metric used in this analysis. All raw data is on the CD (Appendix B)

3. Results

3.1 Camera Noise Levels

Signal to noise ratio (SNR) is measured with respect to digital count. Increased digital count represents a tendency from black to white. The gradient of SNR with respect to digital count for hazy conditions is shallower than that of the control (Figure 3.1), indicating less noise reduction. This trend is indicative of a reduction of contrast and purity as compared to the IEC control environment described by Hyslop (2009) and MacAdam (1981). As a consequence, larger digital numbers indicate the lighter grays and white have increased noise. Conversely, the lower digital values demonstrate a slight increase in the signal.

However, further testing determined that average noise was less than 1% of the digital count for control and hazy conditions in the red, green, blue as well as luminance (Y) channels. This result vindicates Canon's advertised Digic IV noise reduction technology, proving the suitability of this camera. As the camera is used with the same settings throughout the experiments, any such error will be consistent, thus becoming a systematic error that can be corrected.

The corresponding mean noise error calculates to $\Delta u'v' = 0.00014$, with a corresponding standard deviation of 0.00037, comparable to that found in a similar study performed by Lee Jr. (2008) whose mean was higher at 0.00036 with a lower standard deviation of 0.00023. Kerr's (2008) and Hunt's (2006) estimated that $\Delta u'v' \approx 0.002$ is just visually discernable. The mean luminance L^* error is 1.27%, less than the 2% described by Hernandez-Andres (2003).

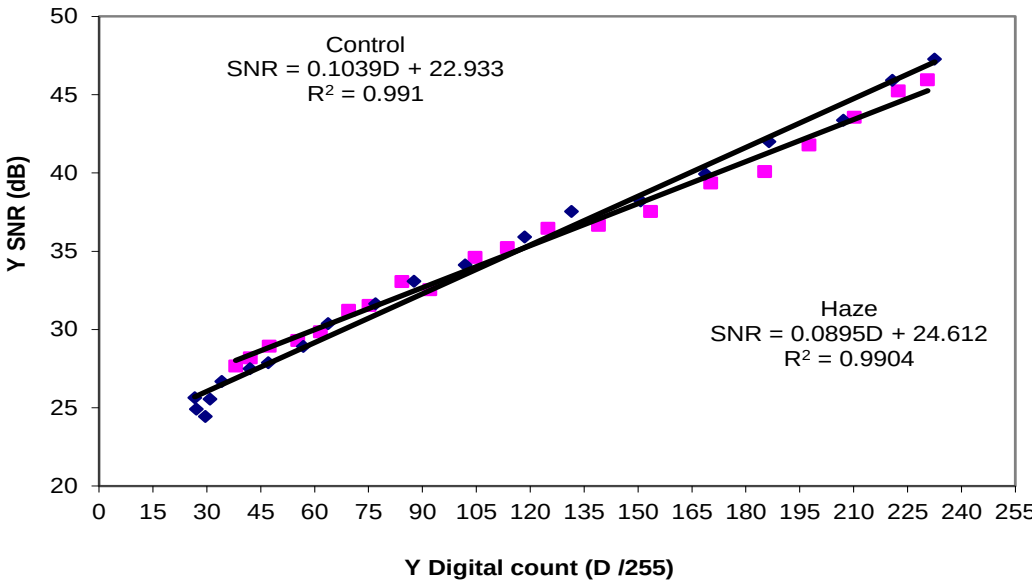

Figure 3.1: Plot of luminance (Y) channel digital number measured against luminance (Y) channel signal to noise ratio for an IEC control environment compared to hazy sky conditions. Red (haze) and blue (control).

The Y channel SNR is shown here as it is an average of RGB channels. All RGB channels were well within 1 standard deviation of the Y channel average in both control and hazy sky conditions.

3.2 Tokyo Skylight Gamut

Data taken from observations made in Tokyo during 2009 were plotted on a CIE xy chromaticity graph (Figure 3.2). A total of 2360 pixels were taken from the horizon to approximately 20° elevation. The pixels were selected from 118 sky photos taken at different times of the day (dawn, during the day and at dusk) in differing sky conditions (clear sky, polluted, cloudy and overcast). Time constraints prevented any more sky photos been taken.

The Tokyo sky data has a strong correlation coefficient of 0.9667 with the gamut derived from it. The quadratic equation of the gamut is,

$$y = -2.6676x^2 + 2.4326x - 0.1719. \quad (49)$$

The Tokyo skylight gamut is in good agreement with the CIE Daylight locus (Equation 8) and the gamut calculated for similar conditions at Granada, Spain during the late 1990's by Hernandez-Andres et al. (2001):

$$y = -2.7794x^2 + 2.7220x - 0.2477. \quad (50)$$

The gamut differences can be explained primarily by Tokyo having substantially more urban aerosols than Granada, and the artefact effect of white balance in the camera (Wuller and Gabele, 2007). The majority of the difference is highly likely to be the difference in aerosol composition and concentration. However, white balance is responsible for the 'flattening' of the gamut (Huynh and Robles-Kelly, 2007).

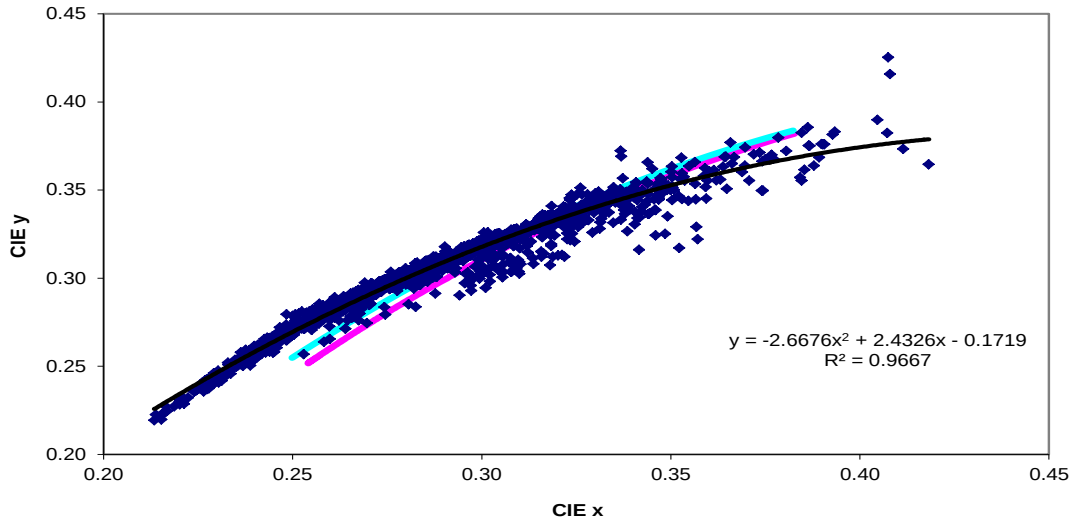

Figure 3.2: Tokyo sky chromaticities (blue dots) and gamut (black) compared to the CIE Daylight locus (blue) and the Planckian locus (pink) (n = 2360)

Most data points are on the green side of the Planckian and CIE Daylight loci, particularly for correlated colour temperatures (CCTs) larger than 6200K (increasing *x* trend), including the nearby D_{65} white point (6504K). Many points with CCTs less than 6200K tend to purple, below the established loci. This is associated with greater aerosol scattering. This effect was in fact observed in studies in India during the late 1960's to mid 1970's (Hernandez-Andres et al. 2001; Sastri, 1976) and indicative of what occurs at twilight (Lee Jr. and Hernandez-Andres, 2003; Lee Jr. 1994).

The two time categories (midday and dawn/dusk) will be examined separately in the next sections.

3.2.1 Midday skylight gamut

The Tokyo midday gamut (Figure 3.3) is from data collected through different times of the year, in different conditions when the sun was close to or at solar maximum with a relative air mass less than 2. The data was taken from pixels from the horizon up to approximately 20° elevation from each sky photo.

The equation of the Tokyo midday gamut is significantly steeper than the Granada and CIE Daylight loci (equations 50 and 8 respectively).

$$y = -4.782x^2 + 3.5978x - 0.3300\,, \qquad (51)$$

All midday data were predominantly on the green side of the Planckian locus. Increased aerosol loading results in a trend towards the achromatic centre, along the CIE Daylight locus. These observations are consistent with observations made by Hernandez-Andres et al. (2001) with colorimetric trends in Granada, Spain and earlier observations from urban centres in India, made by Sastri (1976).

The presence of above average concentrations of NO_2 and SPM vectors the data towards the achromatic centre and the CIE Daylight locus. There are a few pixels taken from the horizon on a day with above average concentrations of NO_2 and SPM that result in the chromaticity being in between the CIE Daylight locus and the Planckian locus.

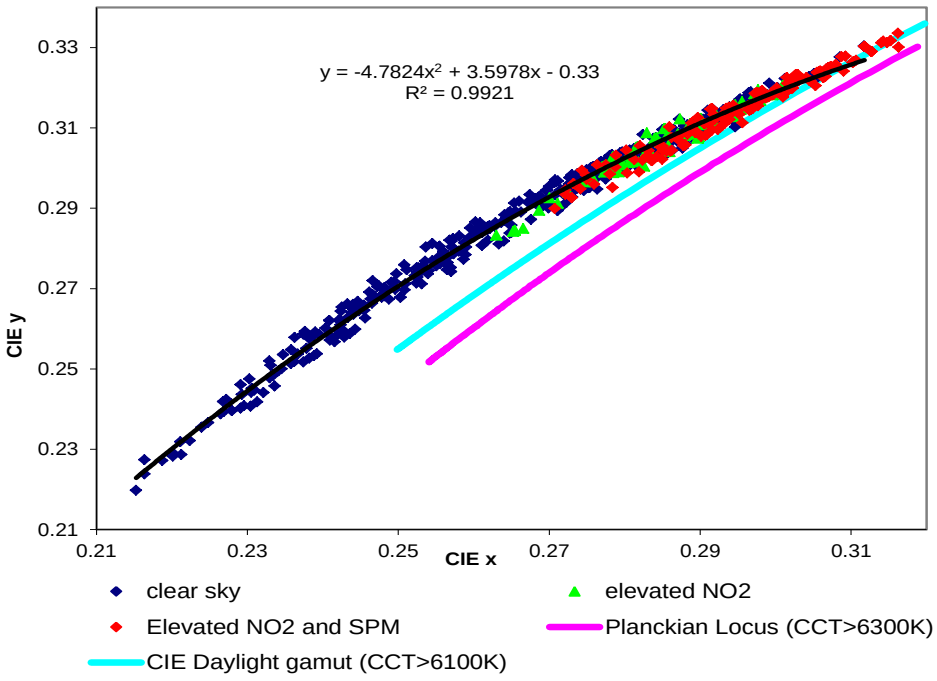

Figure 3.3: Tokyo midday sky chromaticities and gamut compared to the CIE Daylight locus and Planckian locus divided into air quality conditions (n=680)

The midday data has a correlation coefficient of 0.9921, suggesting very little variation due to atmospheric turbidity from increased aerosol loading. The reason for these observations is that at midday, there is much less air mass to cause backscattering of blue wavelengths; these in turn 'flood' any sky picture.

3.2.2 Dawn-dusk skylight gamut

The Tokyo dawn-dusk gamut (Figure 3.4) is from data collected through different times of the year, in different conditions when the sun was close to or below the horizon, with a relative air mass greater than 5.5. The data was taken from pixels from the horizon up to approximately 20° elevation from each sky photo. All pictures were taken with care not to put the camera in direct line with the sun so as to not damage the CCD sensor.

The calculated gamut is only slightly steeper than that of the CIE daylight and Granada data, but is shallower and covers a greater range than the data collected in the midday sample,

$$y = -3.3608x^2 + 2.8712x - 0.2419 \quad (52)$$

The dawn-dusk results have a correlation coefficient of 0.9157. While dawn-dusk data is still in good agreement with the gamut, the correlation is lower than that observed at midday, demonstrating the effect of increased atmospheric turbidity. A significant proportion of the data is either in between the CIE Daylight locus and Planckian locus or in the purple trending area below the locus. There are very little differences between a clear and polluted sky, although most above average NO_2 concentrations lie in the purple trending region.

Dawn-dusk pixel chromaticities account for all of the purple trending data collected in Tokyo. The trends are consistent with observations by Lee Jr. and Hernandez-Andres, (2003) and Sastri (1976). However, separating clear sky from polluted sky is impractical.

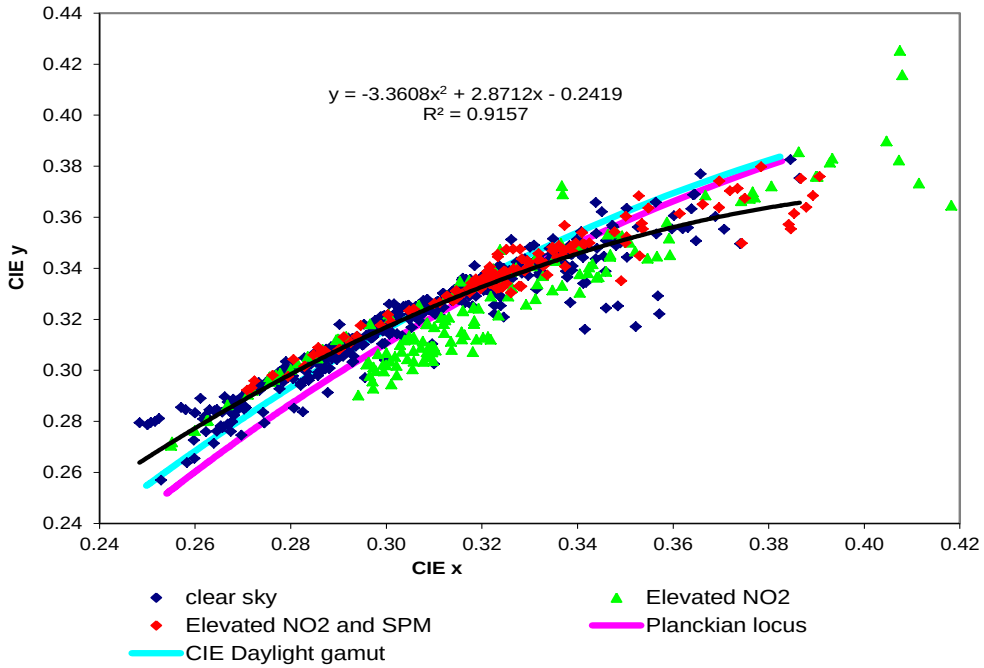

Figure 3.4: Tokyo dawn/dusk sky chromaticities and gamut compared to the CIE Daylight locus and Planckian locus divided into air quality conditions (n=800)

3.3 Colorimetric metrics

3.3.1 Chromatic difference CIE u'v'Y (1976)

Data derived for this colour metric were separated according to the elevation divisions described by Sloane (1988), namely 'horizon' at approximately 1.5° and 'elevated' at approximately 20°. The metrics for chromatic differences (Kerr, 2008), were taken with reference to a model clear blue sky with a CCT of 15,000K. Positive values for du' and dv' indicate an increase in yellowing and reddening respectively. Negative values refer to blue and green trends respectively.

Overall, all Tokyo sky data were considerably more perceptibly red (+du') than the reference blue sky (CCT = 15000K), however some of the data were a 'stronger' blue (-dv') than the reference sample. The yellow-blue (dv') coordinates had 57% more variation than du' indicating a higher variation with yellowing with respect to the reference blue sky model. The minimum chromatic difference to the model clear sky is at a perceptible $\Delta u'v' = 0.0153$.

3.3.1.1 Midday Chromatic Difference

Figure 3.5 shows the average CIE u'v'Y colour differences from the horizon to 20° elevation. All 3 sky conditions clearly show a gradation to higher purity blue from the horizon to the 20° elevation and were perceptibly more 'red' than the model blue sky chromaticity, due to the fact that while nitrogen dioxide and SPM concentrations were below average, they were still present in small amounts, causing some noticeable absorption and scattering effects.

Clear sky chromaticities exhibit the greatest change from the horizon to 20° elevation, with a very perceptible change of $\Delta u'v' = 0.0178$. The colour shift is due to the blue becoming richer ($\Delta dv' = -0.0359$) compared to the increased 'greening' ($\Delta du' = -0.0146$). The characteristic deepening blue is due to the lessening atmospheric path length at greater elevations resulting in the clear sky being dominated by multiple Rayleigh scattering by molecular oxygen and nitrogen (Hyslop, 2009; Haber et al. 2005; Jacobson, 2002; Sloane, 1988).

Above average nitrogen dioxide chromaticities exhibit perceptibly less change from the horizon than that of clear sky. However, the change is still perceptible with $\Delta u'v' = 0.0158$. Despite there once again being more of a shift towards blue ($\Delta dv' = -0.0150$) than green ($\Delta du' = -0.0085$), these changes are considerably less than clear sky. This phenomenon is referred to as 'yellow and red shifting' due to the preferential absorption by nitrogen dioxide of blue wavelengths by authors including Dogras et al. (2004), Sloane (1988) and Husar and White (1976).

Nitrogen dioxide pollution with the presence of above average SPM concentrations has a chromaticity change that is very similar to that without it, $\Delta u'v' = 0.0152$. Specific trends in the yellow-blue ($\Delta dv' = -0.0143$) and red-green ($\Delta du' = -0.0077$) axes are also similar. Chromaticities of the horizon pixels are the closest to the achromatic D_{65} white point of the 3 sky conditions, due to the whitening effect of Mie scattering from SPM aerosol particles (Hyslop, 2009; Haber et al. 2005; Jacobson, 2002; Preetham et al. 1999).

The greatest chromatic differences are when above average nitrogen dioxide with and without SPM concentrations are compared to clear sky. Despite the decrease in yellowing and reddening from the horizon in the polluted skies, the difference in 'blueness' and 'greenness' to that of clear sky become more apparent with higher elevation, as can be seen in Figure 3.5. Increased nitrogen dioxide discoloration with greater zenith angle was noted in sky chromaticity studies performed in the late 1960's to mid 1970's in Los Angeles and New Delhi (Husar and White, 1976; Sastri, 1976).

At the horizon, above average nitrogen dioxide chromaticities are not all that discernible from clear sky horizons ($dv' = 0.0038$). With the presence of above average SPM levels, nitrogen dioxide discoloration is more pronounced ($du' = 0.0096$). However, at 20° elevation, chromatic differences increase to clearly perceivable amounts, $dv' = 0.0247$ and 0.0314 respectively. Though less pronounced, red-green shifts followed a similar pattern, from the horizon to 20° elevation, above average nitrogen dioxide $du' = 0.0025 \rightarrow 0.0086$, with increased SPM $du' = 0.0061 \rightarrow 0.0130$.

Figure 3.5 also very clearly shows the light extinction by preferential absorption of blue light by nitrogen dioxide in attenuating the 'blueness' with increasing elevation. (Hyslop, 2009; Dogras et al. 2003; Jacobson, 2002; Horvath, 1993; Davidson et al. 1988; Sloane, 1988; Husar and White, 1976; Sastri, 1976).

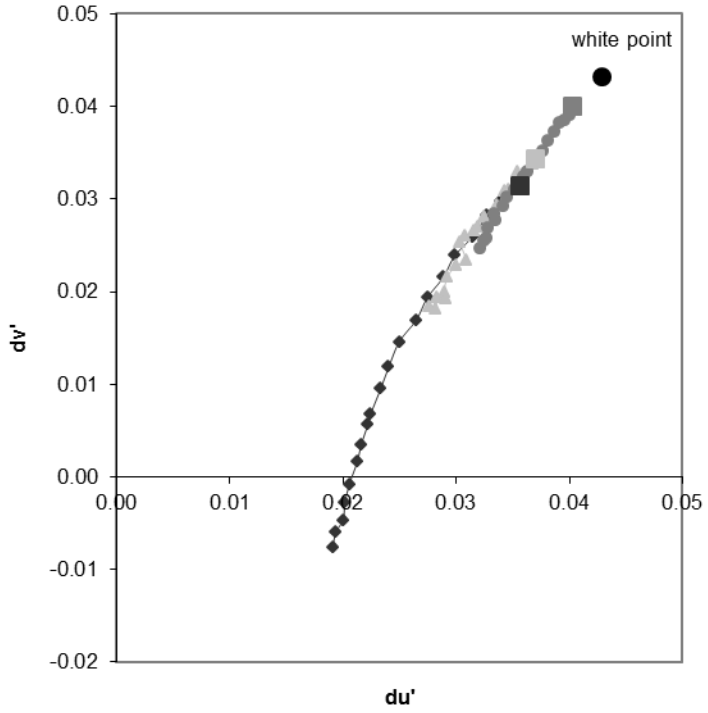

Figure 3.5: CIE u'v'Y colour differences for average midday horizon to 20° elevation respectively, with respect to a 15,000K CCT clear blue sky model by Wyszecki and Stiles, 2000. Each step is in 1° increments from 1° above the horizon (indicated by the box on each line). Dark grey diamonds are clear sky, light grey triangles are above average NO_2 and mid-grey circles are above average NO_2 and SPM. The D_{65} white point is labelled.

The *du'* axis is deliberately placed in the path of the data in figure 3.5 to show that even on the clearest day, the Tokyo sky still exhibits a perceptible red shift from the model 15,000 K blue sky from Wyszecki and Stiles, (2000).

Chromaticities for all 3 conditions demonstrated no 'hooks' or changes of direction described in a similar study performed by Lee Jr. (1994). However, as shown in Figure 3.6, there is a prominent 'hook' visible when the average relative luminance is plotted against elevation angle. Clear sky profiles have a prominent hook occurring with a maximum relative luminance between 4°-6° elevation, similar to the one Lee Jr. (1994) noted for Chesapeake Bay.

The relative luminance profiles for above average nitrogen dioxide with and without elevated SPM concentrations run roughly parallel. Both conditions possess less prominent relative luminance hooks also at about 4°-6° (Figure 3.6).

Figure 3.6: Average relative luminance (L*) profiles for midday clear sky (dark grey), above average NO_2 (light grey) and above average NO_2 and SPM (mid grey).

3.3.1.2 Dawn-Dusk Chromatic Difference

Figure 3.7 shows the average CIE u'v'Y colour differences for the horizon to 20° elevation for data collected during dawn and dusk. The 3 sky conditions demonstrate similar overlap and incoherence as the dawn-dusk gamut in Figure 3.4 but in this metric, exhibiting a hook that becomes more prominent as the amount of pollutants present increases.

All data was far more red (+*du'*) and yellow (+*dv'*) than the references blue sky model and in most cases the D_{65} white point. The greater light path at dawn and dusk, with relative air mass greater than 5.5, results in the blue being almost completely scattered away from the observer (Haber et al. 2005; Jacobson, 2002; Preetham et al. 1999).

Above average nitrogen dioxide concentrations underwent the greatest shifts towards the reference blue sky chromaticity coordinates as elevation increased, $\Delta du'v' = 0.0282$, including a very strong shift towards blue ($\Delta dv' = -0.0259$) and a strong shift towards green ($\Delta du' = -0.0158$). The overall shift from all 3 conditions were very similar, save for blue-shift, where clear sky and the presence of above average SPM concentrations had a significantly less shift ($\Delta du' = -0.0201$ and $\Delta du' = -0.0162$ respectively).

This phenomenon suggests that the optical effects of Mie scattering of SPM within the nitrogen dioxide aerosol layer become more important as elevation increases, as modelled by Sloane (1988).

Despite the overall blue-shifting with increasing elevation, the presence of above average SPM with nitrogen dioxide haze causes the sky chromaticity to become relatively yellower. Without SPM, the sky colour was only just perceptibly more yellow than clear sky. These observations further suggest that Mie scattering due to SPM plays an important role with increasing elevation (Haber et al. 2005; Jacobson, 2002; Preetham et al. 1999). The average difference in red-shift from clear sky remained relatively constant irrespective of the presence of above average SPM concentrations.

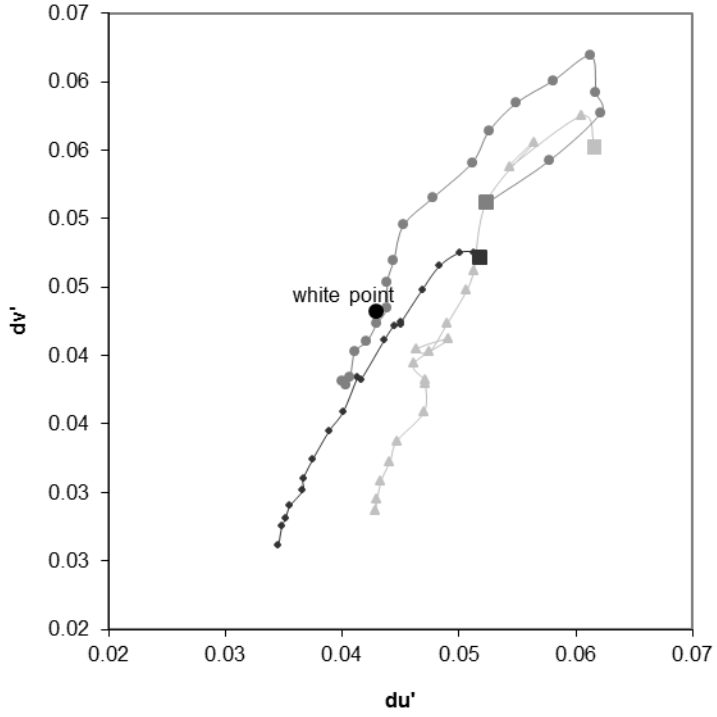

Figure 3.7: CIE u'v'Y colour differences for average dawn-dusk horizon to 20° elevation respectively, with respect to a 15,000K CCT clear blue sky model by Wyszecki and Stiles, 2000. Each step is in 1° increments from 1° above the horizon (indicated by the box on each line). Dark grey are clear sky, light grey are above average NO_2 and mid grey is above average NO_2 and SPM. The D_{65} white point is labelled.

The hook described by Lee Jr. (1994) is very clearly evident in dawn-dusk chromaticities (Figure 3.7). The shift occurs at approximately 2° for clear sky and more pronounced for skies with above average nitrogen dioxide, consistent with much of the data recorded by Lee Jr. (1994) for places such as Antarctica and Bald Eagle, USA. However, the presence of SPM results in a hook further up at 3°-5°, approaching those of the luminance changes recorded at midday.

Luminance hooks (Figure 3.8) were not as consistent as those recorded by Lee Jr (1994). Above average nitrogen dioxide with SPM has a prominent relative luminance hook at approximately 11°-12°, more than twice the elevation than where the chromaticity hook occurred.

Above average nitrogen dioxide concentrations had minor relative luminance hooks at approximately 4° and 13° and a major one at 10°. The luminance profile of above average nitrogen dioxide is also unique compared to the other conditions in that it has perceptibly less relative luminance than clear sky.

The clear sky hook is far less pronounced occurring at approximately 9° elevation, after which, the luminance remained relatively constant, until a minor hook occurs at approximately 18°.

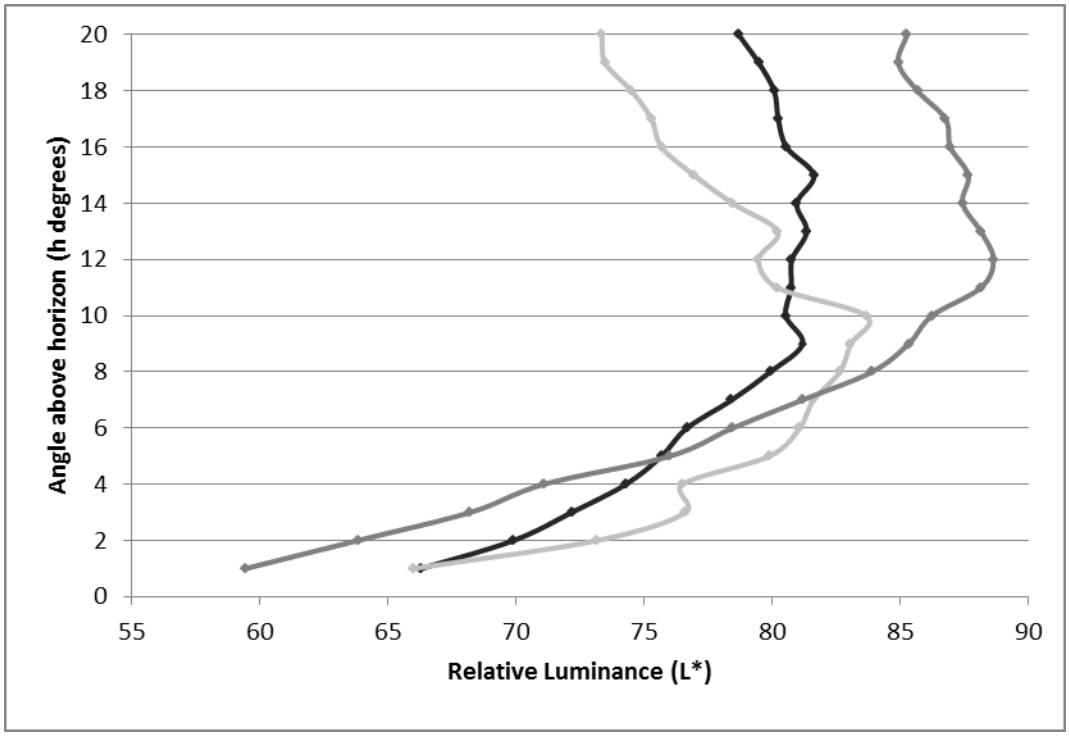

Figure 3.8: Average relative luminance (L*) profiles for dawn-dusk clear sky (dark grey), above average NO_2 (light grey) and above average NO_2 and SPM (mid grey).

3.3.2 CIELCH$_{UV}$ colour space

Table 3.1 is a summary of the average values for the relative luminance (L^*), chroma (C_{uv}), hue angle (h_{uv}) with the associated dominant wavelength (λ_d) (adapted from data tabulated in Lillo et al. 2002, 2004) for all 3 conditions (clear sky, above average NO_2 and above average NO_2 and SPM), positions (horizon and 20° elevation) and times (midday and dawn-dusk).

Table 3.1: Categorised average CIELCH values for the whole data set.

Conditions		L*	C_{uv}	h_{uv}°	λ_d (nm)
Overall average	Midday clear sky	**68.5**	**30.5**	**238.3**	**481**
	Midday above average NO_2	**80.0**	**21.1**	**236.5**	**482**
	Midday above average NO_2 and SPM	**81.8**	**13.6**	**228.2**	**484**
	Dawn dusk clear sky	**78.0**	**13.6**	**178.4**	**496**
	Dawn dusk above average NO_2	**77.6**	**17.4**	**182.6**	**495**
	Dawn dusk above average NO_2 and SPM	**81.2**	**15.5**	**95.2**	**567**
Horizon average	Midday clear sky	**70.9**	**14.5**	**232.5**	**483**
	Midday above average NO_2	**78.0**	**11.6**	**235.9**	**482**
	Midday above average NO_2 and SPM	**79.3**	**5.8**	**193.3**	**494**
	Dawn dusk clear sky	**69.5**	**16.6**	**149.8**	**521**
	Dawn dusk above average NO_2	**71.9**	**23.2**	**101.2**	**567**
	Dawn dusk above average NO_2 and SPM	**63.8**	**16.2**	**53.3**	**578**
20° elevated average	Midday clear sky	**63.8**	**42.5**	**243.4**	**478**
	Midday above average NO_2	**80.2**	**29.7**	**238.5**	**481**
	Midday above average NO_2 and SPM	**82.0**	**22.0**	**239.2**	**481**
	Dawn dusk clear sky	**79.4**	**16.4**	**237.7**	**482**
	Dawn dusk above average NO_2	**73.8**	**19.7**	**234.9**	**483**
	Dawn dusk above average NO_2 and SPM	**85.3**	**8.5**	**152.5**	**515**

Generally, with near constant dominant wavelength, as chroma increases, luminance decreases. This particularly is apparent for midday horizon and elevated positions. However, when considering all data between the horizon and 20° elevation, there is actually very little correlation between chroma and luminance for the Tokyo sky.

Table 3.2 is a summary of comparative values for the CIELUV coordinates u^* and v^*, chroma (C_{uv}) for the calculation of hue angle difference (ΔH) in accordance with equation 26, for all 3 conditions (clear sky, above average NO_2 and above average NO_2 and SPM), positions (horizon and 20° elevation) and times (midday and dawn-dusk).

All values are in relative units. The colour coding gives an indication of the colour trends that the values represent. Positive Δu^* represents yellow shifting; positive Δv^* represents red shifting; negative values represent blue and green respectively (Dogras et al. 2004; Sloane, 1988) and positive ΔC_{uv} represents increased richness in colour (= more saturated).

Table 3.2: Average hue angle CIELUV, chroma and hue angle differences. The colours for each cell represent the colour trend for that average.

Condition		Δu^*	Δv^*	ΔC	ΔH
Overall average	Midday clear sky to above average NO_2	3.5613	8.7872	-9.4195	1.0819
	Midday clear sky to above average NO_2 and SPM	7.8076	15.2338	-16.9630	2.2982
	Midday above average NO_2 to NO_2 and SPM	4.2462	6.4466	-7.5435	1.6384
	Dawn-dusk clear sky to above average NO_2	6.5572	3.6483	3.7700	6.4880
	Dawn-dusk clear sky to above average NO_2 and SPM	7.4177	12.0406	1.8708	14.0178
	Dawn-dusk above average NO_2 to NO_2 and SPM	0.8605	8.3923	-1.8992	8.2198
Horizon average	Midday clear sky to above average NO_2	1.5310	2.3914	-2.8933	0.5554
	Midday clear sky to above average NO_2 and SPM	5.0534	8.1711	-8.6715	4.1363
	Midday above average NO_2 to NO_2 and SPM	3.5224	5.7797	-5.7782	3.5249
	Dawn-dusk clear sky to above average NO_2	7.6407	8.6980	0.8215	11.5482
	Dawn-dusk clear sky to above average NO_2 and SPM	5.1077	5.5575	-0.3939	7.5379
	Dawn-dusk above average NO_2 to NO_2 and SPM	-2.5330	-3.1405	-6.9660	5.6785
20° elevated average	Midday clear sky to above average NO_2	3.1973	12.8285	-12.8519	3.1021
	Midday clear sky to above average NO_2 and SPM	7.4686	19.1643	-20.4779	1.9250
	Midday above average NO_2 to NO_2 and SPM	4.2714	6.3358	-7.6261	0.4794
	Dawn-dusk clear sky to above average NO_2	6.3496	0.4634	3.3999	5.3827
	Dawn-dusk clear sky to above average NO_2 and SPM	5.3255	10.4369	-7.8376	8.7098
	Dawn-dusk above average NO_2 to NO_2 and SPM	-1.0241	9.9735	-11.2374	5.0755

Several trends in the data can be observed from Table 3.2:

- There is no strong correlation between chroma and hue angle differences, suggesting that colour purity and dominant wavelength are independent metrics, as far as digital camera detection is concerned.
- Midday comparisons between clear and polluted skies exhibit discernable yellow and red shifts. The result of the red-yellow shifting is a marked desaturation (negative chroma) of the clear sky blue. Hue angle differences are mostly negligible.
- Horizon and elevated level chroma shifts are similar whether or not above average SPM concentrations are included with NO_2 haze.
- Above average NO_2 concentrations at dawn/dusk result in an increase in chroma (purity) associated with a significant hue angle shift, increasing towards the horizon.
- The addition of SPM with above average NO_2 at dawn/dusk resulted in a slight blue shifting from an already yellow-red shifted sky colour.

3.3.2.1 Midday data

A striking feature in tables 3.1 and 3.2 of the colour of the midday sky is that whether it is classified as 'clear sky' (refer to introduction) or otherwise, near the horizon or at 20° elevation, all dominant wavelengths are very close, between 478-494 nm. This range is in the blue, bordering on the green (cyan) part of the visible spectrum, particularly near the horizon (Hunt, 2006; Malacara, 2002). A consequence of the narrow range of dominant wavelengths is that despite polluted skies sometimes appearing pale yellow, the measured chromaticity is blue. However, there is a clear reduction in chroma or purity with increased pollution levels that is not completely offset by the increase in relative luminance. The ratio of the chroma and relative luminance results in less colour saturation/purity.

Figures 3.9a and 3.9b are specific examples of the perceived hue angle shift that occurs as a result of pollution. Figure 3.9a was taken during a heavily polluted day with above average concentrations of NO_2 and SPM, whereas Figure 3.9b is an example of what is classified as clear sky, having significantly below average concentrations of pollutants.

Both images were taken at the same time of the day 12 days apart so there were minimal sun zenith angle (SZA) and azimuth differences. The luminances (L*) are also very similar, averaging 78 and 73 for profile in figures 3.9a and 3.9b respectively. However, Figure 3.9a's chroma is much less than in Figure 3.9b, and thus is significantly desaturated in comparison. Pixels for analysis were taken from the centre of the picture, so as to minimise the effect of vignetting and associated chromatic aberration.

Figure 3.9a: Image taken in Tokyo, Japan facing due south at 12:00 JST 18th March, 2009 (SZA 53.3°, sun azimuth 184°).

Figure 3.9b: Image taken in Tokyo, Japan facing due south at 12:00 JST 30th March, 2009 (SZA 57.9°, sun azimuth 187°).

The horizon of Figure 3.9a has a slight perceivable yellow tinge, which also casts a 'yellowing' on the objects in the foreground. Also apparent, is the loss of contrast, particularly with the buildings in the background, this is symptomatic of the increase in relative luminance.

Despite the visual difference between Figures 3.9a and 3.9b, the hue angle is on a line pointing towards approximately 240° in Figure 3.10, very close to the hue angles defined as blue (Hunt, 2006; Lillo et al. 2002). Whilst pixels from the horizon of Figure 3.9a are on the same line, they appear to be very desaturated yellow. Patterns for both data sets are almost identical, including the noticeable hook that is present in both sets of data.

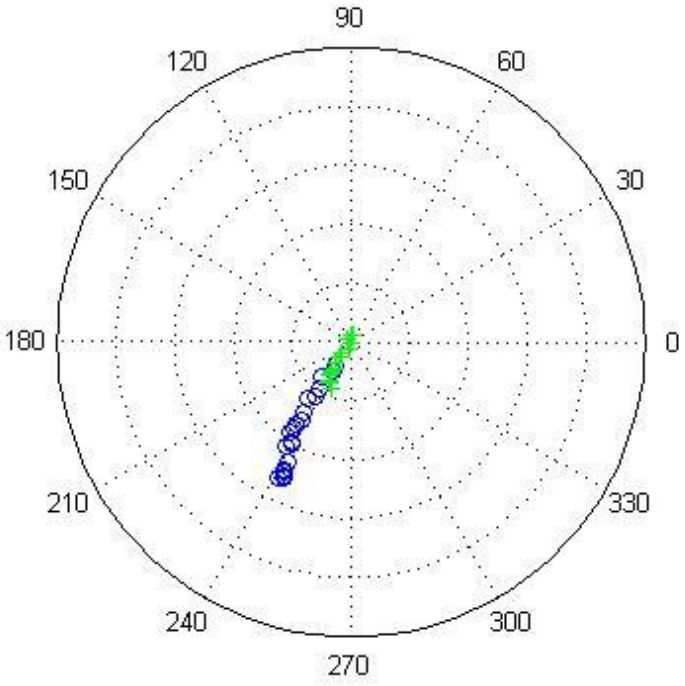

Figure 3.10: Hue angle-saturation (purity) polar coordinates comparing images in Figure 3.9a (+) and 3.9b (O). Saturation values increase by 0.2 unit intervals.

Compared to clear sky, the presence of above average NO_2 concentrations result in a clear yellow-red shift and lessening chroma, hence desaturation towards achromicity, increasing from the horizon to 20° elevation (Table 3.2). Dominant wavelengths remain very similar, with the addition of NO_2 resulting in less of a transition to a deeper blue than for clear sky (refer to Table 3.1).

Figure 3.11a shows the saturation, at 0.2 unit intervals (from 0, truncated at 0.6 for clarity) and hue angles for all midday clear sky and above average NO_2 data. It is very clear that the addition of NO_2 affects the chroma, hence saturation, rather than the hue angle to any great extent.

At the horizon, the difference in saturation and average hue angle is at a minimum for clear sky and above average NO_2. The slight change in perceived hue angle is also observed. Figure 3.11b charts the midday horizon saturation and hue angle plot. What is very clear is that any perceived colour difference is not due to any appreciable hue angle shift, but desaturation. The exception is at the horizon, where the hue angle has shifted to be heavily desaturated yellow, resulting in some colour cancellation causing perceived 'whitening'.

At 20° elevation, a similar pattern to that at the horizon occurs. Skies with above average NO_2 concentrations result in the same hue angle, but less colour saturation, (Figure 3.11c). There is noticeable less variation in hue angle in the 20° elevated sample than the horizon.

a.

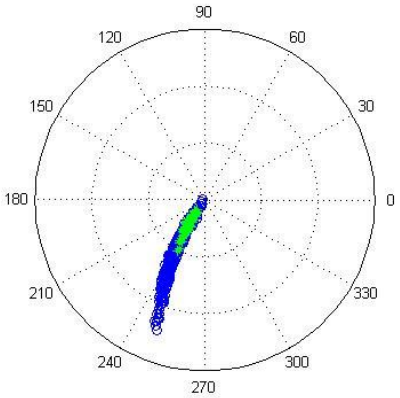

b.

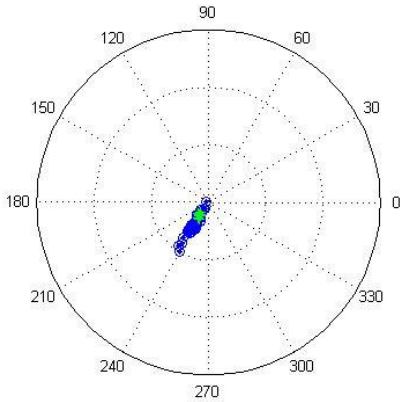

c.

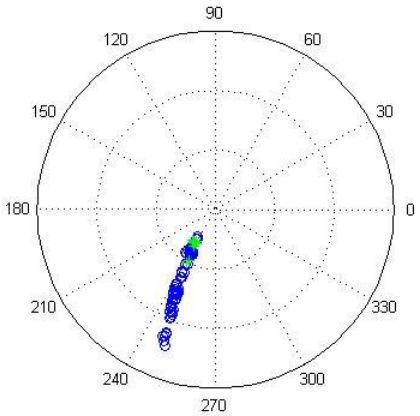

Figure 3.11: Saturation and hue angle polar plots, comparing midday clear sky (O) and above average NO_2 data (+). Image a is the overall comparison, b is for the horizon and c is for 20° elevation. Saturation increases by 0.2 unit intervals, truncated at 0.6 for clarity.

With the presence of above average SPM concentrations, greater desaturation occurs whilst still keeping with similar overall hue angle as can be seen by comparing figures 3.9a and 3.9b in figure 3.10. With increasing elevation angle there is an increased yellow shift as without above average SPM concentrations, however, there is far less red shift (refer to table 3.2). Also, there is a less prominent achromatic shift with increased viewing elevation angle. The greatest change in dominant wavelength is with the addition of above average SPM in the midday dataset.

Figure 3.12a shows the saturation, at 0.2 unit intervals (from 0, truncated at 0.6 for clarity) and hue angles for all midday clear sky and above average NO_2 with SPM data. Similar patterns to figures 3.10 and 3.11a are apparent, both datasets appear to vector towards the same dominant wavelength.

Despite the average hue angle differing by a substantial amount resulting in an average dominant wavelength up to 12 nm higher than other midday data (refer to table 3.1), the low saturation means that this difference is not clearly seen in figure 3.12b. Pixels from the bottom most horizon have hue angles that are very desaturated yellow and chroma values close to full achromicity. Much of the 'whitening' of the sky visible in figure 3.9a is due to blue-yellow colour cancellation.

Figure 3.12c shows a comparison between saturation, at 0.2 unit intervals, and hue angle for above average NO_2 with SPM and clear sky. Like NO_2 haze without SPM, there is less variance than that at the horizon and data is constrained in a small saturation range. But, it is clearly seen that any perceived hue angle shift is due to desaturation more than the negligible hue angle shift of 3 nm (refer to table 3.1).

a.

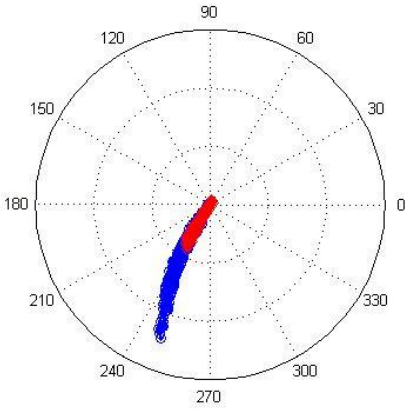

b.

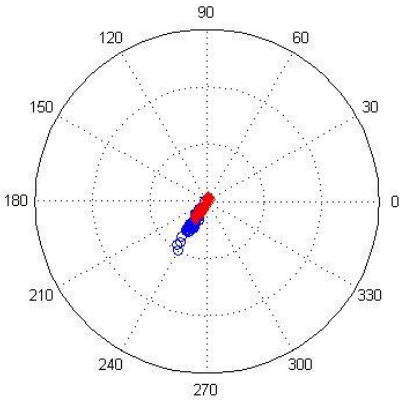

c.

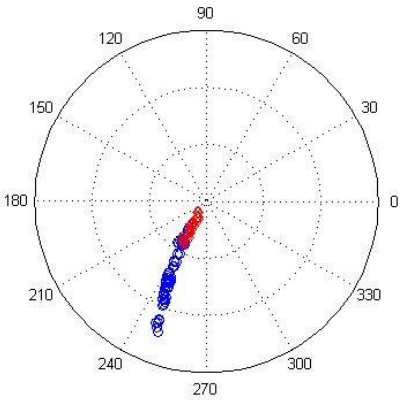

Figure 3.12: Saturation and hue angle polar plots, comparing midday clear sky (O) and above average NO_2 and SPM data (◇). Image a is the overall comparison, b is for the horizon and c is for 20° elevation. Saturation increases by 0.2 unit intervals, truncated at 0.6 for clarity.

The effects of above average SPM with the midday NO_2 haze can be seen in figures 3.13a and 3.13b. Primarily, they share a similar dominant wavelength, but SPM result in this becoming desaturated significantly, particularly at the horizon. In figure 3.13a it can be seen that much of the horizon data trends to heavily desaturated yellow, thus affecting the average dominant wavelength as in table 3.1.

The polar plots in figures 3.13a and 3.13b diagrammatically show that the presence of above average NO_2 without significant SPM results in a greater hue angle difference, associated with a greater proportional yellow-shift as measurements are taken upwards from the horizon as seen in table 3.2. The hue angle difference decreases in the presence of excess SPM. Both polar plots are at 0.2 unit intervals, truncated at 0.6 for clarity.

a.

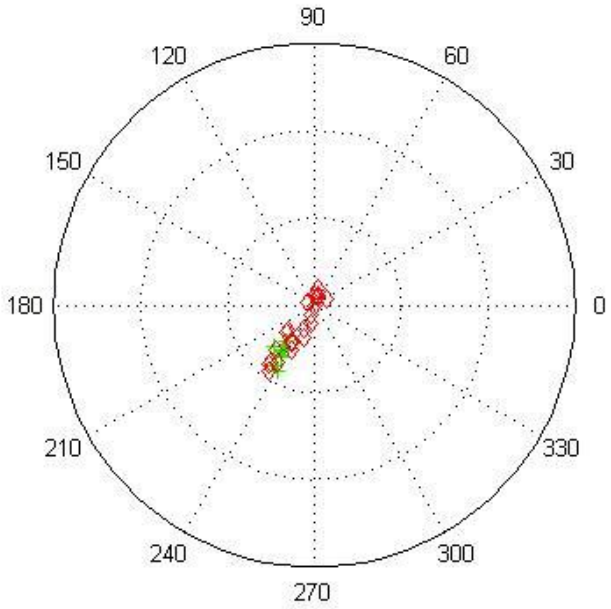

b.

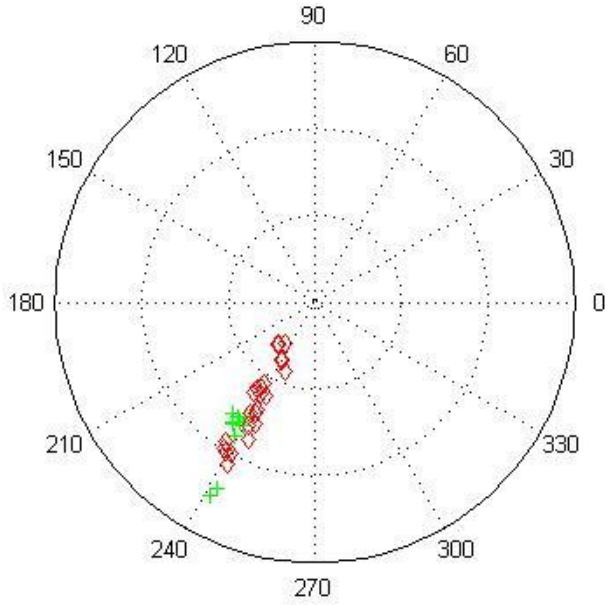

Figure 3.13: Saturation and hue angle polar plots, comparing midday NO_2 (+) and above average NO_2 and SPM data (◇). Image a is for the horizon and b is for 20° elevation. Saturation increases by 0.2 unit intervals, truncated at 0.6 for clarity.

3.3.2.2 Dawn-dusk data

Variability is greater in the data during dawn and dusk. The average dominant wavelengths are approximately bimodal, with much of the data mainly in the blue region, with dominant wavelengths of similar to what were observed for midday 482-496 nm and yellows and near yellows of 515-578 nm (refer to table 3.1).

With respect to clear sky, above average pollution generally, for midday, causes a yellow-red shift and changes to chroma, and hence saturation/purity. However, the addition of SPM concentrations results in changes to the colorimetric behaviour. Figures 3.14a, b and c show the bimodality of dawn-dusk saturation and hue angle particularly for clear sky.

The addition of above average SPM concentrations results in the average dominant wavelength for the polluted sky to shift to approximately 567 nm, which as can be seen in figure 3.14b is in a position in a general opposite direction to that of the clear sky average of 496 nm. Overall, there is a slight positive chroma shift (table 3.2), however, this is not recorded for the horizon nor at 20° elevation, thus most likely occurs in between the two extreme measurements.

It is very difficult to differentiate the sky conditions during these times as can be observed in figures 3.14a, b and c. The greater uncertainty is due to scattering and greater relative air mass. Thus, using polar CIELCH$_{UV}$ data is unsuitable. The scale for figures 3.14a, b and c is 0.1 unit intervals, truncated at 0.5 for clarity.

a

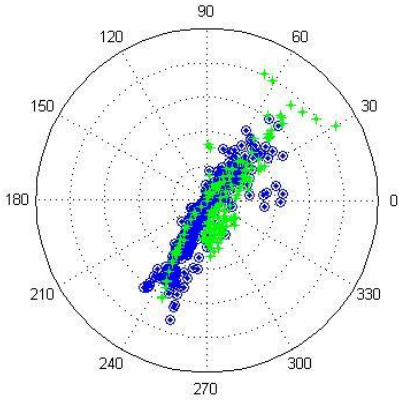

b

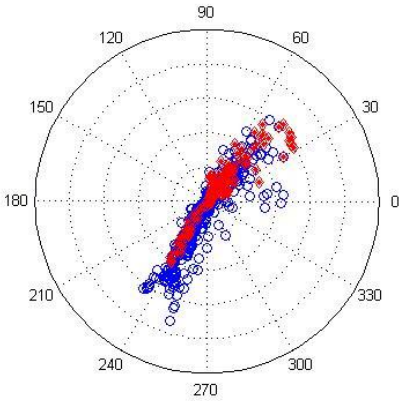

c

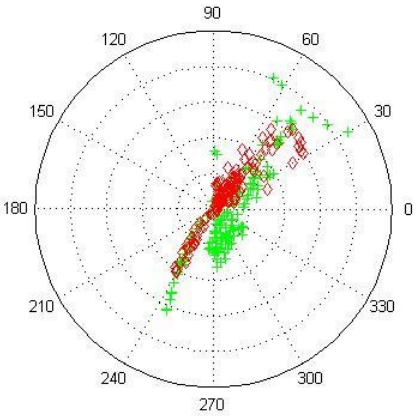

Figures 3.14: Comparison of overall dawn/dusk data. The key is clear sky (O), above average NO_2 (+) and with enhanced SPM (◇). Saturation increases by 0.1 unit intervals, truncated at 0.5 for clarity.

3.3.3 CIEDE2000 Colour Difference Formulae

Figures 3.15a and 3.15b show CIEDE2000 colour differences between the 3 sky conditions based on corrections made to the CIELAB (1976) colour space in order to make it more perceptibly evenly spaced (Millward, 2009; Witt, 2007; Sharma et al. 2005). The data are average profiles from the horizon to 20° elevation, displaying trends of above average NO_2 concentrations with and without excess SPM.

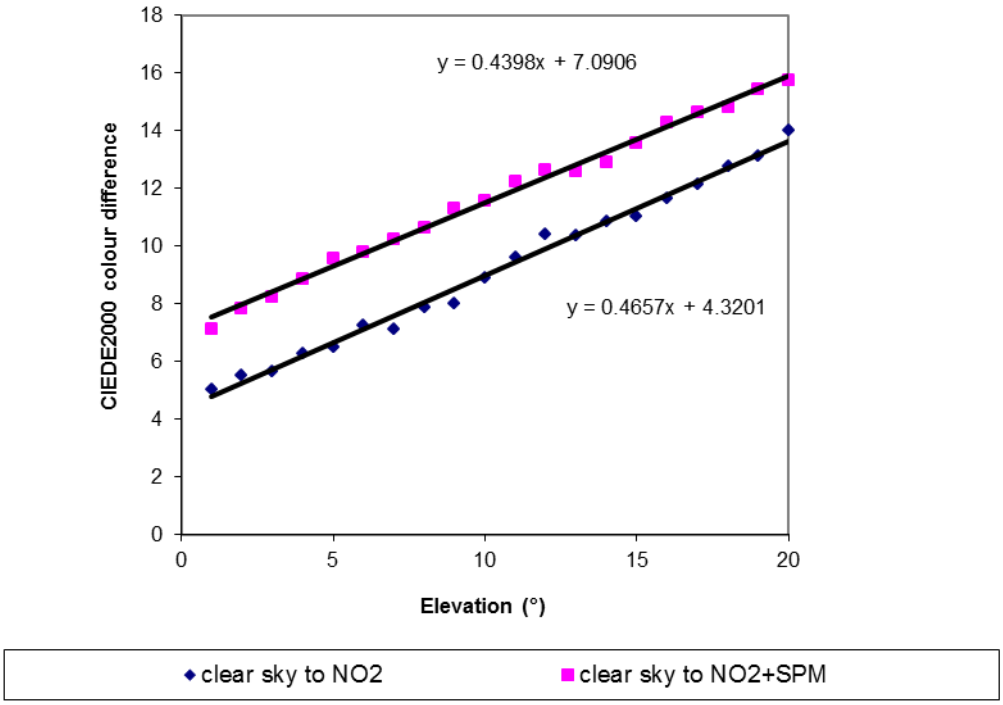

Figure 3.15a: CIEDE2000 colour differences of average midday profiles.

Despite data being collected from different azimuth with different sun elevations and azimuth, the trends for midday data for the colour differences shown in figure 3.15a are very close to being linear and parallel.

In both trendlines, colour differences increase with viewing elevation, indicating increasing relative yellow-red shifting towards the achromatic centre, as positive values for the base components of CIEDE2000 colour difference, CIELAB's a^* and b^* represent yellow and red respectively, similar to Δu^* and Δv^* values analysed in the previous section.

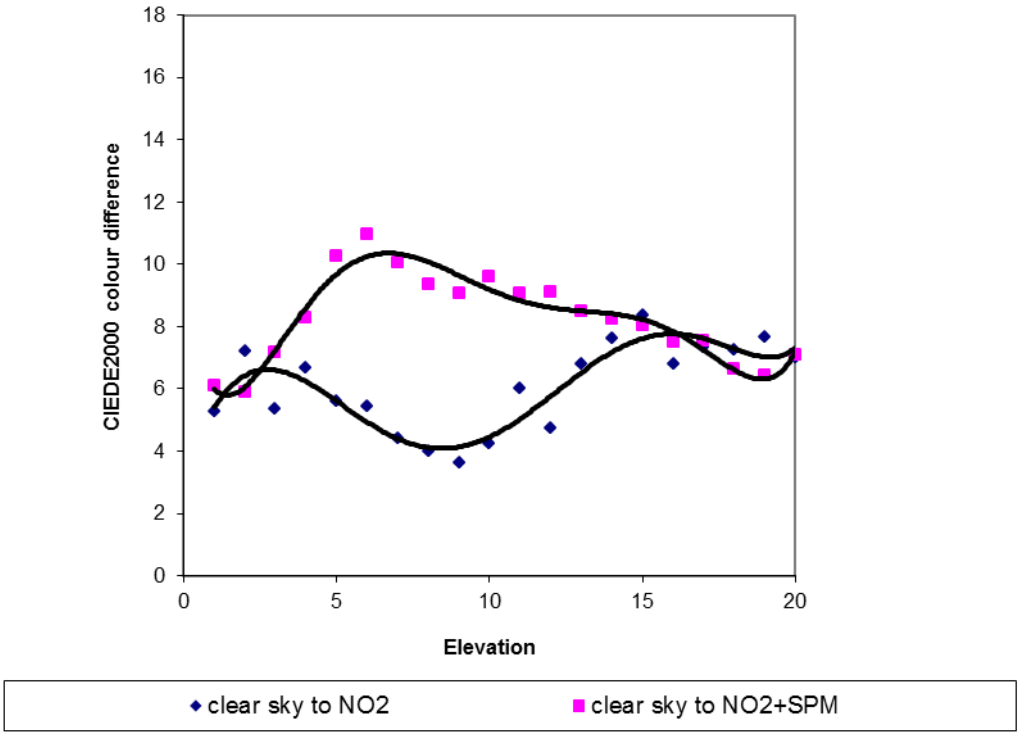

Figure 3.15b: CIEDE2000 colour differences of average dawn-dusk profiles.

Dawn-dusk colour differences are not linear, but do yield interesting distinctive results particularly with the addition of SPM, as shown in Figure 3.15b. A 6th order polynomial trendline was arbitrarily used on both sets of colour difference profiles in order to approximate the trends, however, it is unclear just how consistent this result would be upon further testing. Despite this; there are considerable fluctuations in the data that correlate with earlier results.

A very clear trend in the profiles is the divergence and reconvergence of colour differences between elevations of 3° and 14°, where the colour difference is considerably higher and more noticeable with the addition of above average SPM concentrations. Outside of these elevations, the colour difference is very similar.

Similarities include where the hooks appear on the *du'* and *dv'* charts as well as similarities to trends suggested by the data in table 3.2, that a maximum chroma/colour difference occurs above the horizon.

3.3.4 Hue Angle Comparisons.

Gamma-invariant hue angle exhibits, particularly for midday data, consistent hue angle differences with CIE LAB and CIEDE2000 derived hues, refer to Table 3.3. Evident is a semi-constant hue angle shift from blue (270°) towards green (180°) when the hue angle is invariant to brightness and gamma. Variations for gamma-invariant hue angle are far less than that of CIELAB and CIEDE2000.

Table 3.3: Comparison of CIELAB, CIEDE2000 and gamma-invariant hue angle for midday average clear sky profiles (all values are in degrees).

Clear Sky Midday hue angle comparison example			
	CIELAB hue angle	**CIEDE2000 hue angle**	**gamma-invariant hue angle**
Horizon	253	253	199
	252	249	200
	250	248	201
	253	249	201
	254	248	202
	255	250	201
	255	250	202
	256	252	201
	255	251	202
	257	254	202
	259	255	201
	259	257	201
	260	258	201
	261	259	201
	262	261	201
	263	262	201
	263	263	200
	264	264	200
	265	264	200
20°	265	265	200
Profile average	**258**	**256**	**201**
Standard deviation	**5**	**6**	**1**

3.3.4.1 Midday Gamma-Invariant Hue Angle Comparisons

Midday gamma-invariant hue angle is consistent across all 3 sky conditions with consistent very low variation, refer to table 3.4. The range observed in gamma-invariant hue angles varied by only 199° to 202°, as the standard deviation is 1°, the difference is negligible. Regardless of aerosol loading, the sky colour remains at the same green-cyan trending wavelengths, these values also include cloudy and overcast days.

Table 3.4: Comparison of gamma-invariant hue angles for the 3 sky conditions as recorded at midday (all angles are in degrees).

Midday Gamma-Invariant Hue Angles			
	Clear sky	**+NO_2**	**+NO_2 and SPM**
Horizon	199	199	202
	200	199	201
	201	200	199
	201	201	200
	202	200	201
	201	201	200
	202	200	200
	201	201	199
	202	201	200
	202	201	199
	201	202	199
	201	202	199
	201	200	200
	201	200	199
	201	201	200
	201	200	199
	200	199	199
	200	200	199
	200	200	199
20° elevation	200	201	199
Profile average	**201**	**200**	**200**
Standard deviation	**1**	**1**	**1**

3.3.4.2 Dawn-dusk Gamma-Invariant Hue Angle Differences

Similar to CIE LCH polar plots (refer to section 3.3.2), there is a clear bimodality in gamma-invariant hue angles, particularly with increasing aerosol loading. The bimodality is the cause of the greater standard deviation observed in table 3.5. However, hue angles between the 3 sky conditions are similar towards the horizon and at higher elevations.

Table 3.5: Comparison of gamma-invariant hue angles for the 3 sky conditions as recorded at dawn and dusk (all angles are in degrees).

Dawn-Dusk Gamma-Invariant Hue Angles			
	Clear sky	**+NO_2**	**+NO_2 and SPM**
Horizon	33	27	25
	30	21	26
	27	20	25
	26	19	23
	31	21	19
	54	34	18
	55	40	17
	63	57	16
	144	94	17
	187	95	14
	190	67	10
	192	142	11
	195	132	12
	196	149	23
	197	164	28
	196	176	188
	197	178	203
	197	181	195
	197	182	196
20° elevation	196	183	198
Profile average	**130**	**99**	**63**
Standard deviation	**77**	**66**	**79**

3.3.4.3 Gamma-Invariant Chroma

As gamma-invariant hue angles for all 3 air quality conditions are almost identicalor complementary (separated by 180°). Gamma-invariant chroma can be plotted against elevation for comparison for both midday and dawn-dusk, represented in figure 3.16 (The horizontal axes are shortened to 'Invariant Chroma' for clarity).

As midday gamma-invariant hue angles are equivalent, the associated gamma-invariant chroma (refer to figure 3.16, upper image) can be considered to be parallel in that respect. Gamma-invariant chroma values for all 3 sky conditions increase with greater elevation, with clear sky increasing the most. The sky profile for above average NO_2 with and without excess SPM are parallel with the former having lower chroma values, similar to what is observed for the CIEDE2000 colour differences.

Overall, the dawn and dusk chroma values are lower than those observed at midday except when SPM is added and for polluted horizons. Unlike midday data the 3 sky conditions are not parallel in hue angle. Similar to what is observed in the *du'* and *dv'* colour metrics, there are definite hooks (or turning points) in chroma that are at higher elevation to turning points in gamma-invariant hue angle. The hooks increase in elevation with increased aerosol loading.

The differing gamma-invariant hue angle and chroma observed in dawn-dusk data also reinforce the CIEDE2000 colour differences, where the greatest differences occur in between the horizon and 20° elevation.

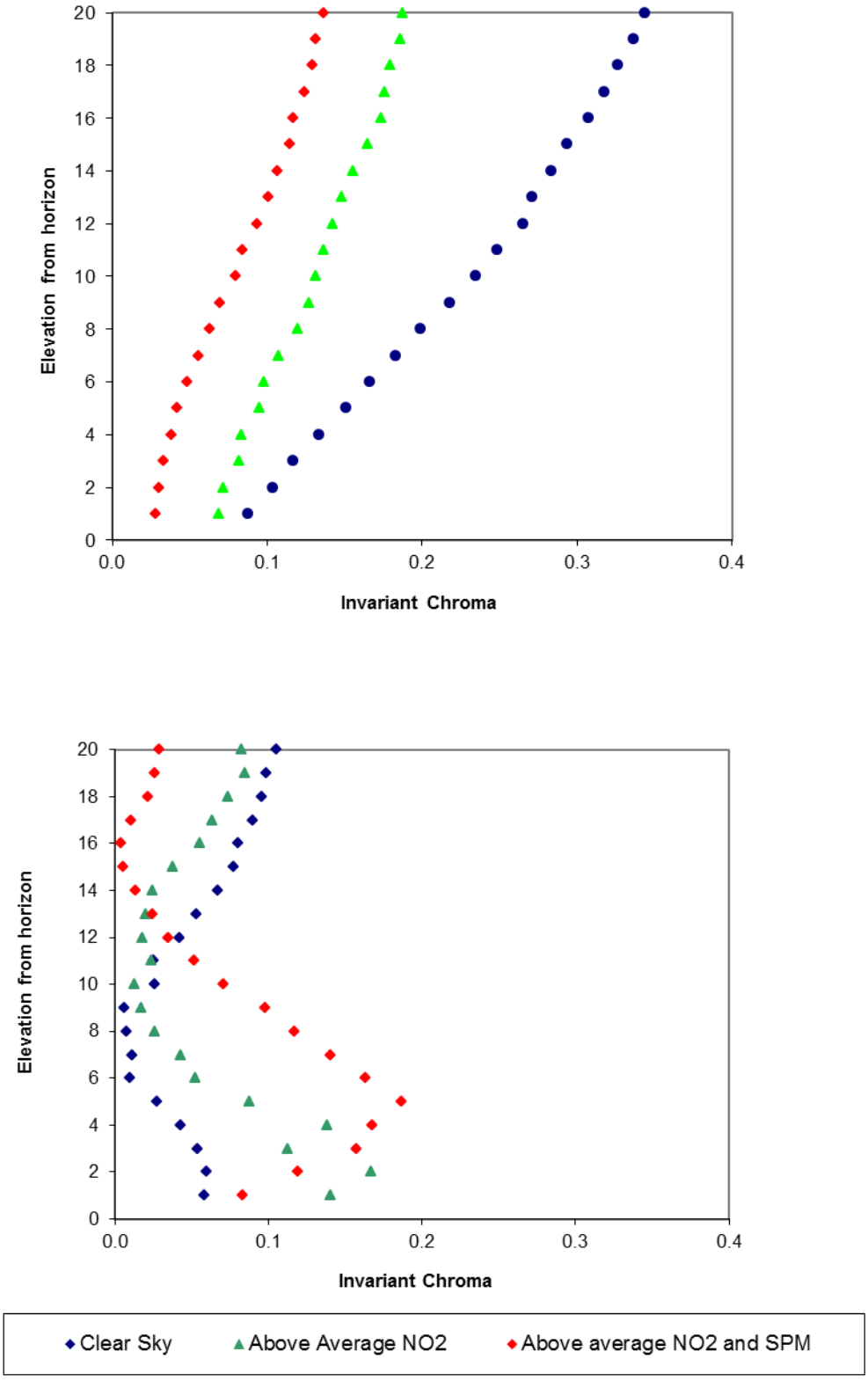

Figure 3.16: Average midday (top) and dawn-dusk (bottom) gamma-invariant chroma profiles. The elevation from the horizon is measured in degrees.

3.4 Volcanic Ash

In early February, 2009, Mt. Asama, a volcano 140 km north west of Tokyo, erupted, sending ash across the city (Kubota and Fujioka, 2009). Volcanic ash is not a major aspect of this study as ash mostly scatters rather than absorbs visible wavelengths. However, achromatic-shifting from absorbing ferrous iron could be an indicator of an ash layer, thus providing a unique opportunity to test the techniques developed in this study.

A single photo was taken (due to camera shutter mechanical error) of the southern sky when ash from the volcano was reported to be over Tokyo. When the photo was taken, the solar elevation was 11.4° above the horizon, corresponding to a relative air mass of 4.91. This is in between the definitions of dawn-dusk and midday.

At the time of the observation, the Tokyo Ministry of Environment reported that the temperature was 3.8°C with a relative humidity of 69.9% and the sky was mostly cloudy. The aerosol load officially observed was 45 ppb NO_2 (above average) and 23 $\mu g.m^{-3}$ SPM. The sky photo is included in figure 3.17.

Data collected from the photo ranges from the horizon to about 20° elevation. Data are analysed according to its CIE xy gamut, CIE u'v'Y chromatic difference from a 15000 K CCT reference blue sky, CIELUV hue angle/dominant wavelength and saturation and gamma-invariant and CIE LAB hue angle comparisons.

Figure 3.17: Photo taken of ash laden Tokyo sky from the 1st viewing platform, facing south. The photo was taken on the 3rd February, 2009.

3.4.1 Volcanic Ash CIE xy Gamut

Figure 3.18 shows the sky profile from the Tokyo sky just after the Mt. Asama volcanic eruption from data extracted from the photo in figure 3.17. The D_{65} white point is marked (grey box) for comparison.

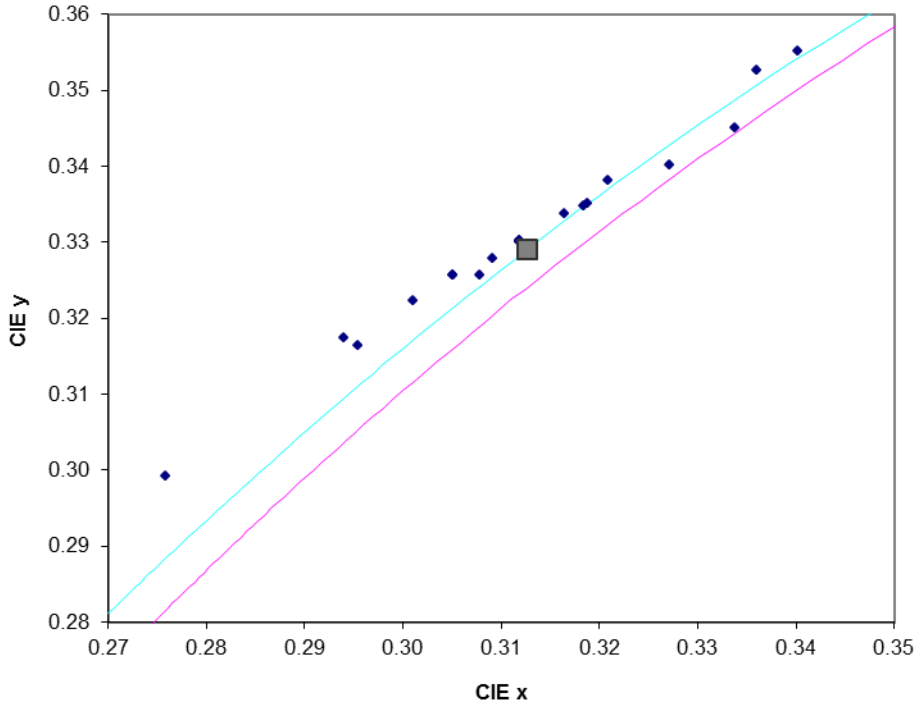

Figure 3.18: Ash laden sky profile for Tokyo from the 3rd February, 2009. The data was collected when there was also above average NO_2 concentrations recorded by the Tokyo Ministry of Environment. The D_{65} white point is indicated by the square, the CIE Daylight locus (blue) and Planckian locus (pink) are indicated.

The data are mostly linear, with horizon pixels distinctly yellow-red shifted (right of the white point). These pixels are also in between the Daylight locus and Planckian locus. A few pixels around the 10° mark are definitely achromatic, whereas those higher in elevation are blue- green shifted.

3.4.2 Volcanic Ash CIE u'v'Y Chromatic Difference

Figure 3.19 charts the CIE u'v'Y chromatic differences for the volcanic sky compared to a model 15,000 K CCT blue sky.

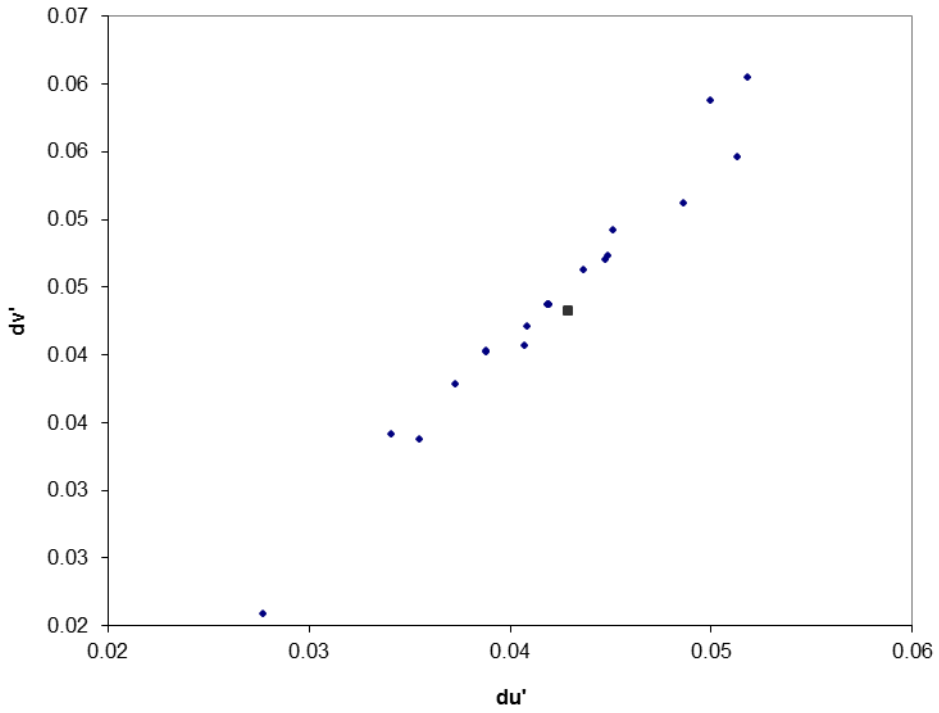

Figure 3.19: CIE u'v'Y chromatic difference comparison chart between the ash and above average NO_2 concentration laden sky and a model 15,000 K CCT blue sky. The achromatic D_{65} white point is indicated by the square.

Although not as regular as midday data, the post-eruption sample (figure 3.19) demonstrates a definite negative trend towards blue-green. All the data are noticeably red-yellow shifted (positive *du'* and *dv'*) with respect to the model sky, with the cluster around the white point clearly evident. The bimodality of colours of the sky profile is very clear, with the horizon being more yellow-red shifted.

3.4.3 Volcanic Ash Dominant Wavelength

Figure 3.20 is a polar plot of CIE LUV derived hue angle plotted against saturation (purity).

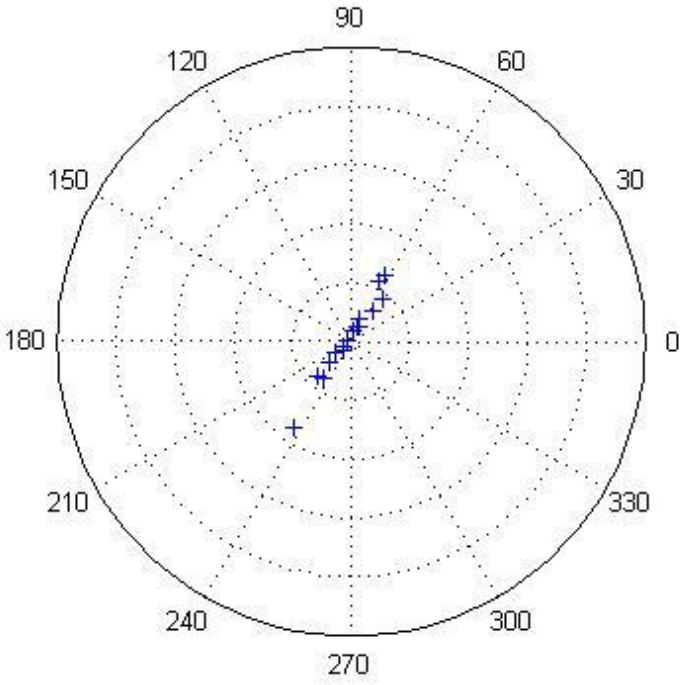

Figure 3.20: CIE LUV derived hue angle and saturation polar plot of ash and NO_2 laden Tokyo sky. Saturation is at 0.1 unit intervals, truncated at 0.5 for clarity.

The same general pattern is noted from the polar plot figure 3.20 as observed in the other metrics charted in figures 3.18 and 3.19. The bimodality of the data is not clear in the photo in figure 3.17 as most of the sky is obscured by cloud, however there is a slight yellow tinge near the horizon.

Data bimodality can be divided into 3 parts based on colour metric projections (figures 3.18, 3.19 and 3.20):

- From the horizon to approximately 8° elevation, pixel colour saturation data points towards a hue angle of approximately 60°, corresponding to a dominant wavelength of 577 nm. This is a yellow-shift in sky colour that increases in saturation closer to the horizon.

- Around 10°, the data points are almost completely achromatic (refer to table 3.6). The actual hue angle of 270° represents a discontinuity, representing achromicity (Finlayson and Schaefer, 2001). The magnitude of this achromicity does not occur readily during any other times or non-volcanic conditions.

- At higher elevations, the colour shifts almost to the exact opposite of that observed near the horizon to a hue angle of about 240°, corresponding to a dominant wavelength of 481 nm. Colour saturation increases with increasing elevation.

3.4.4 Volcanic Ash Gamma-Invariant Hue Angle Comparison

Table 3.6: Comparison of CIE LAB derived and gamma-invariant hue angles (all values are in degrees). The 3 divisions discussed in section 3.4.3 are colour coded according to the yellow shifted sky colour near the horizon, achromatic mid-elevation and blue sky at higher elevations.

	CIELAB	Gamma-Invariant
horizon	85	12
	88	11
	74	18
	93	10
	74	18
	87	13
	100	6
	87	13
	165	270
	165	270
	165	270
	165	270
	220	214
	248	202
	229	210
	229	210
	239	206
	242	205
	250	202
20° elevation	254	202

Table 3.6 is a comparison between CIE LAB derived and gamma-invariant hue angle to determine if earlier patterns are an artefact of the camera workings. It is very clear to see that the same patterns occur when the gamma-invariant RGB data is considered. The main difference is the hue angle shift, from near yellow (90°) to near red (0°/360°) and near blue (270°) to near green (180°) and vice versa.

4. Discussion

In the results section of the thesis, the data were separated by colour space and difference metrics. In this discussion, to aid in the interpretation of the results, they are reorganised by the time of the day (namely midday and dawn/dusk as defined earlier in the study).

Further analysis will be made of observations made from volcanic ash aerosol from the Mt. Asama eruption in February, 2009.

Finally, the reliability of the whole data set, inclusive of the midday and dawn/dusk data will be estimated by variance-covariance analyses of CIE colour metrics, and a brief discussion made of the viability of CIELUV derived dominant wavelengths and the CIELAB derived CIEDE2000 colour differences.

4.1 Midday

All midday chromaticities are on the green side of the Planckian and Daylight loci in the CIE xy chart in Figure 3.3, becoming less so closer to the achromatic centre white point with increasing NO_2, especially with additional SPM concentrations. Above average NO_2 with and without SPM concentrations are hard to differentiate from each other and are constrained to a one-third sector of the gamut nearest to the white point and loci, compared to clear skies. The prevalent observed green trending chromaticity gamuts are indicative of the greater influence of molecular Rayleigh scattering (Lee Jr. and Hernandez-Andres, 2003; Sastri, 1976).

An aspect that makes differentiating between a clear and polluted midday sky difficult are the respective average CIE LUV derived hue angles and associated dominant wavelengths as derived by Lillo et al. (2002). Overall, all three conditions had similar average hue angles, so dominant wavelengths are in close range (481-484 nm) which is within the blue range (refer to Table 3.1).

Chroma values decrease with increasing aerosol load, indicating desaturation towards the achromatic D_{65} white point due to the dominance of Mie scattering as observed in the CIE xy gamut. Figures 3.11a and 3.12a demonstrate the similarity between the hue angle-chroma vectors for all 3 midday conditions. What is apparent is that despite the perceived differences in a polluted and clear sky (Figures 3.9a and 3.9b respectively), the hue angle are calculated to be very similar.

NO_2 preferentially absorbs blue and some green wavelengths, resulting in a yellow-red shift described in models by Dogras et al. (2004); Sloane (1988); and observed in Los Angeles by Husar and White (1976), detected as a chromaticity shift from blue towards the achromatic white point, in the direction of the yellow-red region of the CIE xy diagram, (refer to figure 4.1).

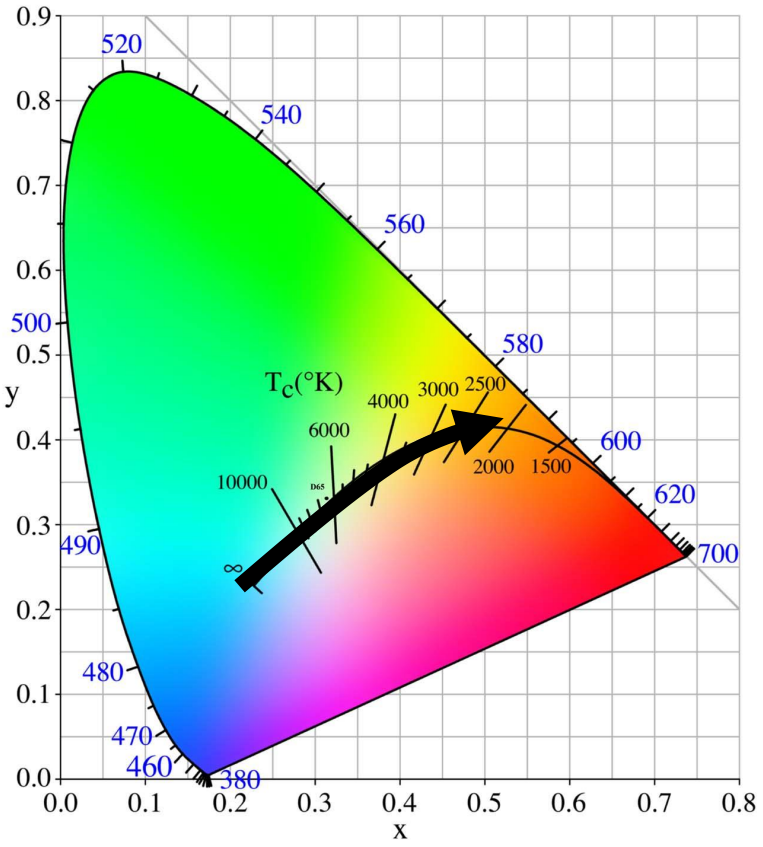

Figure 4.1: CIE xy diagram (with CCTs [T_c]) with the generalised colorimetric vector from clear to polluted sky (arrow) (Hancock Technologies).

Yellow-red shifting is also apparent on the hue angle-chroma polar diagrams but as a result of desaturation of blue by absorption and cancellation with yellow from NO_2 aerosols (Dogras et al. 2004; Sloane, 1988; Husar and White, 1976).

The addition of pollutants causes increased multiple scattering and absorption of mostly blue wavelengths, providing an achromatic 'desaturant' likely to be due to complementary colour cancellation of the blue sky with the blue-absorbing NO_2, alongside the effects of multiple scattering by SPM.

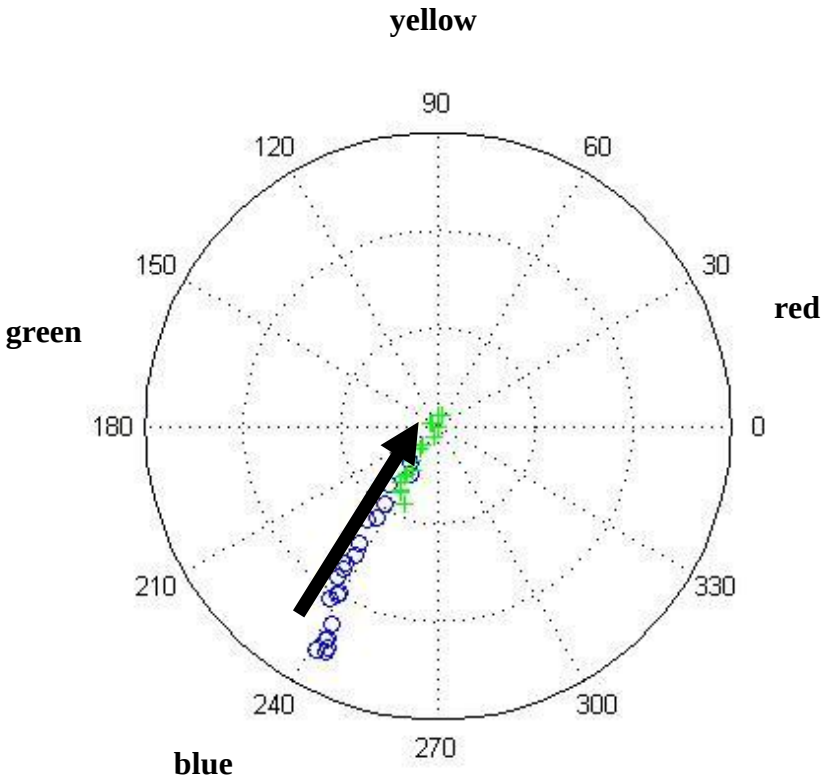

Figure 4.2: Hue angle-saturation polar plot for the polluted (+) and clear (O) sky comparison in figures 3.9a and 3.9b (adapted from figure 3.10). The colour positions are from Hunt (2004). The arrow represents the red-yellow shifting due to above average NO_2 and SPM concentrations.

Average CIE u'v'Y profiles for all 3 sky conditions share the same vector but have different magnitudes when compared to the model 15,000 K blue sky (Figure 3.5) (Kerr, 2010, 2008; Wyszecki and Stiles, 2000). Like the CIE xy colour gamut vectors, each condition's vector is positioned on the green and blue trending side of the achromatic white point. The addition of above average NO_2 results in a yellow-red shift, the addition of SPM causes an achromatic shift along the vector, as described before the CIE xy gamut.

Although there is very little literature about the application of the CIEDE2000 colour difference formula for aerosol studies, it's superseded predecessor transforms – CIE94 and CIELAB (1976) have often been used (Lee Jr. 2008; Witt, 2007; Haralabidis and Pinilis, 2005). The colour difference was taken for above average NO_2 with or without excessive SPM using average clear sky profiles as reference.

Figure 3.15a illustrates CIEDE2000 midday colour difference graphical results approximated to linear relationships. Other polynomial fitting functions were considered, but found to be unreasonable when extrapolated for the whole sky, particularly around the zenith. The equation for the observed colour difference between clear sky and above average NO_2 is approximately,

$$\Delta E_{00} = 0.4657e^0 + 4.3201, \tag{53}$$

where ΔE_{00} represents the CIEDE2000 colour difference and e^0 represents the viewing angle from the ground.

The equation for observed colour differences between clear sky and above average NO_2 with excess SPM is almost parallel, but with higher intercepts and slightly shallower gradient,

$$\Delta E_{00} = 0.4398e^0 + 7.0906, \tag{54}$$

The differing gradients also indicate that both lines intersect at some elevation angle. There is a reduction in the gradient with increasing SPM concentrations, suggesting that increasing SPM concentrations dampen NO_2 colour differences with respect to clear sky.

The colour difference for NO_2 without excess SPM becomes more important at an angle close to 100° from the ground, which is just past zenith and away from the sun. Although this is an approximation, it does fit with earlier observations made by Husar and White (1976) about the colour of Los Angeles smog, where NO_2 appears browner looking away from the sun, so causing greater colour differences than the desaturated hue angles in the sun's direction.

The CIEDE2000 colour difference between NO_2 with and without SPM is almost constant. Thus the addition of excess SPM to above average NO_2 concentrations result in the colour difference equation

$$\Delta E_{00} = 0.0259e^0 - 2.7705. \tag{55}$$

Gamma-invariant hue angle differences between above average NO_2 with and without increased SPM concentrations show a similar pattern as the CIEDE2000 corrected hue angle differences, both associated with a near constant, but substantially less estimated gamma-invariant chroma difference.

The gamma-invariant chroma estimate comparing clear sky and above average NO_2 concentrations is described in equation 56,

$$C_I = 0.0072e^0 + 0.0221, \tag{56}$$

where C_I is the gamma-invariant chroma and e^0 is elevation from the horizon.

Gamma-invariant chroma with the addition of excess SPM to NO_2 haze is described by the equation,

$$C_I = 0.0076e^0 + 0.0687 \quad (57)$$

This relationship suggests that the commonly used gamma correction exaggerates colour/chroma differences where scattering by SPM is involved, however the lines are divergent, suggesting that the addition of excess SPM results in a greater colour difference with increasing elevation.

4.2 Dawn-dusk

Dawn-dusk metrics are considerably more difficult to decipher than those recorded at midday, particularly distinguishing clear sky and above average NO_2 with excess SPM concentrations, comparisons are only marginally easier made without SPM. Clear sky colours have colorimetric similarities with polluted skies at dawn and dusk due to the longer atmospheric path length, hence greater air mass that sunlight must travel through to the camera.

In clear sky, blue is scattered out leaving behind some green, red and non-spectral purples similar to the combined effects of NO_2 and SPM observed at midday as well as at dawn and dusk (Lee Jr. and Hernandez-Andres, 2003; Lee Jr. 1994).

The trend exhibited by dawn-dusk above average NO_2 concentrations also shows a distinct yellow-red shift going from the gamut to the right of the CIE xy chart, whereas, with the presence of SPM, trending towards the achromatic centre, consistent with some of the models of Dogras et al. (2004) and Sloane (1988), (refer to figure 4.3).

While still possessing a good correlation to the CIE xy model gamut (Figure 3.4), dawn-dusk chromaticity patterns are obscured by increased effects of scattering. Most chromaticities were in between the CIE Daylight and Planckian locus or below the latter, on the 'purple' side of CIE xy diagram, generalised in figure 4.3.

Although, it is difficult to differentiate clear from hazy and dusty sky, above average NO_2 concentrations cause a distinct 'purple' shift from the modelled gamut. This observation is similar to those made in studies performed in India in the late 1960's and early 1970's by Sastri (1976) also suggesting that some instances of 'purple' trending chromaticities were due to Mie scattering by dust and soot.

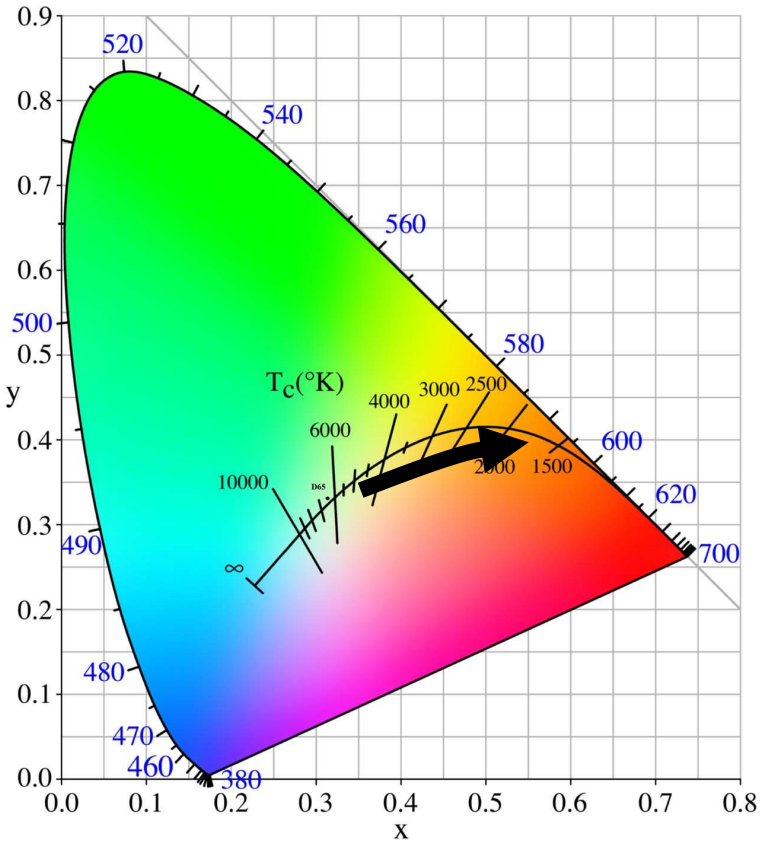

Figure 4.3: CIE xy diagram (with CCTs [T_c]) with the generalised colorimetric vector from clear to polluted sky (arrow) (Hancock Technologies).

Purple trending chromaticities are potentially due to two major factors:

- Twilight clear sky purple was determined by Lee Jr. and Hernandez-Andres (2003) to be due to the combination of molecular scattering in the high atmosphere with the reddened troposphere and stratosphere.

- Huynh and Robles-Kelly (2007) analysed the colour response of digital cameras, similar to the Canon G10 used in this study. The study determined that all cameras' white balance causes a 'purple' shift from CCTs of approximately 5000K or less, consistent with most dawn-dusk chromaticities near to the horizon.

Overall average hue angles (CIELUV, CIELAB and gamma-invariant) and associated dominant wavelengths were bimodal for all 3 sky conditions. Saturations generally shifted from desaturated yellow on the horizon to blue dominant wavelengths at 20° elevation. The blue wavelengths were similar to the dominant wavelengths recorded for midday for clear sky and above average NO_2 concentrations. However, luminance at dawn-dusk is less uniform than midday, peaking at higher elevations (refer to figures 3.8 and 3.6 respectively).

The addition of SPM resulted in an overall shift toward heavily desaturated green dominant wavelengths, (table 3.1). Dominant wavelength and gamma-invariant hue angle changes from the horizon occur more prominently with above average NO_2 concentrations. Luminance increases markedly to approximately 10° above the horizon.

The 3 sky conditions do not share the same CIE u'v'Y vectors, although they do have similarities and are approximate translations. The bimodality in the hue angles is also apparent in that each profile crosses near to the achromatic white point from red-yellow trending back to blue-green trending typical of clear sky. These vectors can be readily distinguished from each other by their position and by the elevation and magnitude chromatic 'hooks' in Figure 3.7 and described by Lee Jr. (1994).

Chromatic hooks become more prominent, occurring at a higher angle above the horizon when the aerosol load is increased. These hooks do not exactly correspond to the hooks observed in each luminance profile (figure 3.8). However, as mentioned, luminance profiles are averages, and are subject to greater variations due to scattering by greater relative air mass and aerosol dust.

CIEDE2000 colour differences were considerably different to the model for midday data (Figure 3.15b). However, there is an approximate inversion of average colour differences evident due to the presence of SPM from about 4° and 14° elevation corresponding with peaks in luminance and where gamma-invariant and colorimetric hue angles crossed over from blue to yellow. This phenomenon is due to brightness above the horizon from the presence of above average SPM concentrations with respect to the relative position of the sun at that time.

There is considerable variation in colorimetric data for dawn-dusk, so this part of the analysis is subject to caution.

4.3 Volcanic Ash Analysis

Ash from the Mt. Asama eruption in February, 2009 was reported to have gone across the Tokyo metropolitan area when the sky photo was taken. The morning that the photo was taken was mostly overcast (figure 3.17), with above average NO_2 and average SPM concentrations. The photographic sample was examined for any irregularities with respect to the other parameters (sky conditions and times). There were 3 distinct 'zones' evident in any of the metrics used with respect to the achromatic D_{65} white point:

- From the horizon to about 8° elevation, colour differences are distinctly on the yellow-red side of the white point in both of the CIE xy and CIE u'v'Y chromatic difference diagrams, further evident on the CIE LUV derived polar hue angle saturation plot, with a dominant wavelength of approximately 577 nm. These results further validate the models developed by Sloane (1988) and Dogras et al. (2004).

- The NO_2 dominant aerosol layer is 'capped' by an achromatic layer, with significantly lower saturation/purity than most other observations. This layer has significant absorption and scattering, possibly representing the ash layer, containing absorbing materials including soot and iron.

- Above this layer, the sky colour increasingly becomes bluer with a dominant wavelength of about 481 nm. Despite the clouds, the sky colour is blue of varying levels of saturation, similar to clear sky (sunny and overcast) values.

An alternative explanation can be reached this as an example of complementary colour cancellation. The achromatic middle layers described before are likely to be the result of the lower NO_2 enhanced 'yellow' layer cancelling the higher clear sky 'blue' layer, if the pixel data points' positions in figures 3.18 and 3.19 is taken into consideration. The hue angle difference between the 2 sky layers is approximately 180° as seen in figure 3.20.

The saturation approximates to a straight vector from part way from blue to yellow, illustrated in figure 4.4 over the page.

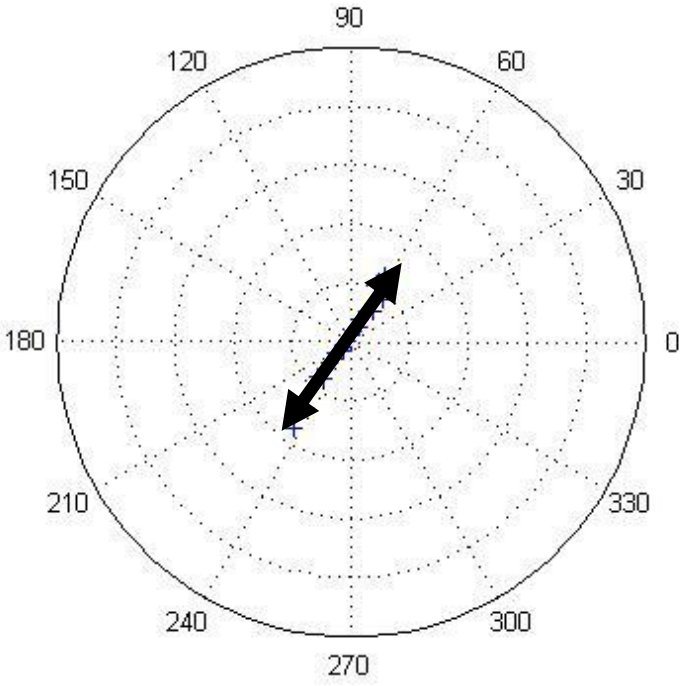

Figure 4.4: Hue angle-saturation plot (from figure 3.20) demonstrating the hue angle vector (indicated by the arrow) as observed from the sky after the Mt. Asama eruption, February 2009.

Taking a vertical profile along the hue angle vector illustrated in figure 4.4, the yellow-blue relationship can be easily seen in figure 4.5. Figure 4.5 clearly demonstrates that the magnitude of saturation is approximately equal on both the opposing blue and yellow sides.

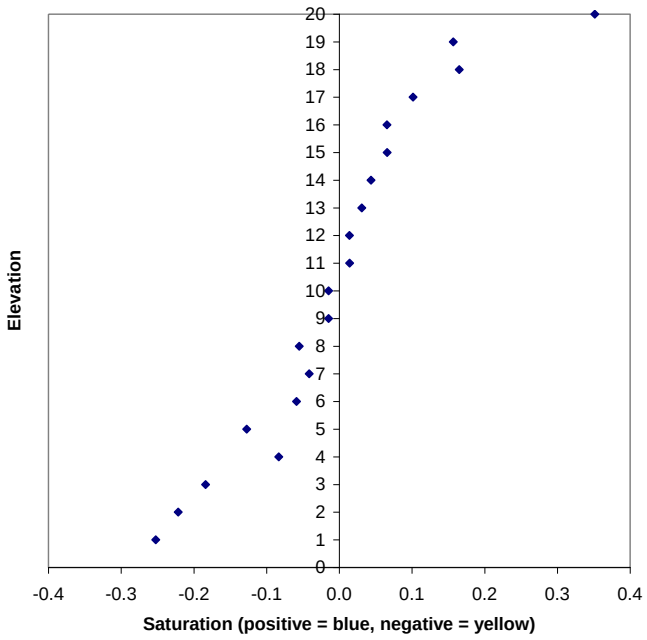

Figure 4.5: Vertical saturation profile for the hue angle vector illustrated in figure 4.4. The vertical axis (elevation) also acts as the dividing line separating blue (positive saturation) and yellow (negative saturation).

The most likely explanation for the colour shifts exhibited in figures 4.4 and 4.5 are that a combination of interrelated effects occurred. Considering multiple events allows for an approximate aerosol loading timeline to be developed and analysed as a possible model. Data of aerosol loading for the days and hours immediately prior to when the photo was taken are also considered in this explanation. The estimated timeline is outlined on the next page:

- Introduction of volcanic ash from the eruption of Mt. Asama, 140 km north west of Tokyo two days earlier. The volcanic ash's scattering of light (Tsunematsu et al. 2008) and the constituent iron absorption (Kokhanovsky, 2008) result in a desaturation of sky colour.

- However, according to the Tokyo Ministry of Environment, SPM levels were about average for that time suggesting that the scattering due to the volcanic ash is at a higher level, out of the range from the governmental measurements. Volcanic ash is sometimes hard to distinguish from high-level cirrus (Tsunematsu et al. 2008).

- As the photo was taken on a weekday, traffic borne NO pollution is expected to be higher than background or weekend levels. On the morning of the photo, NO concentrations were significantly higher than even typical weekdays. NO photochemically reacts with molecular O_2 to form NO_2 haze as the sun rises (Wayne and Wayne, 2005).

4.4 Reliability

Throughout this study, analyses of midday data are found to be more reliable than those observed from dawn-dusk, due to smaller variations in atmospheric scattering. Nevertheless, within some constraints, it is still possible to observe general trends from the dawn-dusk data.

The most reliable metrics for differentiating between clear sky, above average NO_2 concentrations with and without excess SPM are determination of dominant wavelength, approximated from the CIE LUV derived hue angle (after Lillo et al. 2002); saturation/purity, also derived from CIE LUV chroma and relative luminance (Hunt, 2006; Malacara, 2002; Wyszecki and Stiles, 2000).

The CIEDE2000 colour difference formula, derived from the CIE LAB colour space proved to be a reliable metric for comparison, (Millward, 2009; Witt, 2007; Sharma et al, 2005) alongside gamma-invariant hue angle and an estimate for gamma-invariant chroma.

None of the aforementioned metrics have been specifically used for aerosol or even general atmospheric studies. Nevertheless, the metrics are modern day derivations of, and thus supersede colour metrics that have been used for previous aerosol studies mentioned in the literature review. Gamma-invariant metrics were based on research investigating the effects of the prevalent gamma correction that is required for colorimetric transforms.

Calculations of uncertainties in each transform are a complex process due to the reliance of matrix transformations through each step. A variance-covariance matrix analysis is used to estimate the uncertainty for each metric, the process being defined by Gardner (2007). Midday data are compared to dawn-dusk uncertainties for each of the sky conditions and are presented in table 4.1 for averages of each of the main parameters used in the study.

Table 4.1: Variance-covariance uncertainties for averages of the major metrics used in this study, separated according to the time of day.

	Midday sky condition			*Dawn-dusk condition*		
Parameter	**clear sky**	**NO_2**	**NO_2 +SPM**	**clear sky**	**NO_2**	**NO_2 +SPM**
x	0.0204	0.0092	0.0115	0.0215	0.0272	0.0230
y	0.0211	0.0090	0.0105	0.0191	0.0243	0.0176
Y	14.2109	6.6994	8.5891	19.9734	20.6746	23.2717
du'	0.0082	0.0044	0.0050	0.0128	0.0152	0.0293
dv'	0.0160	0.0064	0.0075	0.0185	0.0192	0.0275
du'v'	0.0180	0.0078	0.0090	0.0225	0.0245	0.0402
L*	10.0753	3.7688	4.6540	11.4265	11.8653	12.3840
a*	3.2473	2.7324	2.4016	4.4379	7.2611	7.4441
b*	7.6691	4.0409	5.2114	9.0901	11.3819	8.9224
u*	6.1229	4.5572	5.3644	12.9783	15.2597	30.9109
v*	11.4445	6.4207	8.0825	18.4730	19.3009	29.2634
s	0.2150	0.0907	0.1106	0.0977	0.0715	0.2797
h (°)	3.2798	2.5275	2.0716	2.7721	5.0674	9.1779

All uncertainties calculated were above values considered to be just noticeable differences, described in the literature by MacAdam, (1981). There are a number of reasons that cause these uncertainties, particularly during dawn and dusk. Uncertainties are likely to be the result of the dynamic nature of scattering by particulate matter ever present in the Tokyo sky; the effects of varying humidity and the minor variable noise occurring within the camera.

The uncertainties further suggest that digital camera observations of urban aerosols are best taken at midday (solar maximum). Uncertainties for gamma-invariant hue angle and chroma estimates can be considered similar to those due to camera noise as in section 3.1.

Despite the magnitudes of the perceivable uncertainties; robust patterns can be made and clear general trends obtained from the data, particularly hue angle, hence dominant wavelength, is by far the attribute with the least relative uncertainty. The CIELAB parameter *a** with a relatively minor uncertainty, is modified as part of the CIEDE2000 colour difference metric to make it more even, but the correction has minor effects on the parameters' uncertainties.

4.4.1 Sources of Error

The colorimetric transforms performed throughout the study are means to overcome systematic errors from the camera, which can be considered to be primarily intrinsic camera and scattered light noise and green-shifting of the gamma-invariant hue angle of the sky.

The main sources of random errors come from aerosol conditions, some camera settings and assumptions related to gamma correction. These interrelated issues affect the repeatability and reproducibility of results (Malacara, 2002).

Scattering is visibly a source of increasing variance, best observed in data taken at dawn and dusk and when there were greater SPM concentrations in the midday data. However, as Kokhanovsky (2008) describes, there are many aerosols that are potential sources of temperature and humidity-dependent scattering, even in the cleanest environment.

The main sources of random errors and natural variabilities affecting the study and reproducibility of the results are listed below:

- Variable aerosols present in a coastal city, sea salt and biological aerosols would be present in a city like Tokyo. These vary randomly in size, shape and movement, (Kokhanovsky, 2008).

- The random nature of mixing different scattering and absorbent aerosols.

- Inhomogeneties in aerosol load, shape and internal structure. Many aerosol studies use the assumption that aerosols of different shapes can be approximated to a generalised diameter (Malacara, 2002). Mixed different shapes continually change the nature of scattering in an aerosol cloud (Kokhanovsky, 2008).

- The gamma correction constant of 2.4, is (as mentioned earlier) an estimate. This value depends on the response of the CCD chip to incoming light and thus can change with altering conditions, such as mentioned above. It would be prohibitively time-consuming to calculate the gamma for each pixel as would be required for increased accuracy in this regard.

5. Conclusions

5.1 Effectiveness of Digital Cameras

The hypothesis (section 1.4) is supported, with comparable observations made by an off-the-shelf digital camera to those made using more complex equipment, such as colorimeters LIDARs and sunphotometers. This is because many of the aerosol colorimetric patterns and trends observed using the above specialised equipment are replicated in the data collected in this study.

The digital camera was able to detect the main overall effects of discolouring aerosols, namely carbonaceous soot, iron and gaseous nitrogen dioxide:

- Above average NO_2 concentrations preferentially absorb blue wavelengths, resulting in a yellow-red shift.

- The presence of elevated SPM, including carbonaceous soot, influences concentrations and desaturates any colour causing a 'whitening' or 'greying' of the sky. The resultant colour could be termed as an achromatic shift.

- The detection of possible iron in the volcanic ash high above Tokyo, 2 days after the eruption of Mt. Asama.

The robustness of patterns observed in the data indicates that although some natural variability, primarily concerning scattering, resulted in perceivable uncertainties, most metrics still demonstrate optical behaviour consistent with published observations and models from different environments to Tokyo.

Overall, the colorimetric gamuts observed from the digital camera CCD imaging sensor were not affected by meteorological conditions particularly humidity, cloud cover and precipitation which varied considerably during the study. Variations in sea salt aerosol dynamics and polarising morphology, due to wind direction and humidity respectively, did not cause any significant differences in the patterns observed. This is despite coastal cities such as Tokyo having extremely large concentrations of sea salt (Kokhanovsky, 2008).

The colorimetric consistency observed for midday skies in Tokyo is similar to what was observed for Granada, Spain for different phases of daylight (Lee Jr. 2008; Lee Jr. and Hernandez-Andres, 2005; Hernandez-Andres, 2001; Lee Jr. 1994). The comparisons between Tokyo and Granada data, as well as with the Daylight locus from Judd et al. (1964) are in section 3.2.1.

Noise from the imaging process as well as the lossy JPEG compression on all photos had no effect on observed patterns. The only exception is the auto white balance may depress and lessen gradients of colorimetric gamuts (Huynh and Robles-Kelly, 2007). However, as this setting is automatic, the effect of white balance can be considered as reasonably constant.

There are 3 sets of colorimetric and colour difference metrics that particularly stand out in support of the hypothesis and in terms of low relative uncertainties, consistency with documented data and observed pattern consistency.

5.1.1 Comparisons with Published Results

Despite there being many colorimetric analyses of the polluted and unpolluted skies from around the world since the 1960's, there has been scant research correlating colorimetric values with aerosol concentrations. However, there are several relevant models available, such as the colorimetric variations due to relative air mass (Wyszecki and Stiles, 2000).

Sloane (1988) modelled the colorimetry of a sky with soot and NO_2 with concentrations of 20 $\mu g.m^{-3}$ and 100 ppb respectively. The model assumes an aerosol layer of 250 m thick and a solar angle of 75°, hence summer.

1. CIE xy gamut:

A strong agreement exists between the study's overall and specific gamuts (figures 3.2 to 3.4), the CIE daylight standard and the documented gamut recorded for Granada, Spain (Hernandez-Andres et al. 2001).

The CIE xy gamuts calculated in this study clearly exhibit the green trending clear sky chromaticities, which are due to Rayleigh scattering. The presence of SPM results in the red-yellow-purple trending chromaticities due to Mie scattering. These observations are consistent with what has been documented for places such as Granada and New Delhi by Lee Jr. and Hernandez-Andres (2003) and Sastri (1976) respectively.

Midday data has much clearer definitions of the 3 sky conditions than that observed at dawn and dusk. At midday, each of the sky differences have defined boundaries on the CIE xy diagram (refer to figure 3.3). However, there are overlaps, particularly for NO_2 with or without SPM most evident in the scattered environment at the horizon.

Average CIE xy chromaticities for above average SPM and NO_2 midday concentrations averaged (0.2907, 0.3109) and (0.2483, 0.2653) for the horizon and at 20° elevation respectively. This was slightly more blue-green than the model developed by Sloane (1988) predicted with CIE xy ranges of (0.319-0.322, 0.335-0.338) and (0.273-0.280, 0.292-0.297) for the horizon and at 20° elevation respectively. However, the model predicted NO_2 concentrations far greater than those recorded in Tokyo, hence less red-yellow shifting is to be expected.

The effect of adding SPM to NO_2 air pollution is consistent as all data were within a small distance from the white point, similar to the trend observed in models developed by Sloane (1988) and Dogras et al. (2004). The achromatic trend can be seen in the photo in figure 3.9a, particularly when compared to the relative clear sky of figure 3.9b.

The CIE xy metric reveals that the Tokyo sky is a lot cleaner at midday than was expected. The fact that all midday data were on the green side of the Daylight and Planckian locus demonstrates the predominance of molecular Rayleigh scattering (Sastri, 1976).

Despite the robustness of the CIE xy gamuts and patterns, the digital camera was able to detect the slight but consistent red-yellow shift in the chromatic differences in figure 3.5. The average midday clear unpolluted sky in Tokyo was measured as having CIE xy coordinates of (0.2907, 0.3109), considerably more red and yellow than the model clear sky described by Wyszecki and Stiles (2000), with coordinates of (0.262, 0.270).

This red-yellow shift is consistent with observations made by the author, that even on a clear blue sky day, one just needs to slide a finger down an exterior (and some interior) surfaces to find that absorbing dust and soot is ever present.

Midday data had some good agreement with the model developed by Sloane (1988). The model predicted that for a midday sky with a 250 metre thick smog layer containing 10 $\mu g/m^{-3}$ soot and no NO_2 will have CIE xy chromaticity coordinates of (0.308, 0.332) and (0.275, 0.291) for the horizon and at 20° elevation respectively. A data set for comparison observed in Tokyo had aerosol concentrations of 10 $\mu g/m^{-3}$ SPM and 11 ppb NO_2, closest to the model. The CIE xy chromaticity coordinates were in close agreement, at (0.304, 0.322) and (0.272, 0.292) for the horizon and at 20° elevation. Natural aerosol and atmospheric variations account for the differences.

By comparison, an observation in Tokyo with 59 $\mu g/m^{-3}$ SPM and 62 ppb NO_2 concentrations was observed to have a CIE xy chromaticity coordinates of (0.315, 0.332) and (0.296, 0.314) for the horizon and at 20° elevation. These observations are a good approximation to Sloane's model for a 500 metre thick haze layer with 10 $\mu g/m^{-3}$ soot and 100 ppb NO_2 has CIE xy chromaticity coordinates of (0.328, 0.344) and (0.298, 0.319) for the horizon and at 20° elevation respectively. The variation between the observations and the model is due to less NO_2 concentrations at the horizon causing a less intense yellow-redshift, and a greater amount of SPM at 20° elevation resulting in a greater shift to the achromatic centre.

2. Gamma-invariant and variant hue angle and dominant wavelength:

Hue angles possess the least relative uncertainties and most correlation consistency when compared to other metrics, particularly for midday data. From hue angle, dominant wavelength can be determined using a look-up table developed and tested by Lillo et al. (2004).

When hue angle (dominant wavelength) and saturation (purity) metrics are used together, such as for figures 3.9a and 3.9b, charted in figure 3.10, sky conditions are clearly resolved, particularly when making observations with increasing elevation from the horizon.

Gamma-invariant hue angle (where the gamma correction used for colorimetric transforms is not used), had the most consistent data, exhibiting negligible variation for all 3 sky conditions for any elevation from the horizon. However, gamma-invariant hue angles were consistently shifted towards green relative to where the correction was applied in clear sky and correspondingly towards red in the presence of NO_2, while still achromatic trending to in the presence of SPM.

Gamma-invariant hue angle green-shifting is similar to the green trend observed in the CIE xy gamut for clear sky. The red shift for above average NO_2 concentrations is similar to the constant red-shifting noted in the CIE u'v'Y chromatic difference.

Whereas our eyes perceive a hue angle shift to grey, brown or yellow when NO_2 and SPM haze occurs; the camera, not prone to subjective observations, 'sees' the apparent hue angle shift as a desaturation of the same colour. The same applies to cloudy, overcast and even rainy days. At midday, there was no significant hue angle shifts detected, particularly when the gamma-invariant data straight from the camera is considered. The effects of scattering by SPM and preferential blue absorption from NO_2 caused a desaturation and vectoring towards yellow-red (refer to figure 3.19).

Complementary colour cancellation was observed with apparent higher level desaturation via above average SPM, composed of mainly upper atmosphere volcanic ash and anthropogenic dust, resulting in sky desaturation and a stratified NO_2 haze layer causing a defined yellow-shift in lower elevations (figure 4.5).

3. CIEDE2000 colour differences

As mentioned earlier in this study, this colour difference metric has not been used directly for many aerosol studies; however its predecessors CIE LAB and CIE94 have been used. Thus, it is a natural progression to use the corrections made in calculating this metric to further try and differentiate the 3 sky conditions, as per the study's hypothesis. Colour differences between above average NO_2 concentrations with and without SPM with respect to clear sky are very distinct, particularly for midday (refer to figure 3.15a). It is clear that colour differences increase at higher elevations. The amount of above average SPM concentrations causes a parallel increase in colour difference from just above average NO_2.

Overall

Overall, using the digital camera is an effective means for differentiating NO_2 and NO_2 with SPM pollution and by further analysis, SPM haze alone. To avoid many of the greater uncertainties, the choice of metric is limited but no less powerful. Using the CIE xy gamut as a basis provides a line of constant hue angle that can be defined by using the CIE LUV derived hue angles, and defined by using a look up table from authors such as Lillo et al. (2002; 2004) to determine the dominant wavelength. Using the CIE LAB derived CIEDE2000 colour differences further differentiate aerosol types.

5.2 Further Research

5.2.1 Smartphones

Digital cameras, including the Canon G10 used in this study and DSLRs have for a long while been a dominant part of a digital photography 'ecosystem'. The ecosystem analogy for digital photography is used to describe a set of technologies and applications that 'interact with and impact on the success of one another' (Adomovicius et al. 2008).

Like the biological ecosystem, elements therein adapt and evolve with new stimuli and needs, (Tretter et al. 2010). The technological needs of consumers, businesses and increasingly for scientific field research provide the necessary stimuli for development (Tretter et al. 2010; Avvenuti and Vecchio, 2008).

In this study, the Canon G10 digital camera, image analysis and data processing programs (MATLAB and Microsoft Excel) formed what Tretter et al, (2010) described as the digital imaging 'ecology'. A similar process could be used for webcams, except that in these cases, the camera as a direct continuous link to the computer, but is also encumbered by it, thus making its use not feasible for most cases due to lack of portability.

The data collection and analysis process can be made far more efficient with the use of prolific readily available smartphone and iPhone technology where image capture, RGB data collection and colorimetric transforms and analyses could potentially be performed in this portable medium.

During the past few years, there has been a growing proliferation of Smartphones, including the much-advertised Apple iPhone, where digital imaging and communications technologies have been integrated with greater portability than ever before (Perna, 2010; Tretter et al. 2010; Cellular News, 2009; Avvenuti and Vecchio, 2008).

Smartphones are a representative example of products that are grouped as Consumer Electronics 2.0. The proliferation of Smartphones is set to continue as according to Cellular News (2009), the amount of Smartphone users will likely exceed 1.1 billion by 2013 and is likely to experience accelerated growth into the future.

Technologies following the concept of Consumer Electronics 2.0 are compatible with and ideal for this kind of project as it refers to accessible technological developments that use off-the-shelf hardware components with new and varying software functionalities (Tretter et al. 2008).

Avvenuti and Vecchio (2008) observed that "the growing ubiquity and usability of smart mobile phones can be exploited to develop popular and realistic pervasive computing applications", particularly with the integration of imaging and communication functions (Tretter et al. 2008).

Software development, not hardware is the focus of the Consumer Electronics 2.0, researching and developing means of reusing existing technology for more complex tasks (Tretter et al. 2008). Recently, a programming platform has been developed for the sole use in Smartphones, known as Android (Perna, 2010; Tretter et al. 2010).

Like computer based platforms, including Google's Chrome, Microsoft's Internet Explorer, Mozilla Firefox and Apple's Safari, Android has the ability to be customised. With any appropriate programming platform, it is possible for a camera phone to not only capture image, but extract digital image information in the same way that algorithms used in MATLAB for this study (Avvenuti and Vecchio, 2008). Auto analysis algorithms are also increasingly widespread (Tretter et al. 2010).

This study used Microsoft Excel to transform and analyse RGB image data. This process is mathematical, thus can be written as a series of algorithms or 'apps' for each colorimetric metric and difference formula (Avvenuti and Vecchio, 2008). These 'apps' can be made available for download by anyone for private or academic use.

5.2.2 UV Capabilities

Nitrogen dioxide is unique in that it is the only gaseous aerosol that significantly absorbs in the visible wavelengths (Kokhanovsky, 2008; Dogras et al. 2004; Jacobson, 2002; Horvath, 1993; Sloane, 1988). However, all gaseous aerosols absorb in the shortwave ultraviolet range, including commonplace urban aerosols as sulphur dioxide (SO_2), nitrogen oxide (NO) and ozone (O_3), (Jacobson, 2002; Horvath, 1993).

UV digital photography is not new, Elen (2010) and Naturfotograf.com (2004) have used it to view the 'hidden' side of flowers in particular. A study by Kantzas and McGonigle (2008) used ultraviolet photography to measure the extent of aerosols from volcanic plumes in a similar manner to what could be used in urban studies.

5.3 Closing Remarks

The main difficulties were quite normal for many Postgraduate students and independent field scientists alike – resources, finances and most of all, limitations of time. The study was completed alongside full time Physics teaching duties in an International Baccalaureate World School in Tokyo, Japan. The potential for loss of motivation was never a problem as the study held great interest as it was engaging and relevant.

It was not possible to access and use any of the Ministry of Environment's or Japan Meteorology Agency's monitoring equipment. However this was not necessary, as the Ministry published online data on aerosol concentrations from measurement locations around Tokyo, including one location very close to where the sky pictures were taken. The potential limitation of lack of access provided the opportunity to explore and utilise online resources that are freely available.

An encouraging benefit from this study was the great interest it generated among my students at the school, when discussed with them or when they assisted with the setting up of the camera. The students found relevance in the topic of air pollution and are familiar with digital cameras, and this helped them become very supportive of my work. It is hoped that air pollution studies using digital cameras would form engaging exercises for metropolitan school students elsewhere if supported by simple colorimetric analyses.

Community participation engenders greater awareness of issues such as air pollution, ever present in the Tokyo megacity and all other urban centres. Conducting complex scientific research that normally requires the use of often inaccessible equipment, using instead everyday accessible equipment promotes and encourages the active participation and curiosity needed to inform the public about scientific discovery and related technologies.

References

1. Ackermann, J. 1998, 'The Extinction-to-Backscatter Ratio of Tropospheric Aerosol: A Numerical Study', *Journal of Atmospheric and Oceanic Technology*, vol. 15, pp. 1043-1050

2. Adobe, 2000, *The Munsell Color System*, viewed 2nd March, 2010, http://dba.med.sc.edu/price/irf/Adobe_tg/models/munsell.html

3. Adomivicius, G. Bockstedt, J. Gupta, A. and Kauffman, R. 2008, 'Making Sense of Technology Trends in the Information Technology Landscape: A Design Science Approach', *Management Information Systems Quarterly*, vol. 32, pp. 779-809

4. Alexander, D. Crozier, P. and Anderson, J. 2008, 'Brown Carbon Spheres in East Asian Outflow and Their Optical Properties', *Science*, vol. 321, pp. 833-836

5. Arizona Digital Imaging Institute, *A Tale of 3 Kitties*, ADII Volume 7, viewed 31st January, 2010 http://www.azdii.com/n107.html

6. Avvenuti, M. and Vecchio, A. 2008, 'Mobile phone and visual tags: linking the physical world to the digital domain', *Advances in Ubiquitous Computing, Future Paradigms and Directions*, IGI Publishing

7. Bedford, R. and Wyszecki, G. 1958, 'Wavelength Discrimination for Point Sources', *Journal of Optical Society of America*, vol. 48, pp. 129-135

8. Ben Chouikha, M. Placais, B. Pouleau, G. Sautot, S. and Vienot, F. 2006, 'Benefits and Drawbacks of two Methods for Characterizing Digital Cameras', *CGIV 2006 Proceedings*, Society for Imaging Science and Technology, pp. 185-188

9. Brady, M. and Legge, G. 2009, Camera calibration for natural image studies and vision research, *Journal of the Optical Society of America A*, vol. 26, pp. 30-42

10. Brainard, D. and Stockman, A. 2009, *Colorimetry*, in Bass, M. DeCusates, D. Enoch, J. Lakshminarayanan, V. Li , G. MacDonald, C. Mahayan, V. and van Stryland, E. (eds), *OSA Handbook of Optics*, 3rd ed. New York, McGraw Hill

11. Brown, J. 2007, 'How Monet's cataracts coloured his view of the lilies', *The Independent*, 16 May, 2007

12. Brown, W. and MacAdam, D. 1949, 'Visual Sensitivities to Combined Chromaticities and Luminance Differences', *Journal of the Optical Society of America*, vol. 39, pp. 808-835

13. Buluswar, S. and Draper, B. 2001, 'Color Models for Outdoor Machine Vision', *Computer Vision and Vision Understanding*, vol. 84, pp. 1-29

14. Burns, P. and Berns, R. 1997, 'Error Propogation Analysis in Colour Measurement and Imaging', *Color Research and Application*, vol. 22, pp. 280-289

15. Butkus, N. and Johnson, B. 2010, 'The Effects of Krakatau's Eruption of 1883 on Art Around the World', *Proceedings of the 44th Annual Meeting of the North Central and South Central Chapter of the Geological Society of America*, 11-13 April, 2010

16. Cairns, B. Lacis, A. and Carlson, B. 1998, 'Estimating Aerosol Absorption, Optical Depth, and Vertical Extent Using Satellite Measurements in the UV/Blue Spectral Domain', *Proceedings of the 8th Atmospheric Radiation Measurement (ARM) Science Team Meeting*, Tuscon, Arizona

17. Canon, Canon PowerShot G10 specifications. viewed 4th June, 2009 http://www.canon.com.au/products/cameras/digital_compact_cameras/powershotg10_specs.aspx
18. Canon Professional Network, Capturing the image: DIGIC processing, viewed 9th June, 2009 http://cpn.canon-europe.com/content/infobank/capturing_the_image/digic_processing.do

19. Carlson, J. 2010, *Canon Powershot G10/G11: From Snapshots to Great Shots*, Peachpit Press, Berkely

20. Cellular News, 2009, 'Global Sales of Smartphones to Reach 310 Million Units in 2013', viewed 21st August, 2010 http://www.cellular-news.com/story/38286.php

21. Charity, M. 2001, *Blackbody color datafile*, viewed 21st March, 2010 http://www.vendian.org/mncharity/dir3/blackbody/UnstableURLs/bbr_color.html

22. Chou, C. Chen, W. Chang, S. Chen, T. and Huang, S. 2005, 'Specific Absorption Cross-section and Elemental Carbon Content of Urban Aerosols', *Geophysical Research Letters*, vol. 32, L21808

23. CIE DS 011.1/E-2001, 2001, *Spatial distribution of daylight –CIE standard general sky*, Draft standard, CIE Central Bureau, Vienna

24. Darula, S. and Kittler, R. 2002, 'CIE General Sky Standard Defining Luminance Distributions', viewed 15th Jan, 2010 http://www.metla.fi/lignum-weppijakelu/CIE/CIEsky.pdf,

25. Darula, S. and Kittler, R. 1999, 'A Catalogue of fifteen sky luminance patterns between the CIE standard skies', *Proceedings of the 24th CIE Session, Warsaw, Poland*, CIE Publication 133, vol. 1, part 2, pp. 7-9

26. Davidson, J. Cantrell, C. McDaniel, A. Shetter, R. Madronich, S. and Calvert, J. 1988, 'Visible-Ultraviolet Absorption Cros Section for NO_2 as a Function of Temperature', *Journal of Geophysical Research*, vol. 93, pp. 7105-7112

27. Derefeldt, G. and Hedin, CE. 1989, 'Visualization of VDU colours by means of the CIELUV colour space', *Displays*, vol. 10, pp. 134-146

28. Derefeldt, G. Hedin, CE. and Sahlin, C. 1987, 'Transformation of NCS data into CIELUV colour space', *Displays*, vol. 8, p. 183-192

29. De Tomasi, F. Tafuro, A. Kinne, S. and Perrone, M. 2007, 'Application of LIDAR and sun photometer measurements to aerosol radiative forcing calculations', *3rd Symposium on LIDAR Atmospheric Applications*, San Antonio, Texas

30. Digital Photography Review, Canon G10 Powershot, viewed 7th June, 2009 http://www.dpreview.com/news/0809/08091702canon_g10.asp#tech

31. Dogras, C. Ioannidou, M. and Chrissoulidis, D. 2004, 'Analytical study of the changes in the color of daylight due to sulphate droplets and soot grains in the atmosphere', *Journal of Quantitative Spectroscopy and Radiative Transfer*, vol. 84, pp. 223-238

32. Duffy, P. and Bonfils, C. 2007, 'Interpreting Recent Temperature Trends in California', *EOS*, vol. 88, pp. 409-410

33. Elen, S. 2010, *Beyond Visible: Ultraviolet, Infrared and Luminescence Photography*, viewed 12 May, 2010, http://www.beyondvisible.com

34. Fairchild, M. 2005, *Colour Appearance Models*, John Wiley and Sons

35. Fink, W. 2008, *The Digital Sensor: A Guide to Understanding Digital Cameras*, viewed 1 September, 2010, http://www.anandtech.com/show/2507/2

36. Finlayson, G. and Schaefer, G. 2001, *Hue that is gamma-invariant to brightness and gamma*, Proceedings of the British Machine Vision Conference, Manchester, pp. 303-312

37. Ford, A. and Roberts, A. 1998, *Color Space Conversions*, viewed 1st August 2009 http://www.poynton.com/PDFs/coloreq.pdf

38. Fukushima, H. 2006, 'Air Pollution in East Asia – Japan's Role as an Environmentally Advanced Asian Country', *Quarterly Review*, no. 18, pp. 54-64

39. Gangl, M. Kocifaj, M. Videen, G. and Horvath, H. 2007, 'Light absorption by coated nano-sized carbonaceous particles', *Atmospheric Environment*, vol. 42, pp. 2571-2581

40. Gardner, J. 2007, *Uncertainties in Spectral Colour Measurement*, in Schanda, J. (ed) *Colorimetry: Understanding the CIE System*, New Jersey, John Wiley and Sons

41. Global Volcanism Program, *Asama*, viewed 22 August, 2010, http://www.volcano.si.edu/world/volcano.cfm?vnum=0803-11=

42. Green, P. 2002, *Colorimetry and colour difference*, in Green, P. and MacDonald, L. (eds) Chichester, John Wiley and Sons Ltd

43. Haber, J. Magnor, M. and Seidel, H. 2005, 'Physically-Based Simulation of Twilight Phenomena', *ACM Transactions on Graphics*, vol. 24, pp. 1353-1373

44. Hancock Technologies, n.d., *Color Basics*, viewed March 21, 2010 http://hancocktechnologies.com/Color%20Basics.html

45. Haralabidis, P. and Pilinis, C. 2008, 'Skylight Color Shifts due to Variations of Urban-Industrial Aerosol Properties: Observer Color Difference Sensitivity Compared to a Digital Camera', *Aerosol Science and Technology*, vol. 42, pp. 658-673

46. Haralabidis, P. and Pilinis, C. 2005, 'Linear color camera model for a skylight colorimeter with emphasis on the imaging pipeline noise performance', *Journal of Electronic Imaging*, vol. 14, 043005

47. He, X. Li, C. Lau, A. Deng, Z. Mao, J. Wang, M. and Liu, X. 2009, 'An intensive study of aerosol optical properties in Beijing urban area', *Atmospheric Chemistry and Physics Discussions*, vol. 9, pp. 11413-11440

48. Heckaman, R. and Fairchild, M. 2006, 'Expanding Display Color Gamut Beyond the Spectrum Locus', *Color Research and Application*, vol. 31, pp. 475-482

49. Heredia, F. and Chozas, M. 1992, 'Proposal of a novel formula to calculate the dominant wavelength for colour of red wines', *Food Chemistry*, vol. 43, pp. 125-128

50. Hernandez-Andres, J. Lee Jr. R. and Romero, J. 2003, 'Color and Luminance Asymmetries in the Clear Sky', *Applied Optics*, vol. 42, pp. 458-464

51. Hernandez-Andres, J. Romero, J. and Lee Jr. R., 2001, 'Colorimetric and spectroradiometric characteristics of narrow-field-of-view clear skylight in Granada, Spain', *Journal of the Optical Society of America*, vol. 18, pp. 412-420

52. Hernandez-Andres, J. Romero, J. and Nieves, J. 2001, 'Color and spectral analysis of daylight in southern Europe', *Journal of the Optical Society of America*, vol. 18, pp. 1325-1335

53. Hernandez-Andres, J. Lee, R. and Romero, J. 1999, 'Calculating correlated color temperatures across the entire gamut of daylight and skylight chromaticities', *Applied Optics*, vol. 38, pp. 5703-5709

54. Highwood, E. and Stevenson, D. 2003, 'Atmospheric Impact of the 1783-1784 Laki Eruption: Part II: Climatic Effect of Sulphate Aerosol', *Atmospheric Chemistry and Physics*, vol. 3, pp. 1177-1189

55. Hinds, W. 1999, *Aerosol Technology: Properties, Behaviour and Measurement of Airborne Particles*, 2nd ed. New York, John Wiley and Sons

56. Holm, J. Tastl, I. Hanlon, L. and Hubel, P. 2003, 'Color processing for digital photography', *in* Green, P. and MacDonald, L. (eds) *Colour Engineering: Achieving Device Independent Colour*, John Wiley and Sons, East Sussex

57. Horvath, H. 1993, 'Atmospheric Light Absorption – A Review', *Atmospheric Environment*, vol. 27A, pp. 293-317

58. Hunt, R. 2006, *The Reproduction of Color*, 6th Edition, John Wiley and Sons

59. Husar, R. and White, W. 1976, 'On the Color of the Los Angeles Smog', *Atmospheric Environment*, vol. 10, pp. 199-204

60. Hutchings, J. 2006, 'Talking about Colour… Design and Colour Research - Where Next?', *Color Research and Application*, vol. 31, pp. 250-252

61. Huynh, C. and Robles-Kelly, A. 2007, 'Comparative Colorimetric Simulation and Evaluation off Digital Cameras using Spectroscopy Data', *Digital Imaging Computing Techniques and Applications*, 9th Biennial Conference of the Australian Pattern Recognition Society, 3-5 Dec, 2007, pp. 309-316

62. Hyslop, N. 2009, 'Impaired visibility: the air pollution people see', *Atmospheric Environment*, vol. 43, pp. 182-195

63. IEC 61966-2-1: 1999, Color management – Default RGB color space – sRGB

64. IEC 61966-9: 2003, Multimedia systems and equipment – Color measurement and management – Digital cameras

65. Imatest, 2009, *Noise in Photographic Images*, viewed 26th July, 2009 http://www.imatest.com/docs/noise.html

66. Immler, F. Treffeisen, R. Engelbart, D. Kruger, K. and Schrems, O. 2008, 'Cirrus, contrails, and ice supersaturated regions in high pressure systems at northern mid latitudes', *Atmospheric Chemistry and Physics*, vol. 8, pp. 1689-1699

67. Isono, K. 1955, 'On Ice Crystal Nuclei and Other Substances Found in Snow Crystals', *Journal of Meteorology*, vol. 12, pp. 456-462

68. Jacobson, M. 2002, *Atmospheric Pollution: History, Science and Regulation*, Cambridge, University Press

69. Jacobson, M. 2001, 'Strong radiative heating due to the mixing state of black carbon in atmospheric aerosols', *Nature*, vol. 409, pp. 695-697

70. Jacobson, R. Ray, S. Attridge, G. and Axford, N. 2000, *The Manual of Photography*, 9th edition, Focal Press, Oxford

71. Janeiro, F. Wagner, F. Ramos, P. and Silva, A. 2007,'Automated Atmospheric Visibility Measurements using a Digital Camera and Image Registration', *15th IMEKO TC-19 International Symposium*, Romania, vol. 1, pp. 13-17

72. Johnson, K. Zuberi, B. Molina, L. Molina, M. Iedema, M. Cowin, J. Gaspar, D. Wang, C. and Laskin, A. 2005, 'Processing of soot in an urban environment: case study from the Mexico City Metropolitan Area', *Atmospheric Chemistry and Physics Discussions*, vol. 5, pp. 5585-5614

73. Judd, D. MacAdam, D. and Wyszecki, G. 1964, 'Spectral Distribution of Typical Daylight as a Function of Correlated Colour Temperature', *Journal of the Optical Society of America*, vol. 54, pp. 1031-1040

74. Kandi, S. and Tehran, M. 2010, 'Investigation of the Effects of Texture on the Performance of Colour Difference Formulae', *Color Research and Application*, vol. 35, pp. 94-100

75. Kantzas, E. and McGonigle, A. 2008, 'Ground Based Ultraviolet Remote Sensing of Volcanic Gas Plumes', *Sensors*, vol. 8, pp. 1559-1574

76. Kasten, F. and Young, A. 1989, 'Revised optical air mass tables and approximation formula', *Applied Optics*, vol. 28, pp. 4735-4738

77. Kerr, D. 2010, *Readings in Digital Photography, the Science Demystified*, www.lulu.com

78. Kerr, D. 2008, *A Metric for Chromaticity Difference*, viewed 11th November, 2009, http://dougkerr.net/pumpkin/articles/Chromaticity_Metric.pdf

79. Kim, Y. 2006, 'Color and Symbolic Meaning of Elements in Nature', *Color Research and Application*, vol. 31, pp. 341-349

80. Kodak, 2005, *CCD Image Sensor Noise Sources*, Application note, revision 2.1

81. Koenderink, J. 2010, 'The prior statistics of object colours', *Journal of the Optical Society of America A*, vol. 27, pp. 206-217

82. Kokhanovsky, A. 2008, *Aerosol Optics: Light Absorption and Scattering by Particles in the Atmsophere*, Chichester, Praxis

83. Kondo, Y. Komazaki, Y. Miyazaki, Y. Moteki, N. Takegawa, N. Kodama, D. Deguchi, S. Nogami, M. Fukuda, M. Miyakawa, T. Morino, Y. Koike, M. Sakurai, H. and Ehara, K. 2006, 'Temporal variations of elemental carbon in Tokyo', *Journal of Geophysical Research*, vol. 111, D12205

84. Kubota, Y. and Fujioka, C. 2009, 'Japan volcano Mt. Asama erupts, ash dusts Tokyo', *Reuters*, Feb. 2, 2009

85. Kuehni, R. 2008, 'Forgotten Pioneers of Color Order. Part II: Matthias Klotz (1748-1821)', *Color Research and Application*, vol. 33, pp. 341-345

86. Kuehni, R. 2007a, 'Development of the Idea of Simple Colours in the 16th and 17th Centuries', *Color Research and Application*, vol. 32, pp. 92-99

87. Kuehni, R. 2007b, 'Ludwig Pilgrim, a Pioneer of Colorimetry', *Color Research and Application*, vol. 32, pp. 5-10

88. Lee Jr. R. 2008, 'Measuring overcast colors with all-sky imaging', *Applied Optics*, vol. 47, pp. H106-H115

89. Lee Jr, R. and Hernandez-Andres, J. 2005, 'Colors of the daytime overcast sky', *Applied Optics*, vol. 44, pp. 5712-5722

90. Lee Jr, R and Hernandez-Andres, J. 2003, 'Measuring and modelling twilight's purple light', *Applied Optics*, vol. 42, pp. 445-457

91. Lee Jr. R. 1994, 'Twilight and daytime colors of the clear sky', *Applied Optics*, vol. 33, pp. 4629-4638

92. Lillo, J. Moreira, H. and Gomez, N. 2002, 'Reflectance and Energetic Imbalance: Colourimetric Evaluation of the NCS Colour Atlas', *Psicologia*, vol. 23, pp. 209-231

93. Lim, H. MatJafri, M. Abdullah, K. AlSultan, S. and Saleh, N. 2004, 'Application of Digital Camera Data for Air Quality Detection', *ACRS 2004*

94. Lindbloom, B. *BruceLindbloom.com* Accessed April 2nd, 2010 http://www.brucelindbloom.com/

95. Liu, W. Wang, Y. Russell, A. and Edgerton, E. 2005, 'Atmospheric aerosol over two urban-rural pairs in the southeastern United States: Chemical composition and possible sources', *Atmospheric Environment*, vol. 39, pp. 4453-4470

96. Long, C. Sabburg, J. Calbo, J. and Pages, D. 2006, 'Retrieving Cloud Characterisitics from Ground-Based Daytime Color All-Sky Images', *Journal of Atmospheric and Oceanic Technology*, vol. 23, pp. 633-652

97. MacAdam, D. 1981, 'Perceptual Significance of Colorimetric Data for Colors of Plumes and Haze', *Atmospheric Environment*, vol. 15, pp. 1797-1803

98. MacAdam, D. 1942, 'Visual Sensitivities to Color Differences in Daylight', *Journal of the Optical Society of America*, vol. 32, pp. 247-273

99. MacEvoy, B. 2009, *The Geometry of Color Vision*, Accessed 3rd April, 2010, http://www.handprint.com/HP/WCL/color2.html

100. Mahadev, S. and Henry, R. 1999, 'Application of a Color-Appearance Model to Vision through Atmospheric Haze', *Color Research and Application*, vol. 24, pp. 112-120

101. Mahmood, R. 2007, 'Effect of Human Activities on the Atmosphere', *EOS*, vol. 88, p.580

102. Malacara, D. 2002, *Color Vision and Colorimetry: Theory and Applications*, SPIE Press, Washington

103. Malinowski, S. Zawadzki, I. and Banat, P. 1998, 'Laboratory Observation of Cloud-Clear Air Mixing at Small Scales', *Journal of Atmospheric and Oceanic Technology*, vol. 15, pp. 1060-1065

104. Martinez-Verdu, F. Pujol, J. Vilaseca, M. and Capilla, P. 2003, 'Characterization of a digital camera as an absolute tristimulus colorimeter', *JIST*, vol. 47

105. McCreary, J. *Filter options for digital cameras*, viewed 19th July, 2009 http://www.dpfwiw.com/filters.html#factors

106. McLean, 1997, *Electronic Imagery in Astronomy*, Praxis Publishing, Chichester

107. Melgosa, M. Huertas, R. and Berns, R. 2004, 'Relative significance of the terms in the CIEDE2000 and CIE94 color difference formulas' *Journal of the Optical Society of America A*, Vol 21, pp. 2269-2275

108. Melgosa, M. 2000, 'Testing CIELAB-Based Color-Difference Formulas', *Color Research and Application*, vol. 25, pp. 49-55

109. Milward, S. 2009, *Color Difference Equations and Their Assessment*, in RIT, *Test Targets*, Rochester Institute of Technology

110. Ministry of Environment, Government of Japan, viewed 27th February, 2010 http://www.env.go.jp/en/

111. Minoura, H. Takahashi, K. Chow, J. and Watson, J. 2006, 'Multi-year trend in fine and coarse particle mass, carbon and ions in downtown Tokyo, Japan', *Atmospheric Environment*, vol. 40, pp. 2478-2487

112. Molders and Olson, 2004, 'Impact of Urban Effects on Precipitation in High Latitudes', *Journal of Hydrometeorology*, vol. 5, pp. 409-429

113. Monkkonen, P. Koponen, I. Lehtinen, K. Hameri, K. Uma, R. and Kulmala, M. 2005, 'Measurements in a highly polluted Asian mega city: observations of aerosol number size distribution, modal parameters and nucleation events', *Atmospheric Chemistry and Physics*, vol. 5, pp. 57-66

114. Naturfotograf.com 2004, *Which lenses?*, viewed 18 May, 2010, http://www.naturfotograf.com/UV_IR_rev05.html

115. Nave, R. n.d. *Hyperphysics – Light and Vision*, viewed 28th February, 2010, http://hyperphysics.phy-astr.gsu.edu/hbase/vision/ciecon.html#c1

116. Nayatani, Y. and Nakajima, M. 1996, 'Prediction of the Helmholtz-Kohlrausch Effect Using the CIELUV Formula', *Color Research and Application*, vol. 21, pp. 252-268

117. Nieves, J. Valero, E. Nascrimento, S. Hernandez-Andres, J. and Romero, J. 2005, 'Multispectral synthesis of daylight using a commercial digital camera', *Applied Optics*, vol. 44, pp. 5696-5709

118. Ohno, Y. 2000, 'CIE Fundamentals for Colour Measurement', *IS & T NIP16 Conference*, Vancouver, Canada, Oct 16-20, 2000

119. Okubo, S. and Takahashi, H. 2009, 'Long-term and seasonal trend of SPM concentration and its spatial distribution in the Kanto region, Japan', *7th International Conference on the Urban Climate*, July, 2009, Yokohama, Japan

120. Orava, J. Jaaskilainen, T. and Parkkinen, J. 2004, 'Color Errors of Digital Cameras', *Color Research and Application*, vol. 29, pp. 217-221

121. Osada, K. Kido, M. Nishita, C. Matsunaga, K. Iwasaka, Y. Nagatani, M. and Nakada, H. 2007, 'Temporal variation of water-soluble ions of free trophospheric aerosol particles over central Japan', *Tellus*, vol. 59, pp. 742-754

122. Pandis, S. Wexler, A. and Seinfeld, J. 1995, 'Dynamics of Tropospheric Aerosols', *Journal of Physical Chemistry*, vol. 99, pp. 9646-9659

123. Parisi, A. Sabburg, J. and Kimlin, M. 2004, *Scattered and Filtered Solar UV Measurements*, Kluwer Academic Publishers, Dordrecht

124. Perna, G. 2010, 'No Longer Niche, Smartphones Sales Skyrocket', *International Business Times*, Aug 13, 2010

125. Petty, G. 2006, *First Course In Atmospheric Radiation*, 2nd ed. Madison, Sundog Publishing

126. Postylyakov, O. Ugolnikov, O. Maslov, I. and Masleev, A. 2003, 'Polarization of the Twilight Sky: Measurements, Empirical Model, Radiative Transfer Simulation and Application to Aerosol Profile Retrieval', *Geophysical Research Abstracts*, vol. 5, pp. 13842-13855

127. Preetham, A. Shirley, P. and Smits, B. 1999, 'A Practical Analytic Model for Daylight', *Siggraph 99, Los Angeles*, pp. 91-100

128. Pujol, J. De Lasarte, M. Arjona, M. Vilaseca, M. Martinez-Verdu, F. De Fez, D. and Viqueira, V. 2004, 'Performance analysis of different optoelectronic imaging sensors for applications in color measurements', *Proceedings of the AIC 2004, Color and Paints, Interim Meeting of the International Color Association*, pp. 143-146

129. Renard, J. Daugeron, D. Personne, P. Legros, G. Baillargeat, J. Hadamcik, E. and Worms, J. 2005, 'Optical properties of randomly distributed soot: improved polarimetric and intensity scattering functions', *Applied Optics*, vol. 44, pp. 591-596

130. Romero, J. Hernandez-Andres, J. Nieves, J. and Garcia, J. 2003, 'Color Coordinates of Objects with Daylight Changes', *Color Research and Application*, vol. 28, pp. 25-35

131. Rossi, L. Rose, P. and Marino, A. 2010, 'Teaching Optics in North Uganda', *Optics and Photonics News*, vol. 21, pp. 14-17

132. Roy, G. Hayman, S. and Julian, W. 1998, 'Sky Modeling from Digital Imagery', *ARC Project A89530177 Final Report*, The University of Sydney and Murdoch University, Australia

133. Sabburg, J. and Wong, J. 1999, 'Evaluation of a Ground-Based Sky Camera for Use in Surface Irradiance Measurement', *Journal of Atmosphere and Oceanic Technology*, vol. 16, pp. 752-759

134. Sastri, V. 1976, 'Locus of daylight chromaticities in relation to atmospheric conditions', *Journal of Physics D: Applied Physics*, vol. 9, pp. L1-L3

135. Scandinavian Colour Institute: Natural Colour System, 2004, viewed 1st April, 2010, http://www.ncscolour.com/webbizz/mainPage/main.asp

136. Schaefer, D. and Domroes, M. 2009, 'Recent climate change in Japan – spatial and temporal characteristic of trends in temperature', *Climate of the Past*, vol. 5, pp. 13-19

137. Schanda, J.. 2007, *CIE Colorimety*, in Schanda, J. ed. *Colorimetry: Understanding the CIE System*, New Jersey, John Wiley and Sons

138. Schnaiter, M. Horvath, H. Mohler, O. Naumann, K. Saathoff, H. and Schlock, O. 2003, 'UV-VIS-NIR spectral optical properties of soot and soot-containing aerosols', *Journal of Aerosol Science*, vol. 34, pp. 1421-1444

139. Seinfeld, J. and Pandis, S. 2006, *Atmospheric Chemistry and Physics: From Air Pollution to Climate Change*, 2nd ed. Hoboken, John Wiley and Sons

140. Seiz, G. and Baltsavias, M. 2000, 'Cloud Mapping Using Ground-Based Imagers', *IAPRS, vol. XXXIII, Amsterdam*

141. Shaddix, C. And Williams, T. 2007, 'Soot: Giver and Taker of Light', *Scientific American*, vol. 95, pp. 232-239

142. Sharma, G. Wu, W. and Dalal, E. 2005, 'The CIEDE2000 Color-Difference Formula: Implementation Notes, Supplementary Test Data, and Mathematical Observations', *Color Research and Applications*, vol. 30, pp. 21-30

143. Shields, J. Karr, M. Tooman, T. Sowle, D. and Moore, S. 1998, 'The Whole Sky Imager – A Year of Progress', *Proceedings of the 8th Atmospheric Radiation Measurement (ARM) Science Team Meeting*

144. Simkin, T. and Siebert, L. 1994, *Volcanoes of the World*, Smithsonian Institute and Geoscience Press Inc. Tuscon

145. Simonini, S. Elston, S and Stone, C. 2001, 'Soot temperature and concentration measurements from color charge coupled device camera images using a three-color method', *Proceedings of the Institution of Mechanical Engineers*, vol. 215, pp. 1041-1052

146. Sloane, C. 1988, 'Contribution of NO_2 and Soot to the Discoloration of Urban Skies', *Atmospheric Environment*, vol. 22, pp. 2021-2031

147. Souch, C. and Grimmond, S. 2006, 'Applied climatology: urban climate', *Progress in Physical Geography*, vol. 30, pp. 270-279

148. Spasojevic, B. and Mahdavi, A. 2005, 'Sky Luminance for Computational Daylight Modeling', *Ninth International IBPSA Conference*, Montreal, Canada, August 15-18

149. Spivey, N. 2005, *How Art Made the World*, London, BBC

150. Takamura, T. 1992, 'Spectral Reflectance in an Urban Area – A Case Study for Tokyo', *Boundary-Layer Meteorology*, vol. 59, pp. 67-82

151. Takeo, M. 2008, 'Review of Volcano Science at Mt. Asama, Japan', *International Workshop on High Energy Earth Science: Moon and Neutrino Radiography*, Tokyo, Japan, June 26-27, 2008

152. TechTarget, 2009, *Canon PowerShot G10 Review*, viewed 28th December, 2009 http://www.digitalcamerareview.com/default.asp?newsID=3775&review=canon+powershot+g10

153. Torres, O. Bhartia, P. Herman, J. Sinyuk, A. Ginoux, P. and Holben, B. 2002, 'A Long-Term Record of Aerosol Optical Depth from TOMS Observations and Comparison to AERONET Measurements', *Journal of the Atmospheric Sciences*, vol. 59, pp. 398-413

154. Tretter, D. Liu, J. Zhang, K. Gao, Y. Atkins, B. Chao, H. Xiao, J. Wu, P. and Lin, Q. 2010, 'Multimedia Experience on Web Connected CE Devices', viewed 16 August, 2010, http://www.hpl.hp.com/techreports/2010/HPL-2010-48.html

155. Tsunematsu, N. Nagai, T. Murayama, T. Adachi, A. and Murayama, Y. 2008, 'Volcanic Ash Transport from Mt. Asama to the Tokyo Metropolitan Area Influenced by Large Scale Wind Circulation', *Journal of Applied Meteorology and Climatology*, vol. 47, pp. 1248-1265

156. Tsutsumi, Y. Ohno, T. and Takeuchi, . 2005, 'Annual Variations of Spring Aerosol Events Observed by Sun Photometers from 1998 to 2002 over Japan', *Journal of the Meteorological Society of Japan*, vol. 83A, pp. 307-313

157. Tsutsumi, Y. Morishita, H. Yoshida, M. Odashima, K. Saito, A. Suzuki, K. and Ijima, O. 2004, 'Analyses of Aerosol Events Observed at Four Sun Photometer Sites in Japan during March-April 2002', *Journal of the Meteorological Society of Japan*, vol. 82, pp. 1161-1172

158. Ugolnikov, O. Postylyakov, O. and Maslov, I. 2004, 'Effects of Aerosol and Multiple Scateering on the Polarization of the Twilight Sky', *Journal of Quantitative Spectroscopy and Radiative Transfer*, vol. 88, pp. 233-241

159. Uno, I. Ohara, T. and Wakamatsu, S. 1996, 'Analysis of Wintertime NO_2 Pollution in the Tokyo Metropolitan Area', *Atmospheric Environment*, vol. 30, pp. 703-713

160. van de Hulst, H. 1981, *Light Scattering By Small Particles*, revised edition, Mineola, Dover Publications

161. Wang, J. Xia, X. Wang, P. and Christopher, S. 2004, 'Diurnal variability of dust aerosol optical thickness and Angstrom exponent over dust source regions in China', *Geophysical Research Letters*, vol. 31, L08107

162. Wayne, C. and Wayne, R. 2005, *Photochemistry*, Oxford Chemistry Primers, Oxford University Press, Oxford

163. Widmann, J. Duchez, J. Yang, J. Conny, J. and Mulholland, G. 2005, 'Measurement of the optical extinction coefficient of combustion-generated aerosol', *Journal of Aerosol Science*, vol. 36, pp. 283-289

164. Williams, B. 2005, *A History of Light and Lighting*, viewed 24th April, 2010, http://www.mts.net/~william5/history/hol.htm

165. Witt, K. 2007, *CIE Color Difference Metrics*, in Schanda, J. ed. *Colorimetry: Understanding the CIE System*, New Jersey, John Wiley and Sons

166. Wright, W. 2007, *Professor's Wright's Paper from the Golden Jubilee Book: the Historical and Experimental Background to the 1931 CIE System of Colorimetry*, in Schanda, J. (ed), *Colorimetry: Understanding the CIE System*, Hoboken, John Wiley and Sons.

167. Wuller, D. and Gabele, H, 2007, 'The usage of digital cameras as luminance meters' *SPIE-IS&T*, vol. 6502, pp. 65020U-1 – 11

168. Wyszecki, G. and Stiles, W. 2000, *Color Science: Concepts and Methods, Quantitative Data and Formulae*, 2nd edition, Wiley, New York

169. Yamanoi, Y. Takeuchi, S. Okumura, S. Nakashima, S. and Yokoyama, T. 2008, 'Colour Measurements of Volcanic Ash Deposits from Three Different Styles of Summit Activity at Sakurajima Volcano, Japan, Conduit Processes Recorded in Colour of Volcanic Ash', *Journal of Volcanology and Geothermal Research*, vol. 178, pp. 81-93

170. Yan, P. Tang, J. Huang, J. Mao, J. Zhou, X. Liu, Q. Wang, Z. and Zhou, H. 2008, 'The measurement of aerosol optical properties at a rural site in Northern China', *Atmospheric Chemistry and Physics*, vol. 8, pp. 2229-2242

171. Yoshida, H. 2006, 'Evaluation of Image Quality', *in* Nakamura, J. (ed) *Image Sensors and Signal Processing for Digital Still Cameras*, CRC Press, Boca Raton

172. Yoshikado, H. and Tsuchida, M. 1996, 'High Levels of Winter Air Pollution under the Influence of the Urban Heat Island along the shore of Tokyo Bay', *Journal of Applied Meteorology*, vol. 35, pp. 1804-1813

173. Zelanski, P. and Fisher, M. 1994, *The Art of Seeing*, 3rd ed. New Jersey, Simon and Schuster.

174. Zerefos, C. Gerogiannis, V. Balis, D. Zerefos, S. and Kazantzidis, A. 2007, 'Atmospheric effects of volcanic eruptions as seen by famous artists and depicted in their paintings', *Atmospheric Chemistry and Physics*, vol. 7, pp. 4027-4042

175. Zhang, H. and Montag, E. 2006, 'How Well Can People Use Different Color Attributes', *Color Research and Application*, vol. 31, pp. 445-457

176. Zhang, R. Khalizov, A. Pagels, J. Zhang, D. Xue, H. and McMurry, P. 2008, 'Variability in morphology, hygrocopicity, and optical properties of soot aerosols during atmospheric processing', *PNAS*, vol. 105, pp. 10291-10296

177. Zielinski, G. Fiacco, R. Mayewski, P. Meeker, L. Whitlow, S. and Twickler, M. 1994, 'Climatic Impact of the AD 1783 Asama (Japan) Eruption was Minimal: Evidence form the GISP2 Ice Core', *Geophysical Research Letters*, vol. 21, pp. 2365-2368

Bibliography

Cargill, M. and O'Connor, P. 2009, *Writing Scientific Research Articles: Strategies and Steps*, Wiley-Blackwell, Chichester

A. Glossary

All definitions are paraphrased from Hunt (2006), Jacobson, (2002), Malacara, (2002) and Wyszecki and Stiles, (2000) unless otherwise stated.

ABC

Absorption – Cancellation of part or all the target light wavelengths.
Achromatic – Of 'no colour', white, grey and black.
Achromatic-shifting – Colour trending towards white, grey and black.
Aerosol – Airborne particle or droplet.
Albedo – Reflecting power of a surface.
Aperture – Variable lens opening in a camera, also referred to as 'f-number'.

Backscatter – Total reflection of light into the incident direction by a particle.
Brightness – CIE Y parameter.

CCD – Charge-Coupled Device, the light sensitive sensor in a digital camera, Smartphone, webcam and security camera used to convert the energy from incoming photons to an electric impulse.
CCN – Cloud Condensation Nuclei, usually a particle of dust or sea salt that attracts moisture.
CCT – Correlated Colour Temperature, a colour's equivalent blackbody temperature in Kelvin.
Chroma – the resolved vector between 2 colorimetric parameters. Related to purity.
Colorimetry – the study of the measurement of colour.
Complementary colour cancellation – Where opposing colours, such as blue and yellow and red and green can partly or completely 'cancel' each other out to become achromatic.

DEF

D_{65} – White point, approximating daylight, with a CCT of 6504K.
Digital count/ Digital number – relative strength of a pixel's colour, starting at 0 for not present to a maximum of 255.
Dominant wavelength – see hue.
DSLR – Digital Single-Lens Reflex cameras.

Exif – photographic information about a digital image, found from viewing the image's properties.

f-number – see aperture.
FOV – Field of View, or viewing area, usually measured in degrees or steradians.

GHIJ

Gamma correction – Standardised power based correction applied to 'straighten' the camera's response to low and high digital counts. The standard is 2.4, though many situations are less.
Gaseous aerosol – Aerosols that exist as molecules in the atmosphere, such as NO_2.

Hue – The specific colour of a sample. Related to dominant wavelength.

ISO number – The speed of a camera.
IEC – International Electrotechnical Commission.

KLMN
LIDAR – LIght Detection And Ranging – a remote sensing device that measures properties of light.
Lightness – Also referred to as relative luminance, scaled from 0 to 100 for dark and brightest respectively.

Microlensing – The focussing of incident light on an aerosol particle by the coated fluid. For example, sulphuric acid will microlens onto soot.

OPQR
Planckian Locus – Chromaticities of blackbody objects.
Purity – see saturation

STUV
Saturation – A quotient of the colour sample's chroma and relative luminance (or lightness), scaled from 0 to 100, it represents purity of the colour where 0 is the least pure and 100 is the most pure.
Scattering – The dispersion of specific or all wavelengths of light. Termed 'Single Scattering' for when the interaction with one type of aerosol is considered and 'Multiple Scattering' for multiple interactions.
SNR – Signal to noise ratio, a measure of photons being received properly by the sensor (signal) compared to those that do not (noise).
SPM – Suspended Particulate Matter, includes dust, soot, ash and other solid particles.
Steradian – Solid angle, the area measured by the field of view.

Tristimulus – Red-green and blue stimuli to the human eye or image sensor.
Turbidity – A measure of how turbulent the aerosol ladened sky is, mainly affecting visibility.

WXYZ
Whitepoint – A position on a CIE xy and UCS diagram of equal energy.

Yellow-red shifting – Colour values vectoring to towards yellow-red on a CIE xy and CIE u'v'Y diagram. Mathematically, increasing x and u parameters respectively.